

**DEVELOPMENT OF EXPERIMENTAL TECHNIQUES FOR STUDYING
GAS DIFFUSION AND WATER TRANSPORT IN THE POROUS MEDIA
OF FUEL CELLS**

by

Siddiq Husain Tahseen

B.Sc., Islamic University of Technology, 2009

A THESIS SUBMITTED IN PARTIAL FULFILLMENT OF
THE REQUIREMENTS FOR THE DEGREE OF

MASTER OF APPLIED SCIENCE

in

The College of Graduate Studies
(Mechanical Engineering)

THE UNIVERSITY OF BRITISH COLUMBIA
(Okanagan)

April 2013

© Siddiq Husain Tahseen, 2013

ABSTRACT

Polymer Electrolyte Membrane (PEM) fuel cells, which produces electricity by oxidation of hydrogen and reduction of oxygen with water as the only waste product, have shown great potential as a zero-emission and high-efficiency source of energy. Despite the numerous advantages of the fuel cell, its performance must still be improved significantly. Numerous studies have identified water management as the major problem hindering commercialization of fuel cells. One of the components playing an important role in water management is the porous gas diffusion layer (GDL) across which reactant transport and water removal occur. Due to a long operation or large output current, the water production rate exceeds the water removal rate. As a result, water accumulates in the pores of the GDL and blocks convective and diffusive transport of reactants. This is the origin of the limiting current. To enhance water management, the reactant transport and water removal mechanisms inside the GDL needs to be thoroughly studied. Despite various numerical models developed to illustrate the multiphase flow in the cell, these mechanisms are not well understood due to the structural complexity of the GDL. In this thesis, experimental techniques are developed for the measurement of gas diffusion and water content inside the GDL. For the latter, the fluorescence microscopy technique is used to measure the pressure and time required for water to penetrate and break through the surface of the GDL. The results show that the breakthrough time and pressure are larger for hydrophobic GDLs. However, the effect of the sample thickness is found to be negligible. An innovative experimental technique is developed for the determination of the effective diffusion co-

efficient as a function of the water content in the GDL. The results demonstrate that diffusivity is greater for samples with higher porosity. Also, it is shown that the presence of cracks in the micro-porous layer of the GDL increases water accumulation within the pores, reducing significantly diffusive transport within the GDL. These experimental techniques provide basic insights into the transport properties of the GDL which can lead to the design of new materials that enhance transport inside the porous media.

Keywords: PEM fuel cell, GDL, gas diffusivity, water management, water transport.

PREFACE

The research presented in this thesis consists of two segments: the measurement of water content inside porous GDL and the measurement of diffusion. Both the research was conducted under the watchful supervision of Dr. Mina Hoorfar. The total research for the measurement of water content inside the GDL was conducted at the Advanced Thermo-Fluidic Laboratory (ATFL) in the school of engineering, UBC Okanagan. The experiments for the measurement of gas diffusion were conducted at the laboratory of Ballard Power Systems Inc. This thesis has been proofread and cleared by Ballard Power Systems Inc. for any IP conflict.

The results for measurement of water content obtained using the 1st generation set-up was published in ASME Fuel Cell Conference 2012 (Tahseen et al. 2012) and presented in WHEC 2012 conference. The 1st generation set-up was designed by Mehdi Shabraeeni at ATFL. However, modifications in the experimental procedure were done by the author. The problems associated with the measurement were identified by the author and the second generation set-up was designed and modified by the author. All the experiments involved with the 1st and 2nd generation set-up, the analysis of the data and the preparation of the manuscript were also done by the author himself.

The literature review and the scope of research related to the measurement of diffusivity were done by the author. The development of the setup and measurements were conducted in collaboration with an undergrad student (Samuel Yew)

List of Publications

1. S.H.Tahseen, K. Chen, M. Shahraeni, S.C.M. Yew and M. Hoorfar.
Measurement of Liquid Water Content inside the Gas Diffusion Layer.
ESFuelCell2012-91084, San Diego, CA.
2. S.H.Tahseen, K. Chen, M. Shahraeni, S.C.M. Yew and M. Hoorfar.
Measurement of Liquid Water Content inside the Gas Diffusion Layer after the
Time of Breakthrough. WHEC-2012, Toronto, ON.
3. S.H.Tahseen A.S. Milani and M. Hoorfar. Sensitivity Analysis of Mass
Transport Properties of Gas Diffusion Layers of Polymer Electrolyte Membrane
Fuel Cells. ICNMM2012-73107.Puerto Rico, USA.
4. M. Shahraeni, S.C.M. Yew, S.H. Tahseen and M. Hoorfar. Accurate
measurement of capillary pressure-saturation correlation for gas diffusion
layers. ICNMM2012-73059, Puerto Rico, USA.

TABLE OF CONTENTS

ABSTRACT.....	ii
PREFACE.....	iv
TABLE OF CONTENT.....	vi
LIST OF TABLES.....	x
LIST OF FIGURES.....	xi
NOMENCLATURE.....	xvi
ACKNOWLEDGEMENTS.....	xx
DEDICATION.....	xxi
CHAPTER 1: INTRODUCTION.....	1
1.1 Basic Principle of PEM Fuel Cells.....	3
1.2 Water Management.....	10
1.3 Gas Diffusion Layer.....	11
1.4 Literature Review.....	15
1.4.1 Experimental Visualization of Water Transport in the GDL.....	15
1.4.2 Theoretical and Experimental Estimation of Gas Diffusivity in the GDL.....	25

1.5	Objective	34
1.6	Structure of the Thesis	35
CHAPTER 2: EXPERIMENTAL SETUP FOR STUDYING WATER		
TRANSPORT IN GAS DIFFUSION LAYER (GDL).....		37
2.1	Experimental Setup (First Generation)	38
2.1.1	Fluorescence Microscopy	39
2.1.2	Water Injection	42
2.1.3	Calibration	44
2.1.4	Experimental Procedure	48
2.1.5	Limitations of First Generation Setup	51
2.2	Experimental Setup (Second Generation).....	52
CHAPTER 3: EXPERIMENTAL SETUP FOR MEASUREMENT OF		
EFFECTIVE DIFFUSION COEFFICIENT IN GAS DIFFUSION LAYER (GDL).....		57
3.1	Principle of Measurement	58
3.2	Schematic of Experimental Setup.....	61
3.3	Diffusion Assembly	63
3.4	Peripheral Devices	69
3.4.1	Gas Supply.....	69
3.4.2	Differential Pressure Sensor	71

3.4.3	Back Pressure Assembly	72
3.4.4	Gas Chromatograph.....	73
3.5	Water Injection.....	75
3.6	Experimental Procedure.....	77
3.6.1	Selection of Samples	79
3.6.2	Testing Procedure	80
3.7	Numerical Analysis.....	84
CHAPTER 4: RESULTS AND DISCUSSION.....		92
4.1	Results for water transport.....	92
4.1.1	First generation setup.....	93
4.1.2	Second Generation Setup.....	103
4.2	Results for gas diffusivity	113
4.2.1	Effect of Porosity on Diffusivity	114
4.2.2	Effect of Thickness on Diffusivity	117
4.2.3	Effect of Pressure Difference on Diffusivity Measurements.....	118
4.2.4	Comparison with Literature.....	119
4.2.5	Wet Diffusivity	123
4.2.6	Impact of wettability.....	127

CHAPTER 5: CONCLUSIONS AND FUTURE WORK.....	128
5.1 Conclusions.....	129
5.2 Potential applications of the research	131
5.3 Future Work	132
REFERENCES	134

LIST OF TABLES

Table 3-1: Experimental operating conditions.....	78
Table 3-2: Properties of the GDL samples tested. The results shown in this table are obtained from [103].	80
Table 3-3: The Knudsen number for different GDLs	85
Table 3-4: Flow regimes based on the Knudsen number	86

LIST OF FIGURES

Figure 1-1:	Schematic of the PEM fuel cell operation principle	6
Figure 1-2:	A typical polarization curve depicting the change in voltage and power for a change in current density. Different losses occurring during different regime is also highlighted.....	10
Figure 1-3:	SEM images of a Toray TGP-H-060 GDL sample with 40% wt. PTFE loading: (left) 200x and (right) 1000x magnification.....	13
Figure 1-4:	SEM image of a SGL-34BC GDL sample with MPL: (left) lateral view, (right) transverse view.....	15
Figure 2-1:	Schematic of the first generation setup developed based on the method reported in [62].....	39
Figure 2-2:	Fluorescence microscopy and the different components of the microscope used for top view imaging	41
Figure 2-3:	A sectional view of the experimental setup (left) and the first generation setup developed to study water transport in GDL (right).....	42
Figure 2-4:	Pressure sensor calibration graph showing the change in voltage with the change in manometer height	46
Figure 2-5:	Calibration procedure adopted to measure the expansion of tubing (left); the result of the calibration experiment (right).....	48
Figure 2-6:	First generation assembly: the platform for GDL (left), the pressure cylinder (middle), the cap used to exert pressure on the pressure cylinder (right).....	49
Figure 2-7:	A typical response curve of the pressure sensor which displays its output in terms of voltage.....	54

Figure 2-8:	Schematic of the second generation assembly	55
Figure 2-9:	The second generation of the experimental setup developed for the measurement of the water content in the GDL	56
Figure 3-1:	Mass transfer by diffusion in a binary mixture	59
Figure 3-2:	Schematic of the flow stream in the diffusion assembly based on the diffusion bridge technique [100]	60
Figure 3-3:	Schematic of the diffusivity setup and its main components: I-1 and I-2 are the two flow-meters; V-1, V-2, V-3, V-4, V-9, V-10 and V-11 are quarter turn needle valves; V-5, V-6, V-7 and V-8 are metering valves; E-1, E-2, E-3, E-4 and E-5 are water knockouts; I-3 is the differential pressure sensor, I-4 and I-5 are the pressure sensors measuring the pressure difference between the inlets and outlets; GC is the gas chromatograph; and BPR is the back pressure assembly	63
Figure 3-4:	Flow plate design	65
Figure 3-5:	Velocity profiles at different cross sections of the flow plate (COMSOL results)	66
Figure 3-6:	Flow patterns in both lateral and the transverse directions (obtained by plotting the results of COMSOL in Matlab)	67
Figure 3-7:	Gas supply module	70
Figure 3-8:	Exploded view of the back pressure regulator (BPR) assembly	73
Figure 3-9:	A typical plot of GC showing the change of concentration of oxygen with time.....	74
Figure 3-10:	Water injection System	75
Figure 3-11:	Flow chart of the experimental procedure for the diffusivity measurement.....	83

Figure 3-12: Unit element of the mesh grid	89
Figure 3-13: Diffusion coefficient versus oxygen concentration obtained as a result of the FEA based data analysis program	91
Figure 4-1: Breakthrough pressure of the hydrophobic and hydrophilic samples with different thicknesses	94
Figure 4-2: Time of breakthrough of the hydrophobic and hydrophilic samples with different thicknesses	96
Figure 4-3: SEM images (200X magnification) of Toray TGP060-0% wt. PTFE (left) and Toray TGP060-40% wt. PTFE (right).....	98
Figure 4-4: SEM images (200X magnification) of Toray TGP090-0% wt. PTFE (left) and Toray TGP090-40% wt. PTFE (right).....	98
Figure 4-5: SEM images of the TGP060-0% wt. PTFE sample that has been under compression: 200X zoom (left) and 500X zoom (right)	99
Figure 4-6: Water content inside the GDL with and without considering the expansion of flexible components for different PTFE loading and thickness level	102
Figure 4-7: Comparison between the breakthrough pressure values obtained using the first and second generation setups and those reported in [25]	104
Figure 4-8: Comparison between the time of breakthrough for GDLs with different thickness and hydrophobicity level obtained using the first and second generation setups	105
Figure 4-9: Change in the breakthrough pressure with the change in the internal contact angle. The contact angles were taken from [103].....	106
Figure 4-10: Change in the time of breakthrough with the change in the internal contact angle. The contact angles were taken from [103].....	106

Figure 4-11: SEM images of TGP060 (500X magnification left), TGP060 T6 (200X magnification middle) and TGP060 T19 (200X magnification right)	107
Figure 4-12: Change in the breakthrough pressure with the change in the mean pore diameter. The mean pore diameters were taken from [103]	108
Figure 4-13: Change in the time of breakthrough with the change in the mean pore diameter. The mean pore diameters were taken from [103]	108
Figure 4-14: Breakthrough time and pressure for E-lat carbon cloths and AvCarb P50 samples with different hydrophobicity.....	110
Figure 4-15: SEM images (200X magnification) of P50 T13 (left) and P50 T33 (right)	110
Figure 4-16: SEM images (100X magnification) of E-Lat thin, hydrophilic (left) and E-Lat thick, hydrophobic (right)	111
Figure 4-17: The output of the pressure sensor for TGP 60 40% wt. PTFE carbon paper (left) and E-lat carbon cloth (thick-hydrophobic) (right)	112
Figure 4-18: Breakthrough time and pressure for reused samples showing a shift towards hydrophilic characteristics	113
Figure 4-19: Dry diffusivity as a function of porosity (AvCarb EP40 and Toray samples). Porosity values were provided by Ballard	115
Figure 4-20: Dry diffusivity as a function of porosity (SGL samples). Porosity values are obtained from manufacturer's specification sheet.....	115
Figure 4-21: Change of diffusibility with the change of porosity for samples made by different manufacturers	117
Figure 4-22: Change of diffusivity with the change of thickness for samples made by different manufacturers. The thickness for the SGL samples are taken from manufacturer's specification sheet; while for the other samples the values were taken from [103].....	118

Figure 4-23:	Change of diffusivity with the change in the pressure difference across the GDL sample. The pressure difference is intentionally induced to see the effect of pressure gradient on diffusivity.....	119
Figure 4-24:	Comparison between the diffusivity measured here and those obtained from the theoretical correlations described in Chapter 1	121
Figure 4-25:	Comparison between the dry diffusivity results obtained here and the experimental results reported for GDL samples without MPLs in the literature	122
Figure 4-26:	Comparison between the dry diffusivity results obtained here and the experimental results reported for GDL samples including MPLs.....	123
Figure 4-27:	Difference between dry and wet diffusivity	125
Figure 4-28:	SEM images (2000X magnification) of AvCarb EP40T12-CBT18 (left) and AvCarb EP40T12-CBT30 (right).....	125
Figure 4-29:	SEM images (2000X magnification) of AvCarb EP40T12-CBT40 (left) and TGP060T19-CBT18 (right).....	126
Figure 4-30:	SEM images (200X magnification) of SGL-34BC (200X) and SGL-35 BC (200X magnification).....	126
Figure 4-31:	Wet diffusivity as a function of the internal contact angles. The contact angle values were taken from [103]	127

NOMENCLATURE

Abbreviations

PEM	Polymer electrolyte membrane
CL	Catalyst layer
GDL	Gas diffusion layer
MPL	Micro porous layer
PTFE	Polytetrafluoroethylene
SLPM	Standard liters per minute
MEA	Membrane electrode assembly
GDE	Gas diffusion electrode
SEM	Scanning electron microscope
MRI	Magnetic resonance imaging
UV	Ultra Violet
RH	Relative humidity
GDM	Gas diffusion media
EIS	Electro-chemical impedance spectroscopy
GC	Gas chromatograph
DI	De-ionized
FEP	Fluorinated ethylene propylene
CCD	Charge coupled device

PDMS	Polydimethylsiloxane
BPR	Back pressure regulator

Symbols

I	Current density (A/cm^2)
W	Power density (W/cm^2)
ΔV_{act}	Activation overpotential (V)
ΔV_{nernst}	Nernst potential (V)
ΔV_{loss}	Sum of all voltage losses (V)
R	Universal Gas Constant ($JK^{-1}mol^{-1}$)
T	Temperature (K)
α	Charge transfer co-efficient
i	Current density (A/cm^2)
i_0	Exchange current density (A/cm^2)
ΔV_{ohm}	Ohmic losses (V)
R_{total}	Total resistance (Ω)
n	Number of electrons in reaction
i_L	Limiting current density (A/cm^2)
D	Gas diffusion co-efficient (cm^2/s)
C_B	Bulk fluid concentration (mol/m^3)
ρ	Density (kg/m^3)

δ	GDL thickness (μm)
S	Saturation (%)
D_{ij}	Diffusion co-efficient of component i into j (cm^2/s)
D_{bulk}	Bulk diffusion co-efficient (cm^2/s)
D_{eff}	Effective diffusion co-efficient (cm^2/s)
ε	Porosity (%)
ε_p	Percolation threshold
V_w	Volume of water (m^3)
V_p	Volume of pore (m^3)
D_H	Hydraulic diameter (m)
v	Velocity (ms^{-1})
L_e	Entry length (m)
Kn	Knudsen number
λ	Wavelength (nm)
D_p	Characteristic length (m)
Q	Flow rate (m^3/s)
k	Permeability (m^2)
μ	Viscosity (Pa.s)
J	Diffusive molar flux ($\text{mol}/\text{s} \cdot \text{m}^2$)
$\partial\phi$	Concentration difference

δl	Thickness
γ	Surface tension (N/m)
d	Pore diameter
θ	Contact angle (degree)

ACKNOWLEDGEMENTS

I would like to offer my profound gratitude to Almighty Allah (SWT) for his blessings that provided me the strengths and opportunities to perform graduate studies at this level and for everything that I have achieved in life. I am heartily thankful to my supervisor Dr. Mina Hoorfar whose level of hard work and dedication for research can only be compared with the perpetual motion machine of first kind. I feel blessed to declare that she enhanced her role of an academic supervisor and went on to perform the role of an academic mother in my eyes.

I am thankful to Dr. Homayoun Najjaran, Dr. Vladan Prodanovic and Dr. Abbas Milani for their encouraging words and thoughtful criticism. I am indebted to my colleagues at ATFL for their support in different format at different times. Special thanks to Samuel for his assistance in my projects. I admire the analytical ability and the spirit of intellectual integrity that you possess. I will remain ever grateful to my friends Muinul Hasan Banna and Hojat Rezaei Nejad for the highest level of co-operation they provided. I appreciate the role of Ballard and its employees for letting us use their facility to develop the experimental set-up for mass transport measurement.

I am specially thankful to my mother and father for your love and encouragement. It would have been impossible to sustain away from home for so long without your emotional support and inspiration. The amount of sacrifice that you have made over the years is not possible to pay back in any extent. I am indebted to you more than you could ever imagine.

DEDICATION

To my father, Kawsar Ahmad, who had always encouraged me to pursue higher education and sacrificed so much of his energy to ensure that I receive the support I need. Thanks.

This one is solely for you, Abbu.

CHAPTER 1: INTRODUCTION

Over the last two decades, there has been an ever increasing demand for an energy source that is sustainable in nature. Hydrogen features in the vision of most scientists and engineers across the worlds who are working relentlessly to make the world a better place to live. For the same reason “Hydrogen Economy” is echoed as a renewable, green and sustainable source of energy [1-2]. The thought process of expanding hydrogen economy also brightens up the applicability of polymer electrolyte membrane (PEM) fuel cells as a zero-emission and high efficiency source of power. A PEM fuel cell is a chemical to electrical energy conversion device that utilizes hydrogen as fuel and produces power with heat and water as the only by-products (as opposed to harmful oxides produced by oil-powered energy conversion devices). The fuel cell consists of multi layers of porous media including a polymer membrane sandwiched between two porous electrodes (anode and cathode) loaded with platinum. The porous layers are sandwiched between two flow plates providing reactants (fuel and oxidant) to the electrodes where the reaction occurs. A schematic of a PEM fuel cell is presented in the next section.

Fuel cells have shown potential to replace existing stationary and portable combustion-based power generation devices. This has motivated researchers to advance the fuel cell technology. This drive has been expedited by government and industrial sectors (mainly automobile industry) due to two reasons: i) the scarcity of hydrocarbons, and ii) their harmful effects on the environment. The hydrocarbons reserve base and production is not expected to last for over. Also, burning a hydrocarbon fuel is performed at high temperature and the waste heat is rejected at low temperature to achieve maximum efficiency (i.e., limited by the Carnot efficiency which increases as the temperature difference between the hot and cold temperature sources increases).

This process produces a large amount of waste heat which is not utilized to the fullest. Burning at high temperature also increases the rate of production of harmful substances such as NO_x [3]. Thus, there is an urgent need to find a feasible alternative system to replace the hydrocarbon-based power generation devices. For all the reasons mentioned above, fuel cells have drawn much attention as a sustainable source of energy. Fuel cell provides a wide range of power without having any moving components or producing any noise. Once fuelled, it has longer runtime than most other energy conversion systems. Also, the efficiency of fuel cell is not limited by the Carnot efficiency.

Since the development of the first PEM fuel cell, a prodigious amount of research has been conducted on the membrane and electrodes (catalyst layers). The key improvements in the history of fuel cells are: i) the development of a polymer membrane with significantly low resistance [4]; and ii) the reduction of the amount of platinum (Pt) by a factor of ten which resulted in the reduction of the overall cost [5]. In essence, the performance of fuel cell is expressed in terms of current density (A/cm^2) or power density (W/cm^2). An increase in the power density means the production of the same power in a reduced active area. The reduction in the active area also results in the reduction of Pt loading and other components which ultimately reduces the size and cost of fuel cell considerably. Despite the widespread interest in fuel cells and their advantages, their performance must still be improved: the main problem associated with the fuel cell is water management [6]. In essence, excess water produced blocks the pathway of reactants towards the catalyst layer which blocks the access of the reactant gases to the reaction sites. This problem which is referred to as flooding is exasperated when more power is extracted from the cell. In essence, the production of extra power results in the production of additional water that has to be properly dealt with to continue operation. To find a solution to the

underlying problem, it is important to study the water and reactant transport mechanisms inside the internal porous network of the fuel cell. Despite various numerical models developed to illustrate the multiphase flow and transport in the cell, these mechanisms are not well understood due to the structural complexity of different layers of the cell and lack of appropriate experimental techniques. This thesis aims at developing new experimental methods that can provide basic insights into these mechanisms by measuring the transport properties of the porous structure of the fuel cell.

The basic structure and operational principle of a PEM fuel cell is explained in Section 1.1. Flooding and water management in a fuel cell is highlighted in Section 1.2. The gas diffusion layer (GDL), which is the porous media responsible for water and reactant transport, is focused in Section 1.3. The recent studies conducted on the characterization of GDLs are thoroughly reviewed in Section 1.4, where the challenges existing in the current techniques developed for the measurement of water content (referred to as saturation) and ability to diffuse reactants (referred to as diffusion) are discussed. The objective and possible contributions of this thesis related to the development of experimental techniques for characterizing transport properties of GDLs are presented in Section 1.5. Finally, the overall structure and outline of the thesis is presented in Section 1.6.

1.1 Basic Principle of PEM Fuel Cells

A PEM fuel cell is an electrochemical cell which produces electrical energy from the oxidation-reduction reaction of the reactants at the electrodes. Some similarities exist between a typical galvanic cell and a PEM fuel cell except for the fact that in a PEM fuel cell reactants are fed on a continuous basis while in a galvanic cell reactants are stored in the electrodes. A PEM

fuel cell consists of four main components. The heart of a PEM fuel cell is the membrane electrode assembly (MEA) consisting of a polymer electrolyte membrane sandwiched between two porous gas diffusion electrodes (anode and cathode). The gas diffusion electrodes (GDE) have two components: the catalyst layer where reaction takes place and the gas diffusion layer (GDL). The GDEs are surrounded by flow plates from both sides [1]. The role of each of the components is described below:

Reactants are supplied to the anode and cathode side of the cell through the flow plates which are also called the current collector plates. The flow plates are responsible for i) supplying the reactant gases uniformly across the cell, and ii) removal of excess water remaining after proper hydration of the membrane. Also, the flow plates provide a pathway for transport of electrons from the reaction zones to the external circuit connecting the anode and the cathode electrodes. There are different configurations of flow plates each of which influences the reactant and water transport in different ways. The most widely used flow plates include channels in the form of parallel, serpentine, or interdigitated configurations as shown in [7].

The reactants are transported to the catalyst layers from the flow plates through the gas diffusion layers (GDL). The role of the GDL is similar to that of the flow plate in terms of supplying reactants across the cell uniformly. The GDL is also responsible for collecting excess water from the reaction site and transferring it to the flow plate. The GDLs are generally made of a porous carbon material loaded with the hydrophobic polytetrafluoroethylene (PTFE) agent to facilitate water removal from the reaction sites. In essence, the hydrophobic pores (PTFE coated) of the GDL repel water, providing a pathway for transport of the reactants. The hydrophilic pores

(bare carbon material), on the other hand, remove the excess water from the reaction sites [5]. The GDL is the main focus of this thesis, and hence is described in detail in Section 1.3.

The core of a typical PEM fuel cell is the polymer electrolyte membrane. The most widely used material for the membrane is Nafion® which is designed by DuPont. In Nafion, the hydrogen molecule in the polyethylene chain is replaced with fluorine which results in the formation of polytetrafluoroethylene (PTFE) [8]. A sulphonic acid group (HSO_3) is then added to the basic PTFE molecule as a side chain through the process of sulphonation. The HSO_3 is ionized into the SO_3^- ion which exists at the end of the side chain. When H^+ ion, produced as a result of oxidization, comes into contact with the polymer chain, a bond is formed between the SO_3^- and H^+ ions, facilitating transport of protons from one side to the other side of the membrane (from anode to cathode side). Transport of protons is heavily influenced by the level of membrane hydration [8].

The catalyst layer is primarily formed as a mixture of the carbon powder and platinum particles. The mixture proportion is subject to the intellectual property of manufacturers. This mixture is deposited on both sides of the membrane through different techniques adopted by different manufacturers. The mixture can also be deposited on the surface of the GDL, forming the gas diffusion electrode (GDE) layer [9].

A simple schematic of the fuel cell operation is shown in Figure 1-1. Hydrogen fed to the anode flow plate passes through the GDL and eventually reaches the catalyst layer. When the hydrogen gas comes into contact with the surface of the catalyst layer, the oxidation of hydrogen takes place which results in formation of hydrogen ions (protons) and electrons. As described above, the electrolyte membrane only allows the transport of the hydrogen ions while the

electrons travel through an external circuit to the other side of the cell. The reaction occurring in the anode side can be written as

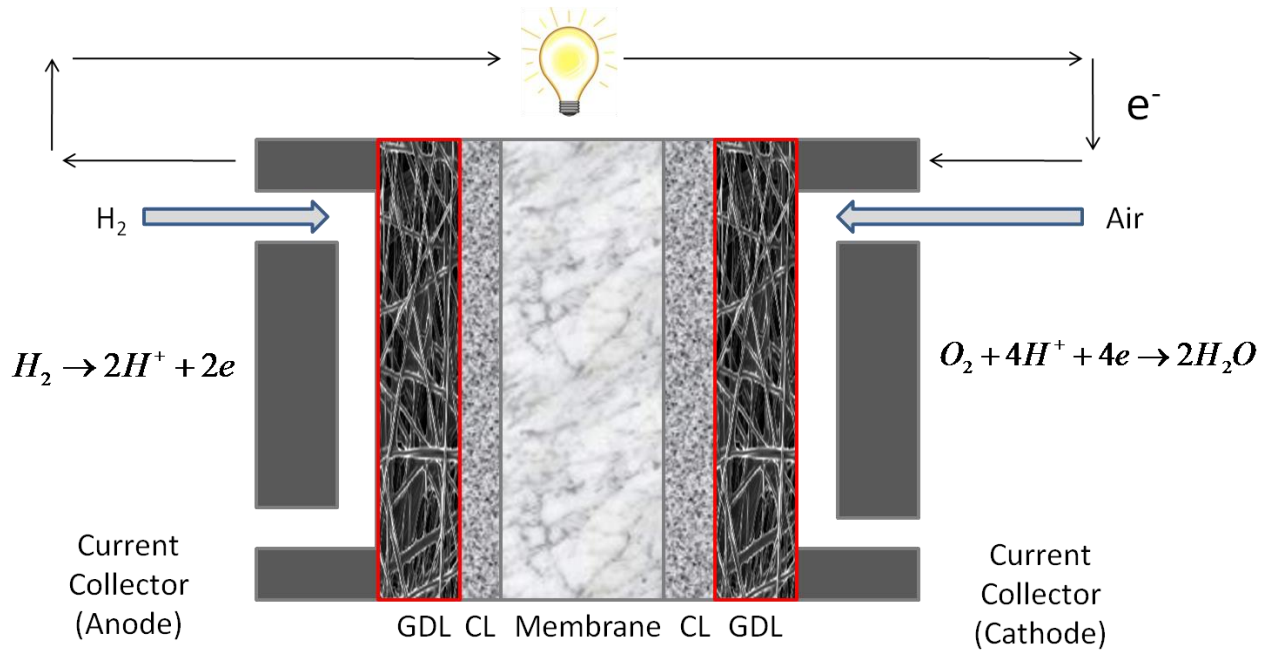


Figure 1-1: Schematic of the PEM fuel cell operation principle

In the cathode side, air (or pure oxygen) transports through the GDL to reach to the catalyst layer. At the catalyst layer-GDL interface of the cathode, H⁺ ions (transported across the membrane), O₂ (reactants at the cathode) and electrons (from the external circuit) are combined which results in an exothermic reaction producing water and heat.



Combining the reactions occurred at the anode and cathode results in the overall reaction of the cell in the following form:



The operational principle of a typical fuel cell is different than that of heat engines. Therefore, the efficiency of a fuel cell cannot be calculated based on the Carnot efficiency. The Nernst potential which is the maximum potential of an electrochemical reaction is 1.223V for fuel cells. This is supposed to be the open circuit voltage when no current is drawn from the cell. The ideal efficiency of a fuel cell can reach up to 83%. However, due to different losses occurring during the fuel cell operation the voltage and efficiency of the fuel cell is lower than the Nernst potential (V_{nernst}) and the ideal efficiency mentioned above. Thus, the actual voltage (V_{act}) of the cell can be described as

$$V_{act} = V_{nernst} - V_{loss} \quad (1.4)$$

The actual voltage depends on the amount of different losses occurred in the fuel cell. It has been observed that when the fuel cell operates at a higher current density, the value of V_{loss} approaches the value of V_{nernst} which results in close to zero voltage output. V_{loss} has three components which are significant at three periods of the fuel cell operation. At the beginning of operation, activation losses (ΔV_{act}) occur due to the sluggish electrode kinetics [8] which can be described by Tafel equation (equation 1.5) [10]. These losses depend on the catalyst material and loading at the surface of the catalyst layer. Activation losses occur at both anode and cathode, but it is more pronounced at the cathode electrode.

$$\Delta V_{act} = \frac{RT}{\alpha_a F} \ln\left(\frac{i}{i_0}\right) \quad (1.5)$$

In the above equation, ΔV_{act} is the activation overpotential in the electrode, R is the gas constant, T is the temperature, α is the charge transfer coefficient at the electrode, F is the Faradays constant, i and i_0 are the current density and the exchange current density, respectively. Once the reaction starts, the protons and electrons flow through the membrane and the external circuit. This transport is associated with losses incurred due to the resistance of the membrane and the components of the external circuit. These losses are referred to as Ohmic losses (ΔV_{ohm}) and can be found by summing the resistances (R_{total}) of all the components.

$$\Delta V_{ohm} = i * R_{total} \quad (1.6)$$

In the above equation, ΔV_{ohm} is the ohmic loss, i is the cell current density, and R_{total} represents the resistance causing the drop in the voltage drop.

Finally, when the cell is operated at a high current density, the voltage drop due to concentration losses occurs. Similar to any other catalytic reactions, the exothermic reaction that produces power in a fuel cell continues as long as there is a continuous supply of reactants. Thus, the reaction continues when both hydrogen and oxygen is supplied on a continuous basis. However, for several reasons oxygen is the limiting reactant in this reaction. One of the reasons is the low partial pressure of oxygen (due to its extraction from air and the humidification process performed for membrane hydration) which reduces the diffusion coefficient of oxygen compared to that of hydrogen. However, the most vital factor affecting the concentration losses is the production of water in the cathode side. At high current densities, excess water forms droplets blocking the pores of the GDL which eventually leads to formation of a liquid film at the catalyst layer. At this stage, the supply of the reactant to the catalyst layer in the cathode is

seized. This results in the loss of concentration at the cathode catalyst layer which is marked by a sharp drop in the performance curve of the fuel cell, referred to as the limiting current of the cell. Mass transport losses can be expressed by the equations 1.7 and equation 1.8. It is clear that these losses depend heavily on the concentration.

$$\Delta V_{conc} = \frac{RT}{nF} \ln\left(\frac{i_L}{i_L - i}\right) \quad (1.7)$$

$$i_L = \frac{nFD C_B}{\delta} \quad (1.8)$$

In the above equations, i_L is limiting current density, D is the gas diffusion coefficient, δ is the GDL thickness, n is the number of moles and C_B is the bulk concentration in the cell.

The above three sources of losses can be shown in the fuel cell performance curve which is called the polarization curve. A typical polarization curve is shown in Figure 1-2. At the low current density, the activation losses are dominant (region I). The linear section of the polarization curve corresponds to the ohmic losses (region II). The last section (region III) is due to the concentration losses where the power and the voltage both experience a significant drop. This region is also called mass transport or flooding zone which is very crucial in further advancement of the fuel cell. Majority of ongoing studies [6] are focused on delaying the start point of the concentration loss region so that fuel cell can run at a higher current density to achieve a larger power density.

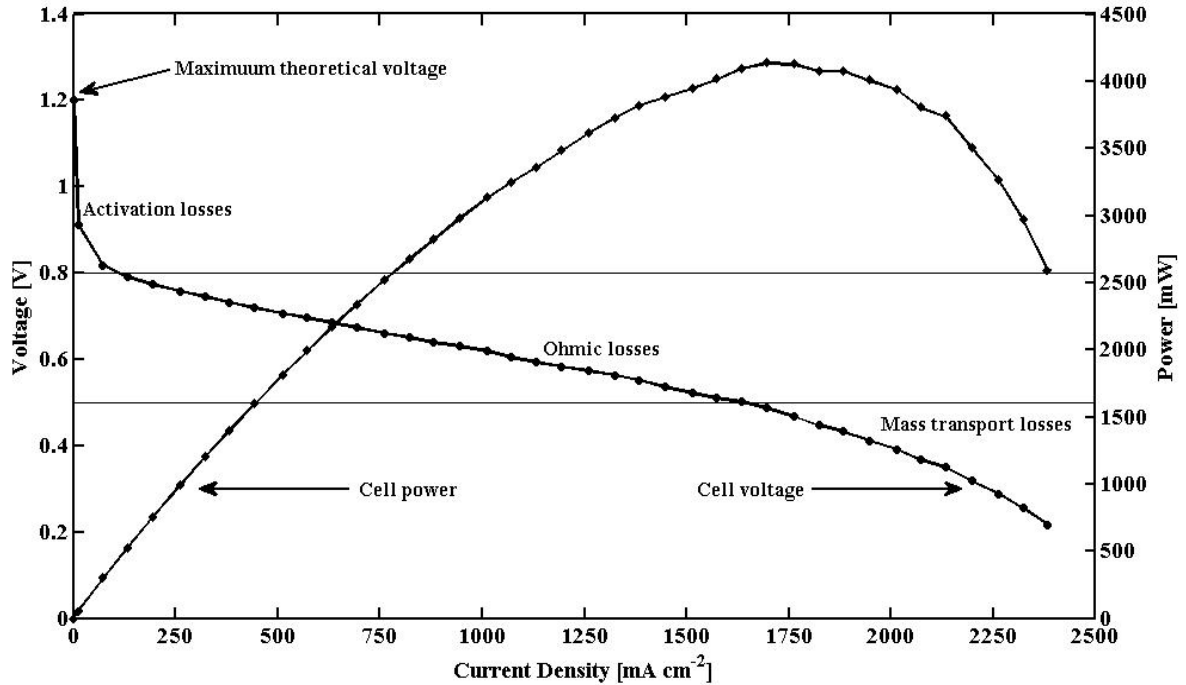


Figure 1-2: A typical polarization curve depicting the change in voltage and power for a change in current density. Different losses occurring during different regime is also highlighted.

1.2 Water Management

In the process of producing electricity, a PEM fuel cell produces water as a by-product. Removal of all the water produced is not an ideal solution as the produced water has both positive and negative effects on the overall performance. Water is crucial for membrane hydration which is quite essential for improving the performance of the ionomer membrane and consequently reducing the ohmic losses [11-12]. However, the excess water needs to be removed from the internal network of the fuel cell to avoid flooding. Finding the optimum balance which is referred to water management is a challenging task for researchers. One of the reasons is the non-uniform distribution of the humidity level and temperature across the cell. The relative humidity of the supplied air increases as it comes in contact with the water produced inside the cell. However, similar to the current distribution, the water production rate is not uniform at the

catalyst layer. As a result the air passing through the areas containing water ends up having higher humidity. Therefore, due to localized water production and the necessity to hydrate membrane, it is impossible to create an ideal uniform environment all over the cell.

Several remedies have been applied to enhance water management. These include tailoring the flow-plate [13], treating the GDL with PTFE [13], and applying micro porous layers [14]. Despite the incremental effects of these remedies, water management is still the limiting factor for the fuel cell performance. To solve systematically the water management issue, it is necessary to characterize and identify the role of important components. The main fuel cell component is the gas diffusion layer (GDL), as humidification, water and gas transport occur across this layer. Therefore, there is a need for the development of appropriate experimental techniques facilitating the characterization of the transport properties of the porous GDLs having such a structural complexity as described below.

1.3 Gas Diffusion Layer

The gas diffusion layer (GDL) provides a backing for the flexible and non-rigid membrane. This layer is also very important in terms of thermal and electrical conductivity. However, the main objective of the GDL is to distribute uniformly the reactants across the catalyst layer. Thus, the GDLs are made of porous materials from carbon fiber papers or clothes.

The thickness of a typical GDL varies between 200-400 μm , and its porosity value ranges between 70-90% [4]. Reactants are transferred across the pores while the solid matrix is used for electron transfer. The properties of the GDL need to be optimized based on the system requirements. For instance, having a higher porosity is better in terms of reactant transport, but it is not useful for electron transport. Similarly, thinner GDLs are better for both electron and

reactant transport, but it might not provide sufficient mechanical support to the membrane which is important for a number of reasons: when a fuel cell is assembled it is compressed to reduce contact resistance [3]. The GDL absorbs part of this compression and strains more than any other components. This strain causes a significant change in the morphological properties of the GDL as reported in [15]. The GDL also protects the membrane from cracking due the pressure applied from the channel ribs [8].

The GDL is usually coated with hydrophobic agents like polytetrafluoroethylene (PTFE) to improve its water handling capacity. The coating procedure depends on the manufacturer and is not usually disclosed. The basic procedure includes soaking the GDL in a liquid solution containing the hydrophobic agent. Sintering is performed at different temperatures to evenly distribute the polymer coatings. The hydrophobic agent concentration in the solution defines the final loading percentage of PTFE. Hydrophobization prevents the wicking action of the liquid water, leaving pathways for reactant transport. Figure 1-3 shows SEM images of a sample GDL.

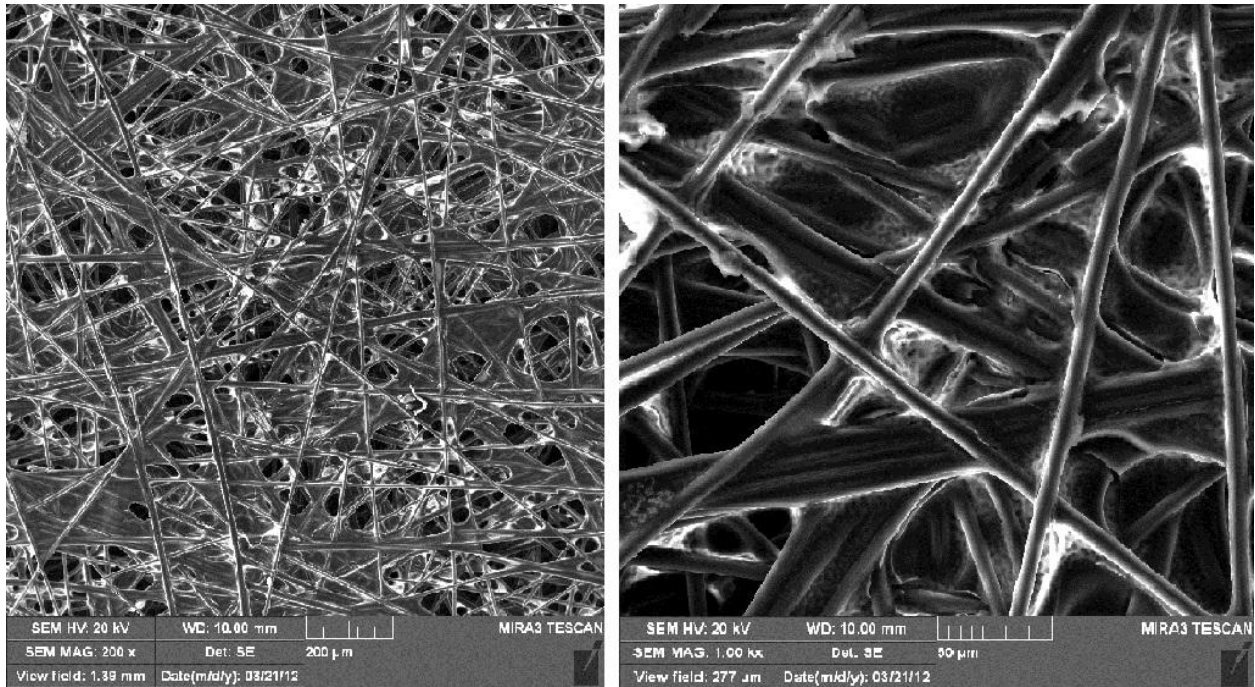


Figure 1-3: SEM images of a Toray TGP-H-060 GDL sample with 40% wt. PTFE loading: (left) 200x and (right) 1000x magnification.

To further enhance water management, a micro porous layer is added to the side of the GDL facing the catalyst layer. The MPL bridges the gap between the large-sized macro pores of the anisotropic GDL and the small-sized micro pores of the isotropic catalyst layer. The micro-porous layer (MPL) consists of amorphous mixtures of carbon black powder and PTFE particles [13]. Experimental [15-17] and numerical studies [14, 18] have shown that the use of MPL significantly improves water management and accordingly the performance of the fuel cell. Figure 1-4 shows SEM images of AvCarb EP-40 GDL with MPLs.

The main transport properties of the GDL include wettability, pore size distribution and porosity, permeability, and diffusivity. The measurement of the first three properties has been the subject of numerous studies. For instance, wettability has been measured based on i) contact angle in the form of external [3] (which is less accurate as it is affected by the roughness of the

surface) or internal like the capillary rise method [19-21] which provide a more accurate angle presenting average internal wettability; and ii) capillary pressure [22-23] which resulted in obtaining a relationship between the capillary pressure and saturation (defined as $S = \frac{\text{Volume}_{\text{water}}}{\text{Volume}_{\text{Overall pore}}}$). The overall bulk porosity and pore size distribution have been measured using common methods (including mercury and water intrusion porosimetry [24-25], Kerosene-based method [26] and porometry [27]), which only provide a quantitative measure of porosity and pore size distribution, and more complex techniques such as high resolution computer tomography [28] which has enabled the measurement of the heterogeneous through-plane porosity distribution. Permeability has extensively been measured in the two in-plane and through-plane directions to study different effects such as i) viscous and inertia permeability coefficients of macro-porous compared to micro-porous layers [29], ii) the anisotropic permeability properties of the GDL [30], iii) the effect of GDL compression [31], and iv) liquid water relative permeability for different hydrophobicity [32]. Among different GDL properties, the measurement of diffusivity has been little studied. More specifically, there is no diffusivity measurement as a function of the water content, which is crucial for studying fluid transport in fuel cells. Related to this thesis, seminal theoretical and experimental studies conducted to study water transport and content and diffusivity are presented in the following section.

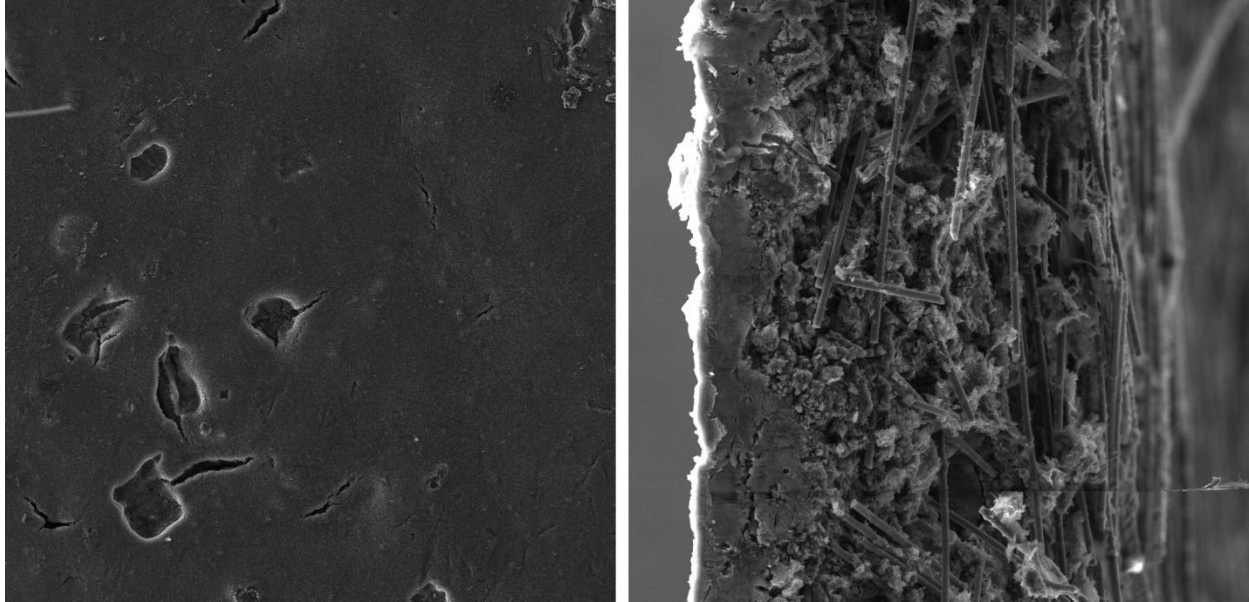


Figure 1-4: SEM image of a SGL-34BC GDL sample with MPL: (left) lateral view, (right) transverse view.

1.4 Literature Review

1.4.1 *Experimental Visualization of Water Transport in the GDL*

Liquid water is produced as the by-product of the electrochemical reaction. High humidity of the reactant gases (to increase proton conductivity in the membrane) also increases the chance of water to remain as liquid. Also, due to the temperature difference between the catalyst layer and the flow channel, water vapor may condense as it travels through the GDL and reaches the flow channels. The presence of liquid water restricts diffusive and convective transport of reactants by blocking the pores of the porous GDL which ultimately results in a sudden drop in the voltage. The negative impact of liquid water on the convective and diffusive transport has been shown using the morphology model developed by Zamel et al. [33]. Their model showed that the porosity of the GDL decreases due to the presence of liquid water which blocks species transport. This effect was found to be more pronounced in the through plane direction. However, they showed that liquid water has a positive impact on thermal transport. Due to above reasons, it

is essential to understand the water pathways inside the GDL and its transport mechanism from the catalyst layer to the flow channel. More importantly, it is necessary to quantify the amount of water that a GDL can hold before it becomes flooded. Saturation which quantifies the amount of water inside the GDL is an important parameter as it indicates the area available for gas transport [26]. A number of different experimental and numerical methods have been developed to study and quantify the water content and flow in the GDL [34]. Most recent experimental studies (relevant to this research) are presented in this section.

For visualization of flow inside the GDL or other components of the fuel cell, a number of different techniques have been successfully implemented in the past decades. These techniques include magnetic resonance imaging (MRI), neutron imaging, X-ray micro tomography, and direct visualization [35]. Using magnetic resonance imaging (MRI), particles within a strong magnetic field are excited by radio frequency signals. The response of the particles to the RF signal is then analyzed to detect the presence and location of water. MRI was successfully used by Zawodzinski et al. [36] to detect liquid water and determine the diffusion coefficient in the membrane. The same technique was used in finding the distribution of liquid water in the membrane of an operational fuel cell [37]. The results showed that the hydration level of the membrane decreases as the cell current increases. Using MRI, similar results were reported by Teranishi et al. [38] who concluded that a thick membrane is better in terms of hydration. Feindel et al. [39] used MRI to investigate the effect of the flow field configuration on liquid water distribution in the membrane and flow channels. They found that the maximum current is drawn before the liquid water is observed in the cathode flow field. As the intensity of water increased flooding occurred and the current density reached the limiting current zone rapidly [39].

Neutron imaging is another technique which was successfully used to measure the liquid water content and its local distribution. In this technique, neutron beams are passed through the samples. The presence of liquid water reduces the intensity of neutron beams [40], which can quantify the water content after proper calibration. The advantage of this method compared to other imaging techniques is that it can be used while the fuel cell is running. This technique has been used to investigate water behavior, transport and removal through different components of the fuel cell [40]. It has also been used to explore water distribution along the thickness of the electrolyte membrane [41]. Using neutron imaging, Trabold et al. [42] showed that the concentration losses occurring at high current densities is due to poor water management in the gas diffusion electrode (GDE) areas. They reported that for operating fuel cells at high current densities, the gas velocity needs to be high to remove water effectively. Similar results were reported by Turhan et al. [43] who also showed experimentally that higher inlet gas flow rates reduce water accumulation in the cell. Owejan et al. [44] also used the neutron imaging technique to investigate water transport through the GDL. To enhance transport of the reactants through the GDL, they used interdigitated flow fields. Their results demonstrated that the primary cause of flooding is droplet pinning at the interface of the channel and the manifold. Even with an interdigitated flow field, they experienced mass transport losses as the water content in the GDL increased. In a later study [13], they found that flooding is mainly responsible for the significant drop of in the voltage at high current densities. They showed [13] that the channel geometry and surface property have considerable effects on the amount of water accumulated in the cell. Their results suggested that coating the flow plates with hydrophobic agents enhances the performance at high current densities. Zhang et al. [45] performed a study on the formation and transport of liquid water through a variety of GDLs and flow-fields with

different hydrophobicity. They showed that the hydrophobicity level of the flow field controls the location of droplets formed at the interface of the GDL and the flow field. The carbon cloth GDLs were found to accumulate less water compared to the carbon papers. Their most interesting finding was the influence of liquid water on electrochemical performance. They showed that even a large amount of water does not negatively influence the fuel cell performance when pure oxygen is supplied. This is, however, in contrary to the results reported in [13]. Hickner et al. [27] also used the neutron radiography technique and reported the impact of several parameters including the current density, cell temperature, gas flow rate, and inlet gas humidity on the liquid water content in the membrane electrode assembly observed from cross-sectional view. They studied the effect of the operating temperature of the fuel cell on water condensation in the GDL. They showed that condensation occurring due to a small temperature difference has a considerable effect on the distribution of liquid water (or saturation profile). Kim and Mench [46] also used neutron imaging to find the water transport induced by phase change. They showed that in the presence of the gas phase in either the GDL or the catalyst layer, the water transport mechanism will be dominated by phase change during which water flows from the high to the cold temperature zones. Chen et al. [47] used neutron radiography to study the impact of the cathode stoichiometry ratio and relative humidity on the water content. They concluded that the anode water content tends to reduce with increasing the current density at a fully humidified condition. At smaller stoichiometry values, they reported a larger amount of water in the GDL.

Another modern technique used to investigate water saturation behaviour in the GDL is X-ray micro-tomography. The material under study is bombarded with X-ray beams attenuating differently depending on the material properties which are characterized based on the transmitted

signals detected and processed by a number of detectors positioned at different angles. This technique was used by Sinha et al. [48] to show water distribution along the thickness of GDLs. In the same study, they showed that the water evaporation rate decreases in an exponential fashion during the gas purge step. Manke et al. [49] studied the evolution and transport of water droplet using X-ray radiography in an in-situ experimental set-up. Their setup facilitated the study of the effect of the operating conditions on the growth rate of the droplets. Their results confirmed the viscous fingering pattern for water transport in the GDL during the pore filling process. A synchrotron X-ray radiography technique with a time resolution of 5 seconds was introduced by Hartnig et al. [50]. It is important to mention that the time resolution for similar techniques with such high spatial resolution is in minutes. They observed liquid water transport in the cross-sectional direction of the porous media. They showed that water droplets create two different barriers for species transport: i) under the ribs of the gas channel, and ii) close to the MPL. The location of these barriers is, however, dependent on PTFE distribution in the GDL. Büchi et al. [51] measured saturation of the GDL with three dimensional imaging facilitated by high resolution X-ray tomography. Their method which is dependent on the size of the sample overestimated saturation. The source of this error is the opaque nature of the GDL which makes it hard to estimate the liquid water content from the image intensity.

Direct visualization is another method developed for studying liquid water distribution inside PEM fuel cells. Typically, cameras with high temporal and spatial resolutions are used to visualize the flow within thin porous samples (with the thickness of 190 μm to 400 μm and porosity of 70% to 90%). However, the use of this method is limited to transparent flow fields in in-situ experiments where a microscope is used to monitor the process of droplet formation at the GDL-catalyst interface and its transport and removal through the flow-field. Tüber et al. [52]

used direct visualization to correlate the performance of the fuel cell to liquid water formation. They showed that the drop in the voltage is due to the droplets observed in the cathode flow field. They also claimed that hydrophilic GDLs (non-treated) perform better than hydrophobic GDLs (treated). Their rationale was that water is uniformly distributed in the non-treated GDLs, and hence the gas diffusion pathway is less limited compared to the treated GDLs. However, the validity of their results is questionable since their experiments were conducted for short periods (40 minutes) during which the water transport patterns in treated and non-treated GDLs are not easily distinguishable. Yang et al. [53] investigated transport of liquid water at automotive current densities (0.82 A/cm^2) using a transparent cathode cell. They showed that liquid water is distributed in a non-uniform manner across different channels in the flow plate. They also studied the pattern of droplet emergence at the interface of the flow plate and the GDL. Their effort resulted in identifying the preferential areas for the droplet growth on the surface of the GDL. Ge and Wang [54] experimentally analyzed the impact of GDL wettability on liquid water transport especially on the anode side. At low current densities, the performance of the fuel cell with the hydrophilic GDL was found to be better compared to that obtained using the hydrophobic GDL as the wicking characteristics of the hydrophilic GDL prevents water clogging the flow channel. Spornjak et al. [16] studied water transport across different GDLs with different surface properties. They found that for treated samples water is formed in the shape of droplets; while for untreated samples, films are produced. They also performed direct visualization of water transport using GDL samples including micro-porous layers (MPL). Their results show that water back diffusion from the cathode to the anode causes droplet formation in the anode side due to the very high pressure required for water to penetrate the MPL layers in the cathode. This back diffusion increased the hydration of the membrane. In a different study, the

same group used a transparent flow field and combined them with neutron imaging to separate the water content in the flow channel from that in the GDL [15]. They showed that the water distribution depends on the hydrophobicity level of the GDL pores. When hydrophilic GDLs are implemented in the fuel cell, the amount of water in the overall internal network of the fuel cell is reduced compared to the case where hydrophobic GDLs are used. However, the saturation of the hydrophilic GDL is more than that of the hydrophobic GDL, restricting reactant transport in the porous media. Their results provided general insights into water distribution in the GDL and the flow field; however, their water content measurements were not compared against any results reported in the past [52-54]. Theodorakakos et al. [55] utilized direct visualization and showed that the only mechanism for water removal from the porous media is the removal of discrete droplets formed at the surface of the GDL. Kimball et al. [56] used direct visualization to study the effect of the fuel cell orientation on water removal and overall performance. They showed that a minimum capillary pressure is required for water to penetrate the GDL. They found that droplets are connected to the liquid present in the pores through the branching mechanism. They showed that the gravitational force can enhance the water removal process if the cell is oriented properly.

The methods described so far are used for in-situ measurements. This increases the complexity of these methods and hence limits their applicability. The accuracy of the results of these methods (other than X-ray and neutron imaging) also depends on their image analysis techniques which are in general not appropriate for opaque samples like GDLs. The performance of some of these techniques has been improved by increasing their spatial resolutions. Even with this enhancement, it is still difficult to differentiate the water content in different layers of fuel cells (e.g., between the flow-plate and GDL). Also, this resolution increase significantly reduces

the imaging frequency which affects the accurate determination of water pathway in the internal network of fuel cells. For all these reasons, ex-situ measurements mimicking the real fuel cell operating conditions have drawn attention. Fluorescence microscopy is one of the ex-situ techniques successfully used to trace water motion inside the GDL. In this technique, a diluted fluorescein solution is injected into the porous sample which is illuminated by an ultraviolet (UV) light exciting the fluorescent dyes inside the solution. Due to the interaction of the UV light and the dyes, light rays are emitted at a higher wavelength than the natural light. This emitted ray is captured by a properly configured camera. Litster et al. [57] were the first who used this technique for visualization of water behavior inside the GDL. They developed an experimental setup in which the fluorescein solution was injected from the bottom surface of the GDL. The pathway of water was tracked from the top using a high resolution microscope. The images were then processed and the intensity was related to the height of the liquid column in the sample. They showed that transport inside the GDL is more dominated by branching and the viscous fingering pattern as opposed to the capillary displacement pattern proposed earlier [50]. Their method provides valuable insights into flow pattern. However, the estimation of the water content based on the intensity of the light is not accurate due to the opaque nature of the GDL. Using the same technique, Bazylak et al. [58] studied the effect of compression on the change in the GDL morphology and the cracks created under the compressed areas. These cracks create preferential pathways for water flow. They claimed that the areas under compression lose their hydrophobicity. As a result, the hydrophilic pores serve as preferential pathways for water. In another study conducted on dynamic water transport [59], the same group showed that the droplet emerge from particular locations on the surface of the GDL. They found that the location of the droplets changes in a cyclic manner. This shows that there is a continuous pathway of

water within the GDL where the pores are interconnected. All the above methods mentioned so far were used to visualize liquid water motion inside the GDL. Instead of providing a quantitative measure of the water content in the GDL, the visualization techniques provide a basic insight into distribution of liquid water inside the porous sample.

The measurement of the capillary pressure has also been the subject of study as a parameter identifying water motion inside the GDL from the macroscopic point of view [59]. The significance of the capillary pressure was emphasized by Pasaogullari and Wang [18] who studied the water transport mechanism in both the hydrophilic and hydrophobic pores and showed that capillary transport is the main mechanism for excess water removal. A number of ex-situ experimental techniques have been reported [24-25, 60-62] for the breakthrough condition during which the time and pressure required for water to travel from one side of the GDL to the other (in the through plane direction) are measured. The breakthrough condition can be detected optically where water is injected from one side and emerges in the form of a droplet from the other side of the GDL [58]. It can also be detected through the measurement of the capillary pressure as a sharp drop in the pressure will be experienced when breakthrough occurs.

Efforts have been made to find a relationship between the capillary pressure and the water content (also referred to as saturation) inside the GDL. For instance, Benziger et al. [25] investigated the effect of hydrophobic loadings on the breakthrough pressure and the water content. The latter was measured by weighing the sample on an analytical balance after the experiments, reducing the accuracy of the values reported for the water content. Gallagher et al. [23] investigated the relation between the capillary pressure and saturation (which was estimated based on weighing the sample) using a water transport plate made of a thin hydrophilic porous

carbon layer. They observed hysteresis in the capillary-pressure-versus-saturation curves which was explained due to hysteresis observed during the measurement of the advancing and receding contact angles. This hysteresis is due to the roughness of the GDL and the alignment of the carbon fibers. Casalegno et al. [63] studied the water transport mechanism across GDL samples with and without micro-porous layers (MPL) under real fuel cell operating conditions. In their setup, the sample was sandwiched between two flow channels: one was used to supply humid air; while the other was used for dry air. They defined a parameter called the water transfer coefficient which was determined based on the balance between the inlet and outlet flow during the flooding condition. They also showed that the presence of the MPL enhances water transport characteristics. Measuring the capillary pressure, Gostick et al. [24] found a difference between the liquid and gas pressure for the entire range of the saturation values obtained by weighing the sample using an analytical balance. Their results demonstrated significant hysteresis between the liquid and gas intrusion steps. The same group also developed a setup facilitating the simultaneous measurement of the capillary pressure and saturation [26, 60]. In their setup, the sample was placed upside down where the water was injected from the top surface, and droplets detached from the bottom surface were collected on the balance placed underneath the sample. Saturation inside the GDL at each instant was estimated based on the flow rate of the injected water and the volume of the droplets detached from the sample. However, they ignored the volume of the droplet remained on the surface of the GDL after detachment as well as the effect of expansion of setup components. They used this setup to study the role of the MPL on saturation. The results showed that the saturation value in the GDL drops from 27% to 5% at the presence of the MPL. They suggested that this reduction is due to fact that once the MPL is added the probability of water invading the dead-end pores decreases significantly. They also

studied [26] the effect of GDL hydrophobicity on saturation and the capillary pressure. Their results suggested that the saturation of the hydrophilic sample is more than that of the hydrophobic sample. Shahraeeni and Hoorfar [62] adopted a fluorescence microscopy technique to analyze the behavior of liquid water. They reported the time of breakthrough for GDLs with different thicknesses and PTFE loadings. Their results showed that hydrophobic samples have a large number of pores for reactant transport during the water filling process. Their experiments also indicated that the capillary pressure is related to the time of breakthrough, and both are larger for the hydrophobic samples. They concluded that the estimation of saturation from the flow rate produces erroneous results as the flow rate will not be same across the hydrophobic and hydrophilic samples. However, they did not consider the effect of the expansion of the setup components. Despite prodigious amounts of experimental studies conducted for understanding water transport in the GDL, there is still a need for the development of appropriate setups facilitating the measurement of the water content as a function of the GDL properties (including the capillary pressure which is related to the structural properties of the GDL).

1.4.2 Theoretical and Experimental Estimation of Gas Diffusivity in the GDL

In a PEM fuel cell, the reactants (oxygen and hydrogen) are supplied in their gaseous form. The gas molecules experience small intermolecular cohesive forces which cause them to move in a random (Brownian) motion. This motion originated due to the difference in the concentration is called diffusion which is influenced by temperature [64]. The parameter that defines diffusion in a medium is called the diffusion coefficient. Thomas Graham (early 1800) was the first scientist who performed experiments measuring diffusion in a quantitative manner [64]. The theory of diffusion, however, was proposed by Adolf Eugen Fick in the late 19th century [64]. In the same century, Johann Joseph Loschmidt also measured diffusion for different gas pairs [64].

The diffusion coefficient, which is a measure of the rate of diffusion, depends on the medium structural properties and the gas passed through the medium. A binary mixture is usually used to estimate the rate of diffusion of gas i into gas j . In this case, this coefficient is called the binary diffusion coefficient (D_{ij}). When diffusion takes place in the absence of any medium, the coefficient is called the bulk diffusion coefficient (D_{bulk}). In majority of cases, however, diffusion is obstructed by a medium, mostly a porous structure. Typical examples of porous media, through which diffusion is important, are composites, sandstone, soil, catalysts and textile products. These structures reduce the diffusion rate due to their porous nature which reduces the available area. This reduction depends on the porosity and tortuosity of the medium. In a number of different industries, the measurement of the diffusion coefficient for a specific porous medium and gas pair is of particular interest (e.g., intrusion of the gas in an oil reservoir to facilitate the extraction of hydrocarbon). The coefficient of diffusion or diffusivity is also essential in modeling of fluid transport through the medium of interest [61].

Diffusion plays an important role in reactant transport in PEM fuel cells. Both reactants (hydrogen at the anode and oxygen at the cathode) reach the reaction sites through porous GDLs. This transport is mostly dominated by diffusion due to the difference in the reactant concentrations across the GDL [65]; whereas convection occurring in the flow field enhances the overall transport process [66]. In the course of flooding, liquid water blocks the GDL pores through which oxygen diffuses to reach the reaction site. In order to design more effective porous structures with enhanced mass transport properties, it is crucial to estimate the rate of diffusion as a function of GDL saturation. In the fuel cell literature, diffusion in the GDL is measured in terms of diffusivity or the effective diffusion coefficient (D_{eff}). Despite the importance of this parameter, the measurement of diffusion in the GDL has been limited to either

theoretical models which all over-predict the diffusion coefficient [67] or a few ex-situ experimental methods [65, 68-70] which do not consider the effect of GDL saturation on diffusion. The following sections review the theoretical and experimental efforts made to estimate diffusivity in porous media.

1.4.2.1 Theoretical Estimation

The Bruggeman approximation [67] has been used for a long time for estimating diffusivity and conductivity in the catalyst layers and GDLs of PEM fuel cells.

$$D_{eff} = \varepsilon^{1.5} D_{bulk} \quad (1.9)$$

In this equation, ε presents porosity of the medium. In recent studies, it has been shown that the above equation over predicts the effective diffusivity coefficient for the GDL [65]. Thus, efforts have been made to improve the Bruggeman's correlation by capturing the structural complexity of the GDL. These efforts include the work of Tomadakis and Sotirchos [71] in which a percolation model was used to define the effective diffusivity coefficient (D_{eff}) as

$$D_{eff} = D_b \varepsilon \left(\frac{\varepsilon - \varepsilon_p}{1 - \varepsilon_p} \right)^\alpha \quad (1.10)$$

Where, D_b is bulk diffusivity, ε is porosity, ε_p is the percolation threshold which has a typical value of 0.037, and α is an empirical constant with a value of 0.661. Based on the relation of Tomadakis and Sotirchos, Nam and Kaviani [72] developed a pore network model simulating liquid water distribution in anisotropic porous structures. However, similar to the Bruggemen approximation [67], these models were found to over predict the diffusion coefficient. Neale and

Nader [73] suggested the following relationship for estimating the effective diffusion coefficient. There estimation was based on homogenous and isotropic swarm of impermeable spheres which do not capture the GDL structure.

$$D_{eff} = D_b \frac{2\varepsilon}{3 - \varepsilon} \quad (1.11)$$

Mezedur et al. [66] developed a two dimensional “ordered and random” lattice network model to estimate the effective diffusivity of constituents involved in a catalytic converter. Their model was also not derived for a porous medium like GDL. They suggested the following relation for the measurement of diffusivity in porous media:

$$D_{eff} = D_b(1 - (1 - \varepsilon)^{0.46}) \quad (1.12)$$

Using a finite element method in conjunction with a parametric analysis, Mu et al. [74] suggested a relation between the gas effective diffusivity and micro-scale features of the porous solid. They also presented the linear and quasi-linear relationship between diffusivity and porosity. Based on Hashin coated sphere model and Hashin bound [75], Das et al. [76] proposed a formulation for the diffusive transport coefficient for GDLs and catalyst layers (see Eq. (1.11)). They accounted for the pore size distribution by modifying the Knudsen coefficient [64]. However, their models are highly uncertain due to the randomness of the geometry.

$$D_i^{eff} = \left(1 - \left(\frac{3(1 - \varepsilon)}{3 - \varepsilon}\right)\right) D_i^{bulk} \quad (1.13)$$

All the models described so far are more suitable for porous media like rocks and sandstones. To capture the GDL fibrous structure, Zamel et al. [77] used a stochastic model and presented

the following relationship for the estimation of the effective diffusion coefficient. Their models predict the diffusivity of GDLs well [78], but they are not suitable for small pores of MPLs.

$$D_{eff} = \left\{ 1 - 2.76 \varepsilon \cosh(3\varepsilon - 1.92) \left[\frac{3(1 - \varepsilon)}{3 - \varepsilon} \right] \right\} D_{bulk} \quad (1.14)$$

In general, the porous structure of the GDL is really complex as it consists of randomly distributed cylindrical carbon fibers coated with the hydrophobic agent. Thus, a more accurate diffusivity relationship including the effect of shape factors, such as tortuosity, is needed to capture the structural complexity of this layer.

1.4.2.2 Experimental Measurement

A few experimental approaches have been reported for the measurement of diffusivity in the porous materials of PEM fuel cells. Related to the proposed research, this section presents a review of the ex-situ experimental methods developed to study the effect of different parameters (e.g., hydrophobic loadings, humidity and temperature) on diffusivity of GDLs.

Using humidity and oxygen sensors installed in a Loschmidt cell apparatus [79], Zamel et al. [68] determined the diffusion coefficient for different GDLs based on Fick's law [80] and the measured concentration gradient of the oxygen and water vapor. In their diffusivity measurement, however, they did not consider the presence of liquid water, and hence ignored the relation between diffusivity and saturation. They showed that the diffusion coefficient is affected by the percentage of the hydrophobic loading, but not significantly by the change in temperature. On the other hand, the bulk diffusion coefficient was shown to be sensitive to temperature. Their experimental results were in agreement with those obtained from their 3D numerical simulation

[77]. A similar setup was used by Chan et al. [78] to estimate the diffusion coefficient in the presence of the micro-porous layer (MPL). Their results showed that for the GDL samples loaded with MPLs Knudsen diffusion [81] (which results from the molecule-wall interaction as opposed to molecule-molecule interaction causing molecular diffusion) dominates the transport mechanism, reducing the diffusion coefficient by 79% (compared to the GDL without the MPL). The Loschmidt cell was also employed by Astrath et al. [82] who studied the effect of temperature and humidity on diffusion. They found that vapor diffusion can be ignored in the O₂-N₂-water vapor mixture, and hence the diffusion process becomes binary diffusion between O₂ and N₂. The diffusion coefficient seemed to increase with the increase in the temperature and relative humidity (RH). They used the generalized Schettler and Giddings (FSG) empirical equation [83] derived based on the kinetic theory of gases to find a relation between the diffusion coefficient and relative humidity.

Quick et al. [84] developed an ex-situ experimental setup to investigate the diffusion properties of GDLs. They used the GDL as a spacer separating the liquid water phase from the vapour phase. The transport rate of water vapour (estimated based on the rate of water loss in the liquid phase) through the GDL was measured as a function of the air flow. Casalegno et al. [63] used the setup presented in Section 1.4.1 to estimate water vapor diffusivity. They showed that during flooding the water vapor diffusion coefficient decreases more in the bare GDL compared to the sample having MPLs.

Yu and Carter [85] experimentally measured diffusivity in gas diffusion electrodes (GDE) at fuel cell operating conditions (RH and temperature). Their setup consisted of three parallel channels: nitrogen was fed through the middle channel; while air flew in the two side channels.

They assumed that the diffusion coefficient depends on the material and the value of D_{eff} remain the same in both in-plane and through-plane directions for a porous media like GDL. Thus, they measured D_{eff} only in the in-plane direction. Oxygen diffuses across the porous layer from the air to the nitrogen channel due to the concentration gradient measured by implementing an oxygen sensor in the nitrogen channel. Their experimental results indicated that unlike porosity the oxygen effective diffusion coefficient dropped significantly as the ratio of the ionomer weight to the carbon weight was increased. This indicates an increase in tortuosity. They concluded that the Bruggeman correlation over predicts the diffusion coefficient as it ignores the tortuosity effect. They also studied the effect of RH on diffusivity. The results showed that the diffusion coefficient reduced gradually as RH was increased. Utaka et al. [86] used a galvanic cell integrated with an oxygen sensor to measure oxygen diffusivity in the micro porous layers (MPL). The electrochemical reaction that takes place inside the galvanic cell leads to the production of water which fills the pores of the MPL. The electromotive force of the galvanic cell produced an output current which was used to find the oxygen mass fraction in the porous specimen. Their results also demonstrated tortuosity in the GDL structure and the anisotropic nature of the GDLs by comparing in-plane and through plane diffusivity values. They showed that in-plane diffusivity is higher than through-plane diffusivity, in contrast to the results reported by Yu and Carter [85] who assumed that in-plane and through-plane diffusivity are the same.

Baker et al. [87] estimated the diffusion coefficient in the through-plane direction using a diffusion cell in which a diffusive flow of water vapor through the GDL was measured. Their results showed the relationship between the rate of liquid evaporation and diffusivity. In an extension to this work, Baker et al. [88] measured the resistance to oxygen transport in the fuel

cell using the limiting current method (an in-situ technique). They also separated the contributions of different components (i.e., the flow plate, GDL, MPL) in the total oxygen transport resistance. It was shown that the GDL causes the most resistance followed by the flow channel. However, the separation of the GDL diffusion resistance from that of the electrode was difficult to achieve. In addition, they showed the effect of the pressure difference on the intermolecular diffusion and the Knudsen diffusion. Stumper et al. [89] used the limiting current approach to estimate the electrode diffusion coefficient. They established a correlation between Fick's law and the current density which yielded the value of GDL diffusivity. Using the limiting current approach, Beuscher [90] also conducted the in-situ measurement to determine the diffusion coefficient. His method is more accurate than the previous in-situ measurements conducted using the limiting current approach, as it can predict the changes in the mass transport resistance due to the changes in the cell temperature, carrier gas or gas diffusion media (GDM). He also showed the contribution of the different components of the fuel cell (i.e., GDM, catalyst layer, flow field, etc.) on the overall mass transport resistance. The results revealed that the catalyst layer has considerable resistance to mass transport.

Kramer et al. [65] measured diffusivity using the electrochemical impedance spectroscopy (EIS) technique. Their method was based on the measurement of the effective ionic conductivity of GDLs soaked in an electrolyte. The analogy between Fick's law and Ohm's law was used to estimate the effective diffusion coefficient. The GDL anisotropic characteristics and the effect of compression on the diffusion coefficient were investigated. Similar to [65], Flückiger et al. [91] used EIS to find diffusivity for different commercially available GDLs. They investigated the effect of anisotropy, binder structure, PTFE, and compression. It was found that the addition of PTFE has a positive impact on water removal, but a negative impact on porosity, tortuosity and

the gas diffusion process. The smaller the amount of the binder, the larger the gas diffusion rate. Becker et al. [81] investigated the GDL transport properties like diffusivity, permeability and conductivity using both experimental and numerical methods. They took into account the changes in the above parameters due to compression of the GDL. To represent the real inner structure of a porous media for their modelling, they used the images obtained from synchrotron-based phase contrast X-ray tomographic microscopy (PCXTM). Partial differential equations of the flow and transport processes, involving diffusion and conduction of electrons, were then applied to the images to estimate diffusivity, permeability and conductivity. For their experimental approach, they used EIS developed by [65] to estimate diffusivity. They found a good agreement between the results obtained from numerical simulation, tomographic imaging, theoretical models and EIS measurements.

Adopting from textile industry, Lamanna and Kandlikar [69] developed an ex-situ experimental setup for estimating the diffusion coefficient of water vapour in the GDL. A straight channel was used to avoid the difficulties stemming from serpentine channels. The setup was used to study the impact of the MPL coating, GDL thickness and PTFE loading on the diffusion coefficient. Their results showed that the presence of the MPL significantly decreased the average pore diameter and increased the diffusion length. The PTFE loading reduced porosity and added more tortuosity; while the effect of the thickness found to be negligible. Although their measurements were conducted at the fuel cell operating temperature and pressure, their experimental results were in agreement with the results of Zamel et al [68] and Flückiger et al [91].

Pant et al. [70] developed a counter-diffusion based diffusion experimental technique. Their set-up is distinct in the sense that it can be used to study pure diffusion as well as convection diffusion. The measurement of the latter can be used to estimate permeability [92]. In their setup, the GDL was placed between two flow channels carrying oxygen and nitrogen. Two mass flow controllers were used to regulate the flow through the porous medium. Pressure transducers were employed for the measurement of the pressure across the porous assembly. A gas chromatograph was used to analyze the oxygen concentration in the outlet. They showed that their experimental results were in agreement with those reported by Zamel et al. [68] as well as those obtained from Fick's and Darcy's laws integrated with the Binary friction model. Another significant contribution of their work is the development of a mathematical model describing multicomponent mass transport. They assumed the porous media as an agglomeration of dust particles which are held close to each other by applying a clamping force. To overcome the shortcomings of the previous models [67, 71-72], they considered all the driving and friction forces playing important roles in gas transport across porous media. Their model is capable of predicting transport in the Knudsen, transition and continuum ranges [93]. They also implemented their model to predict the Knudsen diffusivity for smaller MPL pores [94].

1.5 Objective

The main objective of the research presented in this thesis is to provide a better understanding of the transport phenomena inside the GDL. Both water and reactant transport mechanisms are studied to facilitate future design improvements leading to higher performance. The GDL transport parameters measured in this thesis can also be used to enhance the accuracy of the numerical models developed.

To understand liquid water transport and flooding phenomenon, an ex-situ experimental setup originally developed by Shahraeni and Hoorfar [62] will be used. Key parameters (breakthrough time, breakthrough pressure and saturation) associated directly with the water management capability of the GDL are studied for a wide range of samples having different thicknesses and hydrophobicity levels. The errors associated with this type of measurements will be analyzed and possible solutions are introduced.

To study mass transport of oxygen in the porous GDL, an experimental setup is developed based on the counter-diffusion technique. The setup is equipped with peripheral devices to restrict the transport mechanism to pure diffusion. The effective diffusion coefficient will be measured for a number of different GDL samples with MPLs having different porosity and hydrophobicity levels. For the first time in the fuel cell research, diffusivity in wet samples, crucial to study transport in the flooding condition, will be measured.

1.6 Structure of the Thesis

The thesis consists of five chapters. The first chapter briefly describes the basic principle of PEM fuel cells, the losses associated with its operation, and the key limiting factors restricting the fuel cell performance. A comprehensive literature review is also presented followed by the objective and contribution of this research. In Chapter 2, the setup used for the measurement of the water content in the GDL is presented. The calibration and limitations of the technique are described in details. In Chapter 3, the experimental setup developed for the measurement of the effective diffusion coefficient is presented. The setup components, the experimental procedure, the model developed for data interpretation are elaborated. In Chapter 4, the results obtained from these two experimental setups (presented in Chapters 2 and 3) are shown and discussed

using the SEM images which provide a better insight into the structural and transport properties of the samples tested. Finally, the key findings of this research are highlighted in Chapter 5 which finishes with possible future work.

CHAPTER 2: EXPERIMENTAL SETUP FOR STUDYING WATER TRANSPORT IN GAS DIFFUSION LAYER (GDL)

The gas diffusion layer is a key element for water management in PEM fuel cells. The importance of GDLs in flooding and water management is already emphasized in Chapter 1. To enhance water management, it is crucial to characterize water retaining ability of the GDL. The water retaining ability of a GDL is expressed in terms of saturation which presents the percentage of the void space filled with water. The relation for the calculation of saturation is [26]

$$Saturation = \frac{V_w}{V_p} \quad (2.1)$$

where, V_w and V_p present the total volumes of water and pore, respectively.

The GDL serves as a link between the catalyst layer and the flow plate. A portion of the water produced as a byproduct of the oxidation-reduction reaction diffuses in the membrane (enhancing membrane conductivity); while the rest is drained from the reaction site through the GDL. In this research, the water drainage capacity of a GDL is studied using an ex-situ experimental technique in which water is injected from the bottom surface of the GDL. This arrangement eliminates the effect of gravity on water transport. The bottom side of the GDL represents the catalyst layer where water is produced. The water finds its pathway along the thickness of the sample while travels in both the transverse and lateral directions before breaking through the top surface of the sample. The top surface is open to atmosphere, similar to air breathing fuel cells.

In addition to the measurement of the water content (or saturation), the breakthrough time and pressure will be measured for different GDLs using the ex-situ experimental setup explained in this chapter. The setup was constructed in two phases. The intrinsic problems in the original setup (referred to as the first generation setup) are found to have significant impacts on the final results. Thus, a second generation of the setup is developed with a similar concept, but without the shortcomings.

The structure of this chapter is as follows: The first generation setup is discussed in Section 2.1. Fluorescence microscopy adopted for visualization is discussed in Section 2.1.1. The water injection, calibration, and experimental procedures are discussed in Sections 2.1.2, 2.1.3, and 2.1.4, respectively. The limitations of the first generation setup are highlighted in section 2.1.5. Finally, the second generation setup is presented in section 2.2.

2.1 Experimental Setup (First Generation)

The first generation of the setup was developed based on the method proposed by Shahraeeni and Hoorfar [62]. The setup consists of three main modules: the injection system, the image acquisition system, the sensors and the data acquisition system (see Figure 2-1). The injection module consists of a syringe pump, a 2.5-ml Hamilton glass syringe, an injection channel and tubing. The fluorescein solution (0.05g of the fluorescent salt dissolved in 150mL of DI water) is injected into the GDL using a syringe pump (kdScientific 270). The use of the fluorescein solution enables tracing of water as it flows through the GDL. This solution is particularly useful for visualization and detection of the water droplet breaking through the top surface of the GDL. Fluorinated ethylene propylene (FEP) tubing is used to connect the syringe to the injection unit. To measure the capillary pressure, a pressure transducer was inserted very close to the platform

where the sample is placed. Two micro-needles were inserted in the injection channel. The first needle was connected to a voltage source. The signal from the second needle (i.e., very close to the sample) indicates the moment that the water reaches the GDL. This signal, recorded using a PASCO data acquisition board integrated with DATAVIEW software, is used to start the image acquisition process. The water pathway through the GDL is captured using a vertical camera which is also equipped with an ultraviolet (UV) illumination hardware elaborated in the following section.

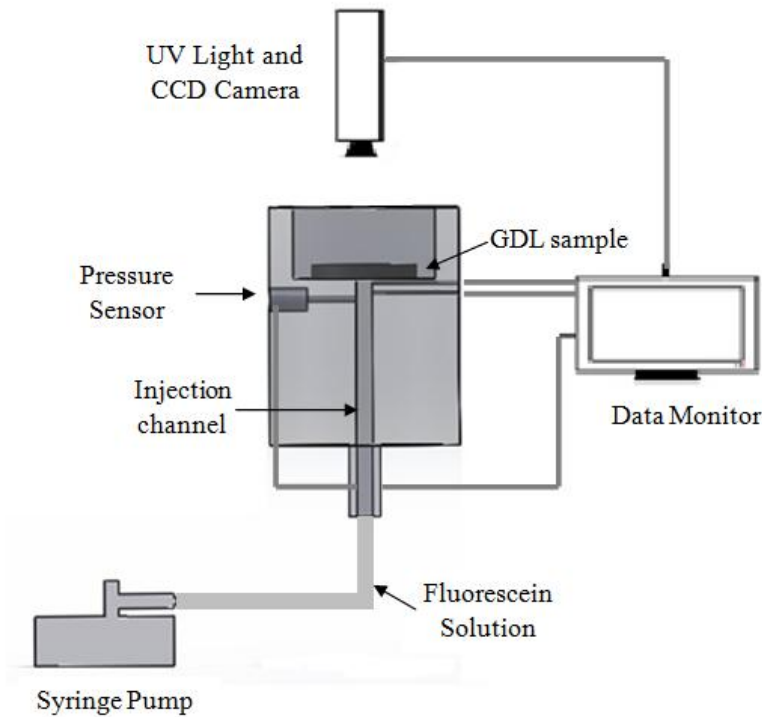


Figure 2-1: Schematic of the first generation setup developed based on the method reported in [62]

2.1.1 Fluorescence Microscopy

The fluorescence microscopy technique is adopted to study water movement through the GDL. The fluorescent dye mixed with water is injected into an object which is illuminated with

lights of two different wavelengths and intensity. If the emitted light is configured properly, the areas covered with the fluorescein solution produce a contrast against other areas in the background [95]. A schematic of fluorescence microscopy employed here is shown in Figure 2.2. The central component is a reflected light microscope. The main feature of this microscope is that the reflected light has a longer wavelength than that of the excitation light. An arc discharging lamp is used to produce multi-spectral light at different wavelengths (UV light). This spectrum is passed through an excitation filter, allowing lights of specific wavelengths to pass through while stopping unwanted wavelengths. Wavelengths that pass through the excitation filter fall upon a dichoric mirror positioned at 45° angle facing the excitation filter and the specimen. Thus, the specimen is irradiated with lights of a permissible wavelength. When the incident wavelength interacts with the specimen, the emitted light returns to the CCD camera through the dichoric mirror. A barrier filter is used to filter unwanted light signals from the emitted light before it eventually reaches the eye-piece via the CCD camera.

The setup uses a UV light source (EXFO X-Cite 120Q Mercury halide short arc) producing UV rays with the wavelengths in the range of 400nm to 600nm. The light produced is then passed through a 490-nm excitation filter within the illuminator section. When the light reflects on the mirror and eventually falls on the GDL specimen, it interacts with the fluorescein solution. As a result, the fluorescent dyes are excited and the light ray is emitted by the GDL specimen. This ray is filtered in a 550-nm barrier filter before it is finally processed by the CCD camera (Leica DFC 340 FX) connected to a vertical APO zoom microscope. The microscope is connected to an extension tube (HCL 2TU 1.25X) shifting the range of the working distance. For all the images captured by this camera, a magnification of 16X is used which results in a field of view of 8.01mm×6.01mm. The resolution for this arrangement was 200 pixel/mm. With this

arrangement, a large portion of the GDL can be captured at a reasonable magnification. The exposure time is also important in terms of image quality and post analysis. The areas covered with the fluorescein solution are appeared as very bright spots on the dark (black-shaded) background of the carbon paper GDLs. Therefore, the images might be bleached out if the exposure time is too long. On the other hand, the areas where the fluorescent concentration is low may not appear in the images if the exposure time is too short. Therefore, an optimum exposure time of 39ms was selected based on trial and error to capture the droplet profile (after breakthrough) without bleaching out the image.

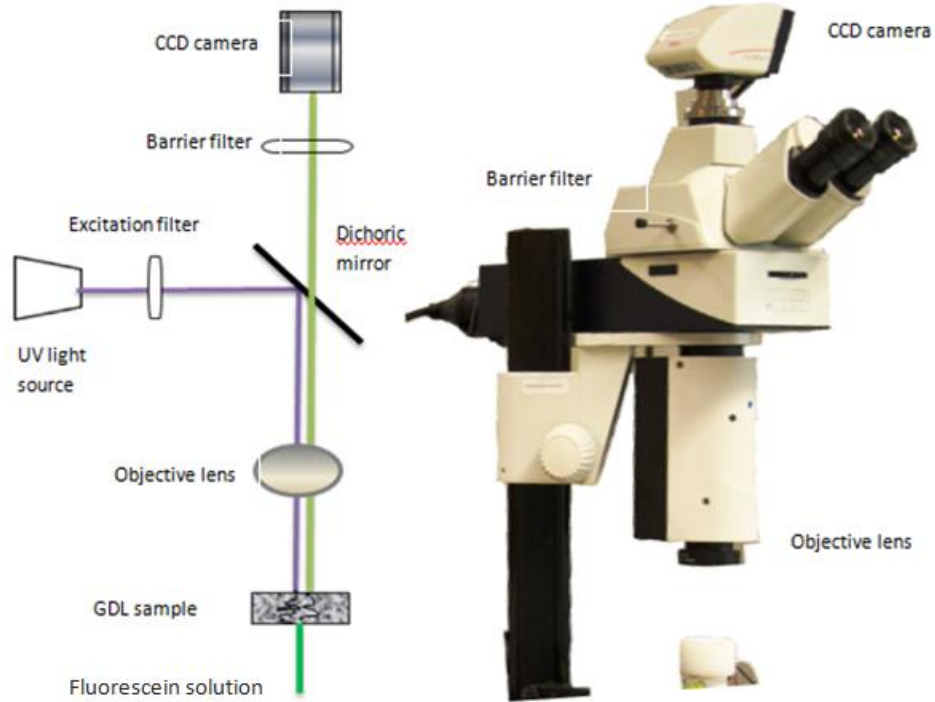


Figure 2-2: Fluorescence microscopy and the different components of the microscope used for top view imaging

2.1.2 Water Injection

The water injection pathway is shown in Figure 2.3. The 2.5-ml Luer Tip (LT) Hamilton glass syringe is first filled with the fluorescein solution prepared by mixing a very small quantity of the fluorescence salt (F6377 purchased from SIGMA-ALDRICH) with DI water. The tube is then attached to the tip of the syringe and also filled with the fluorescein solution. Usually, bubbles exist in the syringe and the tubing after filling them with the solution. These bubbles introduce errors in the measurement. In essence, the syringe pump experiences back pressure when water touches the surface of the GDL. When there are bubbles in the tubing or the syringe, they are compressed before water penetrates into the GDL. The measured breakthrough time and pressure will be affected by the time and pressure required for compressing the bubbles. Therefore, extra care must be taken to remove the bubbles before connecting the tube to the setup.

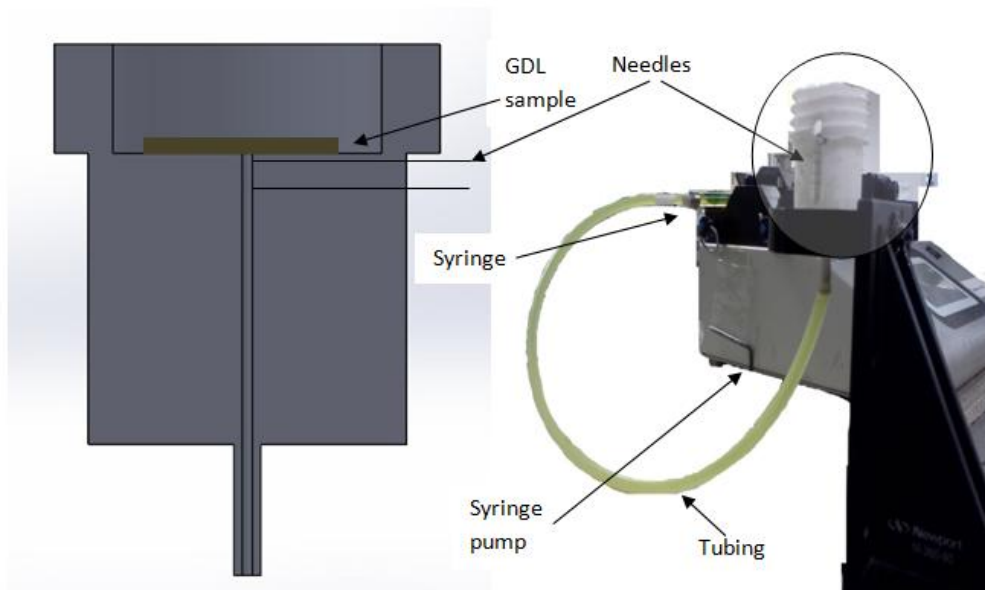


Figure 2-3: A sectional view of the experimental setup (left) and the first generation setup developed to study water transport in GDL (right)

The water injection channel with the diameter of 3 mm is drilled in a Teflon block (ASTM D 1710). One side of this channel is connected to the tubing while the other side is open to atmosphere where the GDL is placed. As explained above, two micro-needles (300 μ m each) are also inserted in the channel. Teflon is selected due to its hydrophobicity. The GDL is placed on the surface of the injection channel and pressurized from the top using a PTFE cylinder to ensure water penetration into the GDL and prevent possible leakage underneath the surface of the GDL. It has been observed that for hydrophobic GDL samples, the pressure from the PTFE cylinder is not enough to avoid leakage even with having a hydrophobic Teflon surface underneath the sample. The reason for this leakage is that even with pressurizing the sample there will be a gap between the sample and the solid surface of the Teflon block. Water tends to travel through a path that requires a minimum pressure. For hydrophobic samples (or samples with micro-porous layers (MLP), the pressure required for water to penetrate the GDL is significantly large than that required to leak on the Teflon surface. To avoid this problem, a hydrophobic flexible layer is required to coat the surface of the Teflon block where the GDL sample is placed. As the sample is pressurized, this flexible layer will be compressed which will reduce (or even eliminate) the gap between the surface and the sample. As a result, the water is forced to penetrate through the GDL.

Polydimethylsiloxane (PDMS) is used to coat the surface of the Teflon block. PDMS is a transparent, flexible elastomer that is widely used as a dielectric material in the microelectromechanical (MEMS) devices [96]. A viscous PDMS solution is made by mixing 184 Sylgard silicone elastomer gels (purchased from DOW CORNING) with its curing agent at a 10:1 ratio by volume. After pouring the solution on the surface, the setup is left for 7 days to cure in the room temperature. The curing process can be sped up by increasing the temperature.

However, high temperature may loosen up the micro-needles and create passages for the leakage. The flexibility of PDMS also prevents the GDL sample from breaking under the pressure inserted from the PTFE cylinder. One of the drawbacks of using PDMS, however, is that it slightly expands when the system is under high pressure. Although the thickness of the PDMS layer is considered in the estimation of the time of breakthrough (see Section 2.1.3.2), the impact of its expansion is very difficult, if not impossible, to calibrate and hence it is ignored. Another problem associated with the use of PDMS is that the fluorescein solution decays the PDMS layer. As a result, the PDMS layer needs to be replaced after every ten runs of experiments.

2.1.3 Calibration

The setup is calibrated for i) the pressure sensor, ii) the distance between the last micro-needle and the GDL bottom surface and the thickness of the PDMS layer, iii) the expansion of the flexible tubing. The calibration of the pressure sensor is required to convert the voltage signal output to the capillary pressure. Also, the time of breakthrough is measured from the moment the liquid touches the last micro-needle till the droplet emerges from the top surface of the GDL (which is visualized by fluorescence microscopy). However, there is a distance between the GDL bottom surface and the last needle. The time required for water to travel this distance must be considered in the final calculation of the time of breakthrough. The thickness of the PDMS layer (as explained in the previous section) also has to be accounted for while calculating the time of breakthrough. Finally, the pressure build-up in the system due to water penetration into the GDL samples (especially hydrophobic samples or samples with MPLs) expands the flexible components of the setup. The amount of water and time that contributes to this expansion needs to be considered in the calculations. The above three calibration steps are explained below:

2.1.3.1 Pressure sensor

The pressure measured in this experiment is the gage pressure between the water inside the injection channel and the atmosphere. The sensor chosen is a standard gage pressure measuring sensor (purchased from Sensortech, model RPOM050G6H) which can also be used in wet conditions. The input port of the sensor has a M5 thread that is connected directly to the setup. 10V-DC power is supplied at the measuring port which operates like a Wheatstone bridge with a variable resistor changing based on the pressure experienced. The output signal (which is in millivolts) is recorded using DATAVIEW software. This output signal is proportional to the capillary pressure required for water to penetrate the GDL sample. In essence, the capillary pressure and hence the voltage output of the sensor are negligible and remain constant as long as water does not come into contact with the GDL. However, as soon as water touches the GDL a sharp rise is observed in the output signal. The capillary pressure and hence the voltage increase as water travels through the GDL. When the water breaks through the GDL surface a sudden drop is observed in the voltage output. This drop indicates the breakthrough phenomenon. The sensor is calibrated using a manometer, assembled in an arrangement where the height is gradually increased to apply more pressure on the sensor while the voltage response is recorded. The calibration curve is shown below. This curve is used to obtain the capillary and breakthrough pressure for different GDLs.

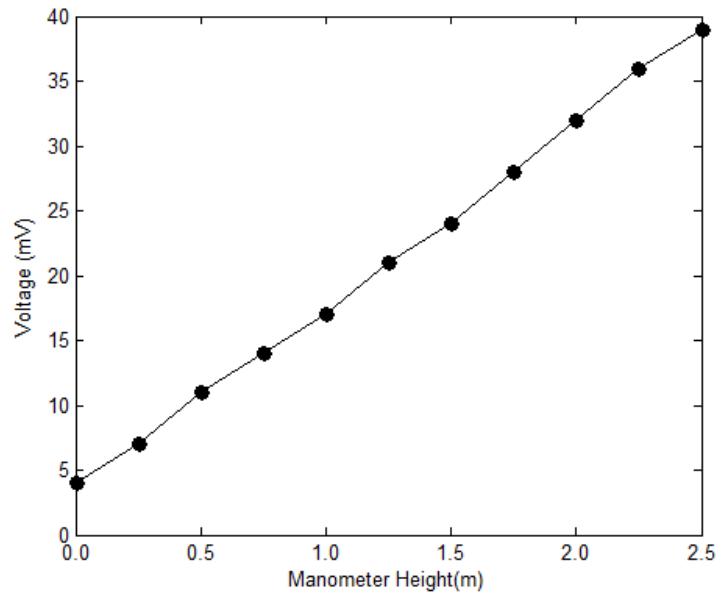


Figure 2-4: Pressure sensor calibration graph showing the change in voltage with the change in manometer height

2.1.3.2 Calibration for thickness

To calibrate the system for the distance between the last micro-needle and the GDL surface as well as the thickness of the PDMS layer, the setup is assembled in its usual way but the GDL is replaced by another voltage sensor. The time is measured between the signals received from the last micro-needle and the voltage sensor. This calibration process is conducted every time the PDMS layer is replaced.

2.1.3.3 Calibration for Expansion

When water touches the bottom surface of the GDL, a gradual rise in the pressure is observed. No sign of leakage has been observed due to this pressure. However, the setup includes flexible FEP tubing, expanding under this pressure. This expansion affects the

measurement of the time of breakthrough as well as the total water content in the GDL. To measure the volume caused by this expansion, a calibration process is conducted where a tube of the same length and material is connected to a pressure sensor from one end and a Hamilton glass syringe from the other end. The tube and syringe are filled with water. Extra care is taken to remove bubbles from the systems. When the tube is filled to its capacity, it mimics the situation where water just touches the bottom surface of the GDL and no pressure is applied. As water is injected at a controlled flow rate, the pressure (recorded by the pressure sensor) increases gradually at a constant rate. This increase in the pressure depends on the volume of the water injected. Therefore, the expansion volume is the amount of the volume injected to increase the pressure to a certain limit. Figure 2-5 presents the calibration curve showing the expansion volume as a function of the pressure.

In the actual experiment, the maximum pressure is recorded at the breakthrough condition during which the maximum expansion occurs in the system. This volume of expansion can be obtained by measuring the breakthrough pressure and using the calibration curve presented in Figure 2-5. The time associated with tubing expansion can be obtained from the flow rate of the syringe pump and the expansion volume obtained from Figure 2-5.

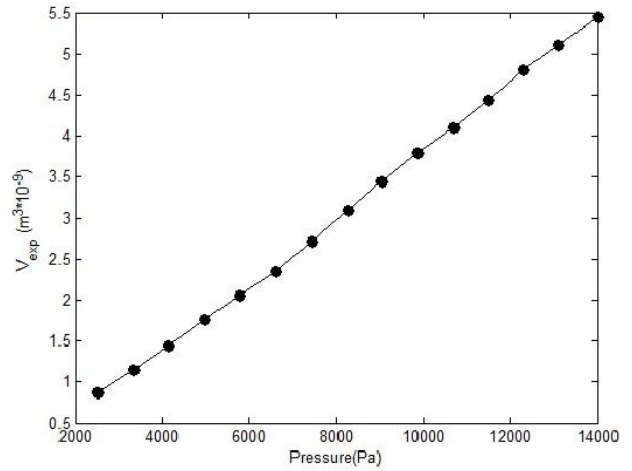
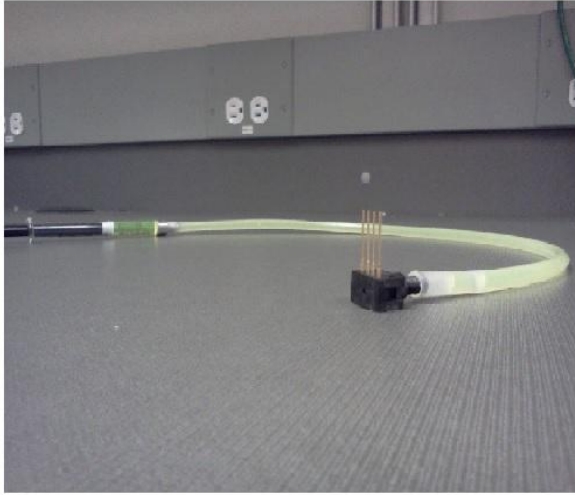


Figure 2-5: Calibration procedure adopted to measure the expansion of tubing (left); the result of the calibration experiment (right)

Finally, the corrected time of breakthrough ($t_{breakthrough}$) is calculated based on the actual measured time ($t_{measured}$), recorded between the signal of the last micro-needle and the breakthrough of the droplet, and the calibration times, correcting the effects of the thickness ($t_{thickness}$) and expansion ($t_{expansion}$) in the setup (see the equation below).

$$t_{breakthrough} = t_{measured} - t_{thickness} - t_{expansion} \quad (2.2)$$

2.1.4 Experimental Procedure

A circular GDL sample with the diameter of 22mm is placed on the surface of the injection channel. Only an area with the diameter of 3mm is exposed to the channel. As mentioned earlier, the GDL has to be kept under pressure to avoid leakage. Thus, sufficient pressure is applied using a PTFE cylinder placed on top of the GDL. A through hole with the diameter of 7mm was drilled in the center of the PTFE cylinder. This hole provides a viewing area for the camera capturing top-view images. The hole was intentionally selected larger than the diameter of the

injection channel to avoid changing the morphology (hydrophobicity) of the area under study due to compression [58]. For instance, if the pressure cylinder is designed with the same diameter as the injection channel, there is a large possibility that breakthrough occurs along the wall of the cylinder where the GDL is less hydrophobic compared to the areas in the middle that are not compressed. Thus, the diameter of the viewing area was selected twice as large as the injection channels so that when water comes into contact with the GDL at the tip of the injection channel, it is exposed to areas with less variation in terms of hydrophobicity. A cap (threaded from inside) is used to ensure the sample is compressed by the cylinder. The cap is turned to a certain point that is marked in the thread to achieve uniform compression for all the experiment (see Figure 2-6).



Figure 2-6: First generation assembly: the platform for GDL (left), the pressure cylinder (middle), the cap used to exert pressure on the pressure cylinder (right).

The camera is adjusted to the right focus and zooming arrangements in the image acquisition mode. Images were acquired at the rate of 25 frames per second. DC power is supplied to the pressure sensor. The only operational variable that is involved with this ex-situ testing is the flow rate at which the water is injected. The flow rate needs to be selected appropriately to mimic the

water production rate occurring in the course of flooding. This flow rate can be calculated using Faraday's law [97]

$$m = \frac{Q * M}{F * z} \quad (2.3)$$

where, m is the mass of the substance produced, M is the molecular mass of that substance, Q is the total charge transferred, F is Faraday's number (96500 C/mol), z is the electron transferred per ion. The derivative of the above equation with respect to time will result in the calculation of the flow rate of the water produced at a certain current, i (A).

$$\frac{dV}{dt} = \frac{i * M}{z * F * \rho} \quad (2.4)$$

In this equation, ρ presents the density of the substance. Considering the current density of 1.7A/cm² (representing the flooding condition) and the area of 0.07 cm² (corresponding to the diameter of 3 mm), the water flow rate obtained from the above equation will be 1.11×10⁻¹¹ m³/s (i.e., approximately 40μL/hr) which corresponds to a Reynolds number of less than 1. In this thesis, measurements were conducted for two flow rates (40μL/hr and 400μL/hr) to demonstrate the effect of the flow rate on the breakthrough time and pressure (see Chapter 4).

A variety of GDL samples with different thicknesses and PTFE loadings are used to measure the breakthrough time and pressure. The samples selected for this part of the analysis do not include micro-porous layers (MPL) (unlike those studied for diffusivity in Chapter 3). These samples (tested with both first and second generation setups) include Toray TGP060 (190μm) with 0%, 6% 19%, and 40% PTFE loadings, TGP090 (280μm) with 0% and 40% PTFE

loadings, AvCarb P50 with 13% (164 μm) and 33% (161 μm), and two E-lat carbon cloth samples with the thicknesses of 270 μm and 380 μm .

Experimental measurements are always associated with certain levels of uncertainty due to the changes in the operating conditions, errors associated with the measuring instruments and external factors. For the water transport measurements described above, the minor changes in temperature or humidity are not expected to influence the results. The experiments were performed by the same individual following the same procedure every time. Therefore, external factors can also be ignored. However, the experiments were conducted using a pressure sensor with a non-linear error of maximum 0.5% within the operational range. In addition, the time of breakthrough measurement is performed visually. In essence, a stopwatch is started when the top needle displays voltage signal and stopped when the droplet appears in the top view. There could be time delays due to the response time of the operator and the instrument. This response time is around 2-3 seconds which is less than 1% of the minimum time of breakthrough measured for both the first (500sec) and second (320 sec) generation setups. Therefore, the total error percentage is less than 2% out of which the pressure sensor can contribute a maximum error of 0.5%, and the time of breakthrough can cause a maximum error of 1%.

2.1.5 Limitations of First Generation Setup

The first generation setup provides a platform for gaining insights into the flow characteristics of water through the GDL. The setup has been used to study different regimes of flow (including invasion, progression, and pore-filling patterns) through visualization of liquid water pathways in the GDL [97]. Also, the setup provides a quantitative measure of the pressure and time required for water to penetrate and breaks through the GDL. Despite the general

success of this setup, it has two main problems influencing the accuracy of the results obtained (see Chapter 4):

- The pressure sensor used has a lower range than the breakthrough pressure observed for most samples: for hydrophobic samples, the breakthrough pressure measured lies in the range that is outside the range of the pressure sensor (which is 0 to 5000 Pa). This high pressure can cause damage to the membrane of the pressure sensor, affecting the results reported from the sensor.
- The typical breakthrough pressure measured for the GDL is within the range of 5000 to 12000 Pa for which the impact of expansion is not negligible as the liquid volume inside the tubing increases linearly by the pressure (see Figure 2-5). In addition, the calibration results can be dubious as highlighted in Chapter 4. Therefore, the use of flexible tubing should be avoided to eliminate any errors associated with expansion. Instead, the setup should be made of solid materials so the problem of expansion can be fixed entirely instead of measuring flexibility and correcting the results.

2.2 Experimental Setup (Second Generation)

The second generation setup uses the same principle (as the first generation) for the measurement of the breakthrough time and pressure. In essence, all the components and parameters in the second generation are kept the same as those in the first generation except for tubing which was eliminated in the second generation setup. The breakthrough time is measured based on the signal received from the last voltage sensor and the first sight of the droplet evolution. This time is corrected to compensate for the distance between the GDL and the last voltage sensor. A similar pressure sensor (RPO250G6H from Sensortechncs) used in the first

generation was implemented in the second generation; however, the new sensor can measure up to 25000 Pa (as opposed to the pressure sensor used in the first generation setup that can measure up to 5000 Pa). This is at the high range of the breakthrough pressure measured for typical GDLs with large PTFE loadings. The pressure sensor used for the second generation is installed and face sealed against the water injection channel. Similar to the first generation setup, the sensor is calibrated using a manometer for its entire range. As a result, the capillary pressure can be obtained from the sensor output and the calibration curve. Figure 2-7 presents a typical response received from the pressure sensor. Before water touching the GDL, the pressure and hence the voltage is negligible. The voltage output will linearly increase over time as water penetrates through the GDL. Thus, this curve can also identify the moment that water touches the GDL. The pressure increases till the first water droplet breaks through the top surface of the GDL. At this moment, the voltage will drop rapidly. The maximum voltage in this curve corresponds to the breakthrough condition. Thus, this curve can also identify the time of breakthrough when the pressure drops to the atmospheric pressure.

Another problem found in the first generation setup is the expansion of the flexible tubing. The best solution to the expansion problem is to make the entire setup out of a rigid material which has a relatively small expansion coefficient. The initial choice was acrylic material. Its transparency facilitated the detection of the presence of bubbles as well as tracking water as it touched the bottom surface of the GDL. However, the setup did not last long as the choice of the material was not ideal for two reasons: 1) the GDL needed to be pressurized but acrylic was brittle in nature. Thus, the system broke when excess pressure was applied; and 2) the PDMS layer used to avoid leakage (see Section 2.1.2) needed to be sometimes heat-treated to speed up the curing process. However, acrylic has a high coefficient of expansion that resulted in the

change in physical dimensions of the setup when it was exposed to heat. Therefore, the setup was remade using Teflon. Figure 2-8 shows the second generation assembly. The syringe is connected (through a threaded hole) directly to the Teflon block to eliminate tubing. The end of the glass syringe is face sealed against an opening that has the same diameter as the opening of the tip of the syringe pump. Face sealing is conducted to prevent leakage. The tip of the Hamilton syringe is wrapped with the Teflon tape.

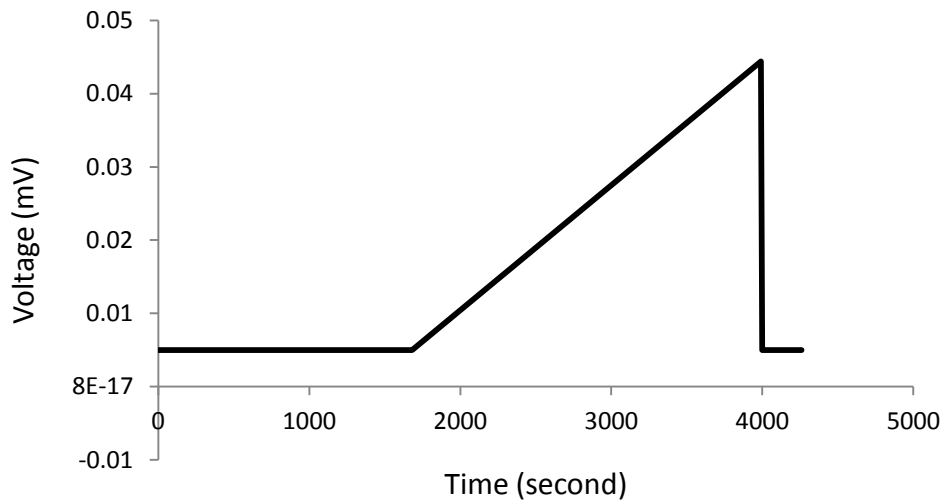


Figure 2-7: A typical response curve of the pressure sensor which displays its output in terms of voltage

Another modification to the first generation is the introduction of an additional camera to capture the side view images of the droplet growth. For this purpose, a hole is drilled in one side of the actual setup to create a viewing window for the camera (see Figures 2-8 and 2-9). The challenging part, however, is to drill a hole in the pressure cylinder. The event of breakthrough depends on the uniform pressure applied by the pressure cylinder across the sample. If the entire cross-section of the pressure cylinder is not in contact with the GDL surface there will be a possibility for leakage through the area that is not in contact. To avoid this problem, the hole in

the pressure cylinder is slanted slightly downward (at a very small angle), so the thickness gradually decreases to zero as the opening approaches the GDL. Instead of creating a through hole, a hole with a downward slope maximizes the contact area of the cylinder with the GDL. The camera is then positioned in a way that the entire profile of the droplet can be visible. The comparison between the top and side-view images results in identifying the time of breakthrough more accurately. Also, for future studies, this modification will facilitate the measurement of dynamic contact angles as the droplet grows on the surface of the GDL. This contact angle measurement can provide useful information regarding the surface properties of the GDL, but it is outside the scope of this research.

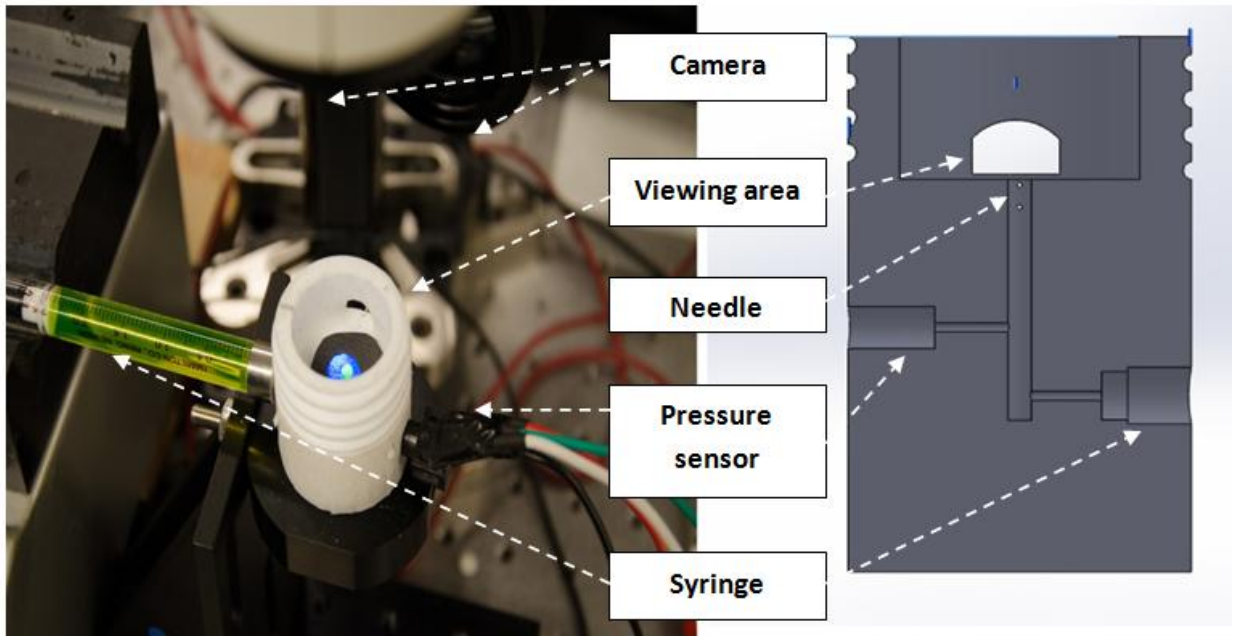


Figure 2-8: Schematic of the second generation assembly

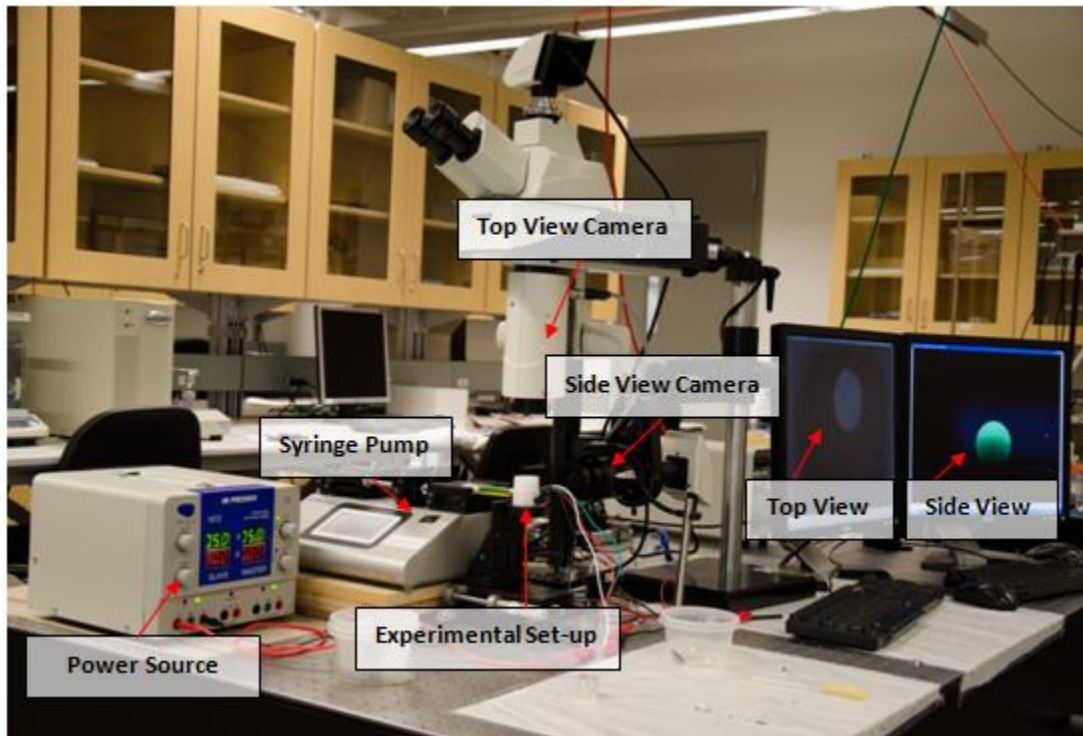


Figure 2-9: The second generation of the experimental setup developed for the measurement of the water content in the GDL

CHAPTER 3: EXPERIMENTAL SETUP FOR MEASUREMENT OF EFFECTIVE DIFFUSION COEFFICIENT IN GAS DIFFUSION LAYER (GDL)

An experimental setup is developed for the measurement of the effective diffusion coefficient of different GDL samples. Only samples with micro-porous layers (MPL) were used for the measurement of the effective diffusion coefficient. Hence, in this chapter the term GDL refers to samples with micro-porous layers. The novelty of this setup (compared to those discussed in the literature review section of Chapter 1) lies in the fact that it is capable of estimating the changes in diffusivity when the sample becomes wet from dry. As mentioned in Chapter 1, the measurement of diffusivity in samples containing water is crucial as it resembles the real conditions occurring in the fuel cell.

This chapter discusses the design and fabrication of the experimental setup with the constraints associated with different components. The setup can be used to study the effect of different operating parameters like temperature, humidity, flow rate, pressure gradient, and compression level across the two sides of the GDL. However, the response of the system to the change in the above parameters was not the focus of this research. The objective of this research is to study the effect of the GDL properties on the diffusion coefficient.

The first part of the chapter (Section 3.1) consists of the principle adopted for the measurement of the diffusion coefficient. The schematic of the experimental setup along with the different design constraints will be discussed in Section 3.2. The diffusion assembly which consists of the flow plate and fabrication of the GDLs will be presented in Section 3.3. The control of different operational parameters (particularly the differential pressure), which involves

the use of a number of peripheral devices, will be discussed in Section 3.4. The water injection method to make the GDL wet will be discussed in Section 3.5. The experimental procedure adopted for the dry measurement will be presented in Section 3.6. Finally, the model developed to interpret the data will be presented in Section 3.7.

3.1 Principle of Measurement

Diffusion will proceed only when there is a concentration difference between chemical species that exist within a close proximity to one another. The concentration gradient is the driving force for mass diffusion, similar to the effect of the temperature difference on heat transfer. A typical example of diffusion is dispersion of different oxides emitted from automobiles into the environment. However, the flow of air actuated by a fan is not considered as diffusion.

The physical origin of diffusion stems from Brownian motion which is the random motion of gaseous molecules. The term concentration is defined as the number of moles per unit volume. Thus, a gas which has a larger number of moles per unit volume is considered to have a larger concentration with respect to another gas having a smaller number of moles per unit volume. When two gases are mixed together or they come into contact with each other there is an equal probability that one might diffuse into the other due to their Brownian motion. However, a gas having a larger number of molecules per unit volume has a higher chance to diffuse in the other gas, as it has more molecules undergoing the Brownian/random motion. This phenomenon is illustrated in Figure 3-1. Two gases A and B are mixed together to form a binary mixture. When the separator between them is removed, the gas A will diffuse in B as it has a higher concentration.

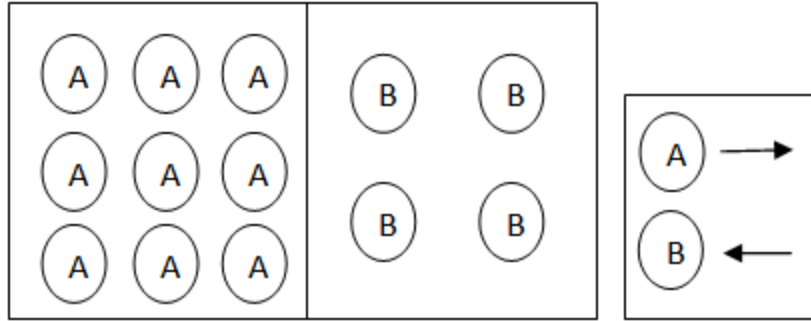


Figure 3-1: Mass transfer by diffusion in a binary mixture

To study diffusion through a porous media like the GDL, the usual practice is to produce a concentration gradient by flowing two different streams of gases across the two sides of the sample. Methods proposed for studying diffusion have been reviewed in detailed in [98-99]. A more recent development, related to this thesis, is the work of Pant et al. [100] who used the diffusion bridge technique to estimate diffusion in dry GDLs with MPLs. One of the advantages of the diffusion bridge technique is the ability to control accurately the pressure gradient across the two sides of the GDL. The work of Pant et al. [69] takes into account both modes of diffusion and convection mass transfer. However, for the setup developed in this research, the pressure gradient is effectively controlled to limit the transport mechanism to solely diffusion while restricting convection. The effective control of the pressure gradient essentially means that the pressure difference is kept at zero or very close to zero to minimize the effect of convection occurring due to bulk fluid motion. Therefore, the diffusivity values reported in this thesis are pure diffusion which is the main mode of transport especially for GDLs with low permeability values [65].

Figure 3-2 presents the overall schematic of the setup. In essence, two independent streams carrying different gases (air on top and nitrogen at the bottom of the GDL) flow horizontally

while the porous GDL is positioned in the middle. The setup is in the form of a parallel flow mass exchanger, causing the diffusion of oxygen species into the nitrogen channel as a result of the concentration difference. This mass flow exchanger also mimics the conditions of the cathode of the fuel cell, considering the nitrogen side as a catalyst layer. The driving force behind this transfer will only be the concentration gradient if the pressure difference across the plates can be reduced to near zero. Both the output streams are analyzed using a gas chromatograph to find the composition of each stream. This analysis of the output stream provides a quantitative measure of the amount of crossover. The device is also kept horizontal to eliminate the effect of gravity which might induce bulk flow.

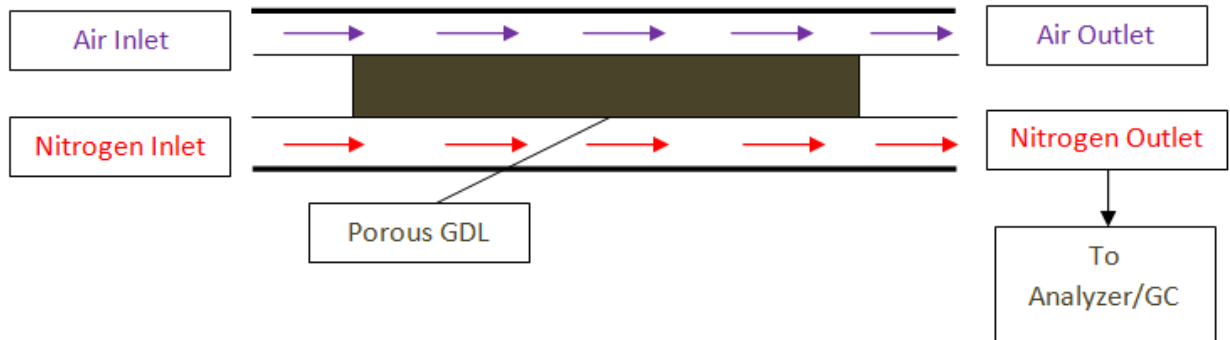


Figure 3-2: Schematic of the flow stream in the diffusion assembly based on the diffusion bridge technique [100]

In addition to the measurement of the effective diffusion coefficient, the setup can also be used to measure permeability of the GDLs (similar to [92]). Convection can be induced by altering the pressure gradient and calculating the transport coefficient for the corresponding pressure gradient value.

3.2 Schematic of Experimental Setup

The measurement of diffusivity is a difficult task since it is extremely sensitive to the pressure gradient. Even a very small pressure gradient will induce components of bulk flow, and hence transport becomes dominated by convection. Thus, the focus of this setup is to minimize the extent of convection by controlling and monitoring the pressure difference across the two sides of GDL on a continuous basis.

In the proposed setup, the diffusion coefficient is measured in one direction (along the thickness of the samples) and it is expected to follow Fick's law (similar to the studies in the past [69,78]). The nitrogen-air gas pair is used. In addition to the measurement of pure diffusion, the setup is capable of measuring the change in diffusivity when the water saturation level inside the GDL increases. This represents the real problem associated with diffusion in a typical fuel-cell running at a higher current density.

The details of the experimental setup are shown in Figure 3-3. The setup consists of five main parts including the diffusion assembly, the gas supply, the humidifier, the back pressure regulator, and the gas chromatograph (GC). The setup was developed in collaboration with Ballard Power Systems Inc., and hence it is built around the standard Ballard test station which was tailored to meet the design requirements for the diffusivity measurement. The typical gas supply unit of the Ballard test station is used to supply nitrogen and air to the two sides of the GDL. The diffusivity is first measured through a dry GDL sample. Then, the GDL is saturated using a water injection mechanism to estimate the change in diffusivity as the sample becomes wet. To keep the saturation level unchanged during the measurement of diffusivity in the wet sample, a membrane humidifier is used to supply humidified gases to the setup. The gas supply

units are connected to the differential pressure sensors used to measure the pressure difference across the two sides of GDL. The gases are then fed into the diffusion assembly. The outlets of the diffusion assembly are connected to the back pressure assembly to control and regulate the pressure difference. The outlet streams are then analyzed for the composition of each gas. For a multi-component mixture, a gas chromatograph (GC) is an ideal option since it can separate different constituents and provide the fractional composition of each component. A relatively inexpensive, but less accurate, option is a gas sensor which works based on thermal conductivity. In this research, the nitrogen channel is analyzed in the gas chromatograph (GC) to measure accurately the amount of oxygen crossover, which is also verified by analyzing the outlet of the air channel in a gas analyzer. A number of valves are used for precise control of pressure. Water knock-off is placed along different points in the circuit to prevent water accessing the pressure sensor and the GC. The components used in the setup will be elaborated in the following sections.

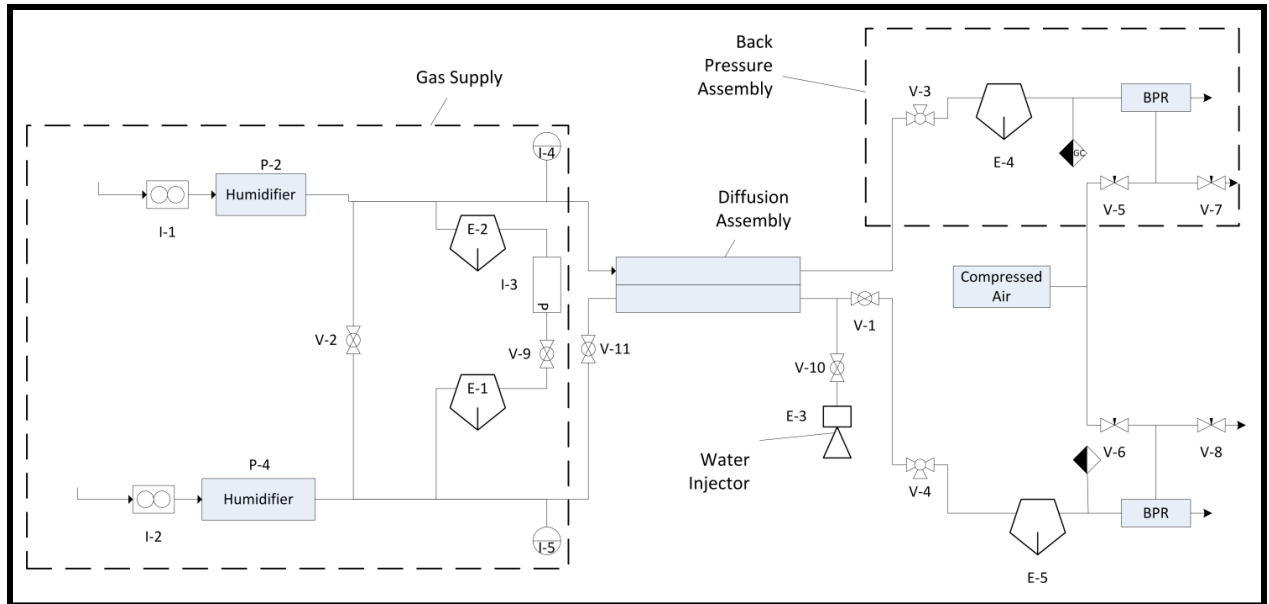


Figure 3-3: Schematic of the diffusivity setup and its main components: I-1 and I-2 are the two flow-meters; V-1, V-2, V-3, V-4, V-9, V-10 and V-11 are quarter turn needle valves; V-5, V-6, V-7 and V-8 are metering valves; E-1, E-2, E-3, E-4 and E-5 are water knockouts; I-3 is the differential pressure sensor, I-4 and I-5 are the pressure sensors measuring the pressure difference between the inlets and outlets; GC is the gas chromatograph; and BPR is the back pressure assembly

3.3 Diffusion Assembly

The diffusion assembly is the most important component of the experimental setup. The schematic of this assembly is shown in Figure 3-2. The parallel channels positioned along the two sides of the porous media are made out of acrylic for better visualization which facilitates the detection of the presence of bubbles inside the flow channels and water breakthrough at the surface of the GDL, and the study of the overall behavior of liquid water for the wet diffusivity measurement. Acrylic also provides thermal isolation of the GDL and the diffusion assembly from the test station and compression hardware. Machining is another feature that supports the selection of acrylic over other possible alternatives (such as graphite). The flow plates were machined using a CNC machine at the machine shop facility of the School of Engineering, University of British Columbia.

The design of the flow plates is a challenge given that the control of pressure is directly related to the flow-field geometry. In order to avoid the effects caused by convection, serpentine flow field (widely used for enhancing mass transfer) is intentionally avoided. Thus, the flow plate geometry selected here is limited to straight parallel channels. To optimize the depth, width, length and the number of the channels, COMSOL Multiphysics (simulating the flow) was used. The preliminary design included a very large length to width aspect ratio for each channel to create one-dimensional flow. This resulted in the channel width of $200\ \mu\text{m}$, which is difficult to machine. In addition to manufacturing complexity, this design may not withstand the force of compression. In the second attempt, the number of the channels was reduced to five to utilize maximum flow channel area. This configuration resulted in 82% channel and 18% land areas for which the one-dimensional assumption of diffusion is still valid. With the revised geometry, however, it was very difficult to distribute evenly the flow between five different channels. Thus, for the final attempt, the flow-channel geometry was confined within a single-straight channel with the width of 8.4mm, depth of 2.5mm, and length of 90mm. The flow follows a cross pattern where it enters through the inlet port located in one end and exits from the outlet port located on the other end of the plate. A schematic of the flow plate used for the diffusion setup is shown in Figure 3-4.

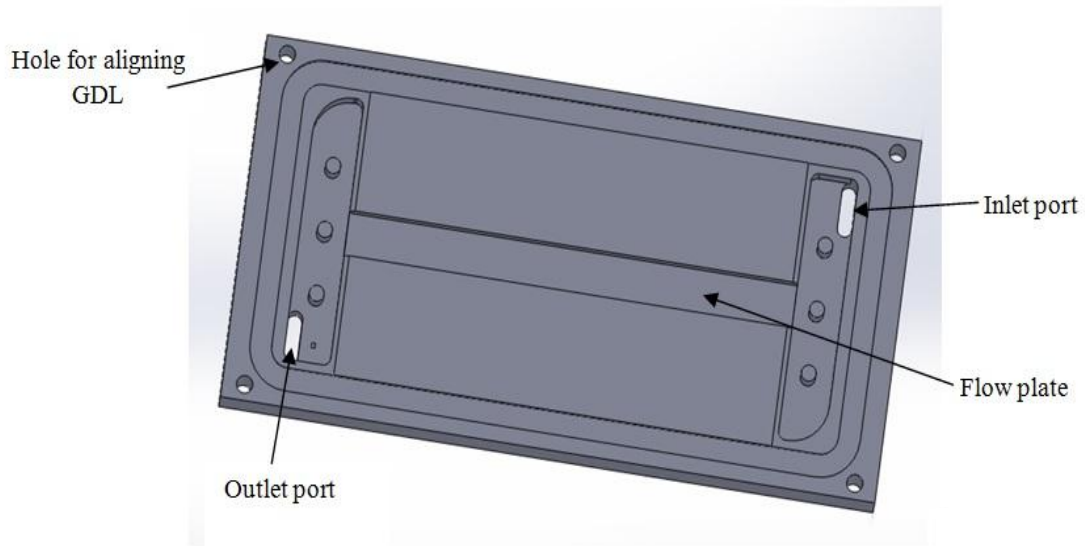


Figure 3-4: Flow plate design

Navier-Stokes equations were solved to simulate the flow in the above flow-plate geometry using COMSOL. Mesh independence was conducted, resulting in the mesh size resolution of 0.05mm along the width and the length and 0.06 mm along the height of the channel. Thus, the number of the meshes considered along the length, width, and height is 1800, 168 and 42, respectively. The result of the simulation is shown in Figure 3-5. It is shown that the channel velocity across the length remains almost constant after the initial zone, which is the entrance length. Once the flow becomes fully developed, the change in the velocity along the length of the plate is negligible. At each cross section, the velocity profile is parabolic.

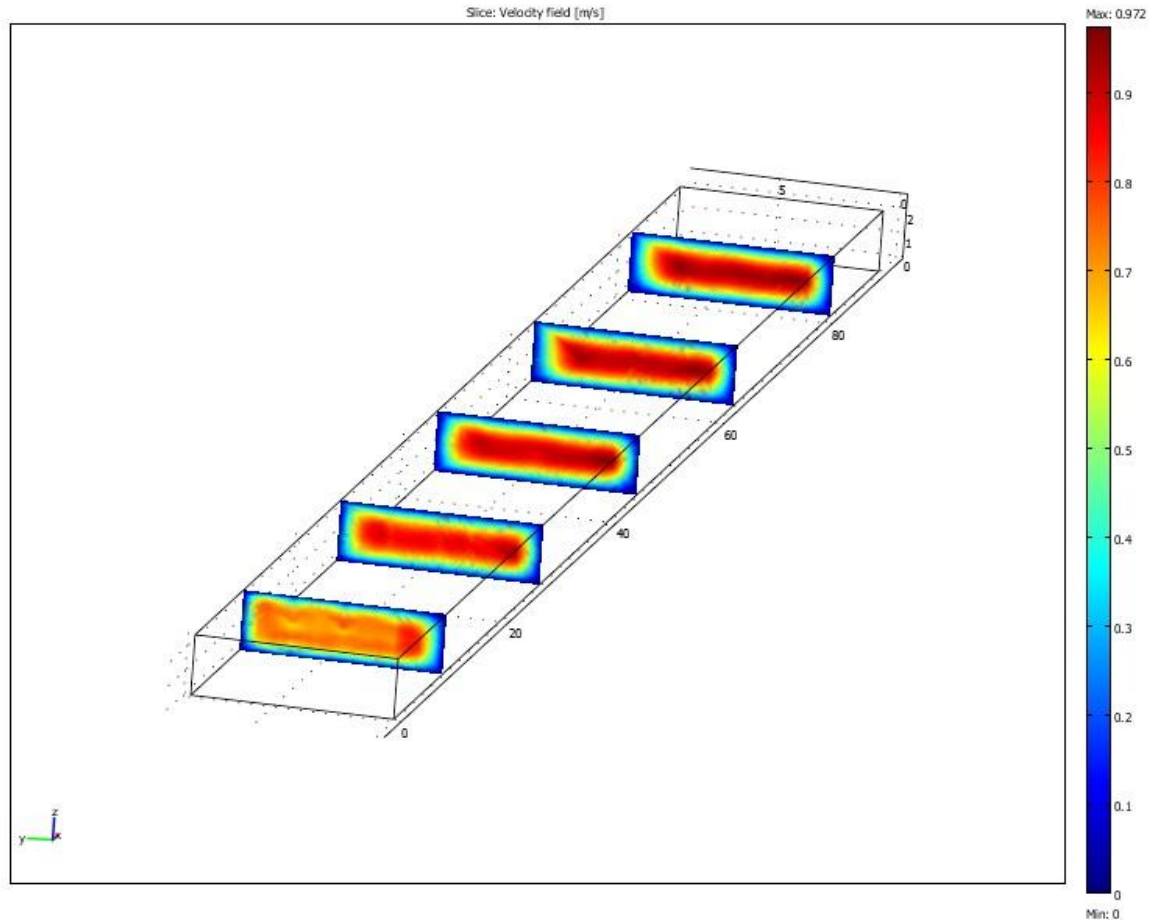


Figure 3-5: Velocity profiles at different cross sections of the flow plate (COMSOL results)

To determine the Reynolds number ($Re = \frac{V * D_H}{\nu}$, where V is fluid velocity, ν is viscosity of air, and D_H presents the hydraulic diameter), the flow rate of 1 SLPM, must be corrected for the experimental pressure of 19.7 psi (absolute pressure). Based on the relationship of $P_1 Q_1 = P_2 Q_2$, the corrected flow rate is 0.75 SLPM which results in the fluid velocity of 0.59 m/s. As a result, the Reynolds number for the above geometry is 145 presenting a laminar flow. The entrance length ($L_e = 0.06 Re D_H$) for this flow is 33.5 mm.

The result of the simulation was also plotted in Matlab to show the flow patterns in both lateral and the transverse directions (see Figure 3-6). The change in the velocity profile is also

negligible along the length of the flow plate when the flow is fully developed.

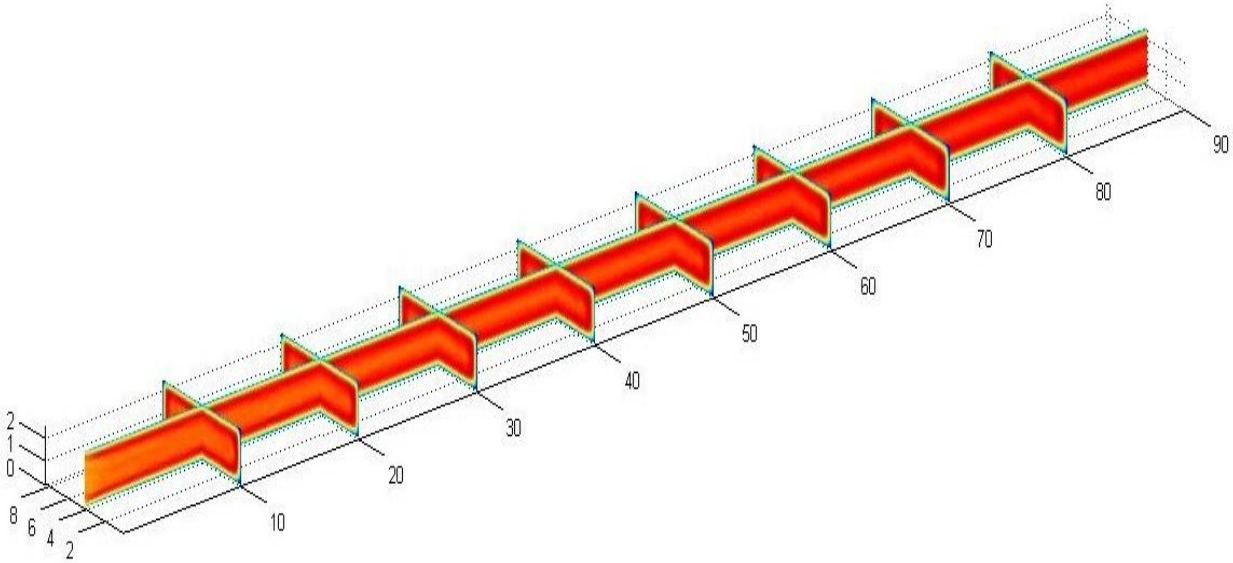


Figure 3-6: Flow patterns in both lateral and the transverse directions (obtained by plotting the results of COMSOL in Matlab)

The GDL is assembled using Kapton sheets facilitating the alignment of the GDL with the flow plates through alignment holes. This minimizes the lateral movement of the sample when it is placed on the cell hardware. The procedure (adopted from the Ballard's MEA assembly process) involves two steps (shown in Figure 3-7). At the end, both sides of the GDL except the area exposed to the flow plate are covered by the Kapton sheets. This results in restricting mass transport in other areas of the GDL except for the exposed area right in the middle.

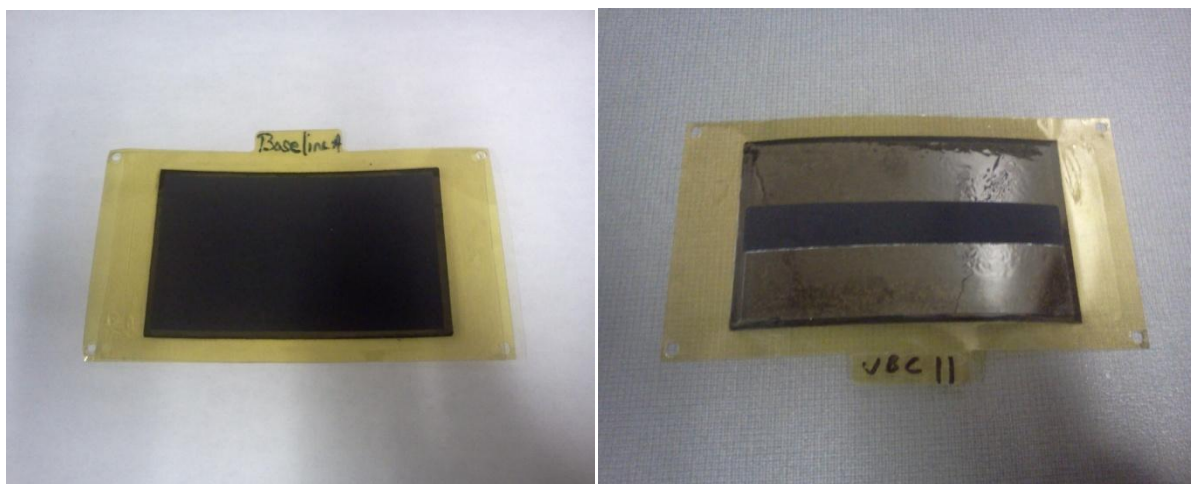


Figure 3-7: GDL assembly with the Kapton sheet: Step 1 (left) during which one side of the GDL is covered, and Step 2 (right) during which both sides of the sample except the area exposed to the flow plate is covered by the Kapton sheets

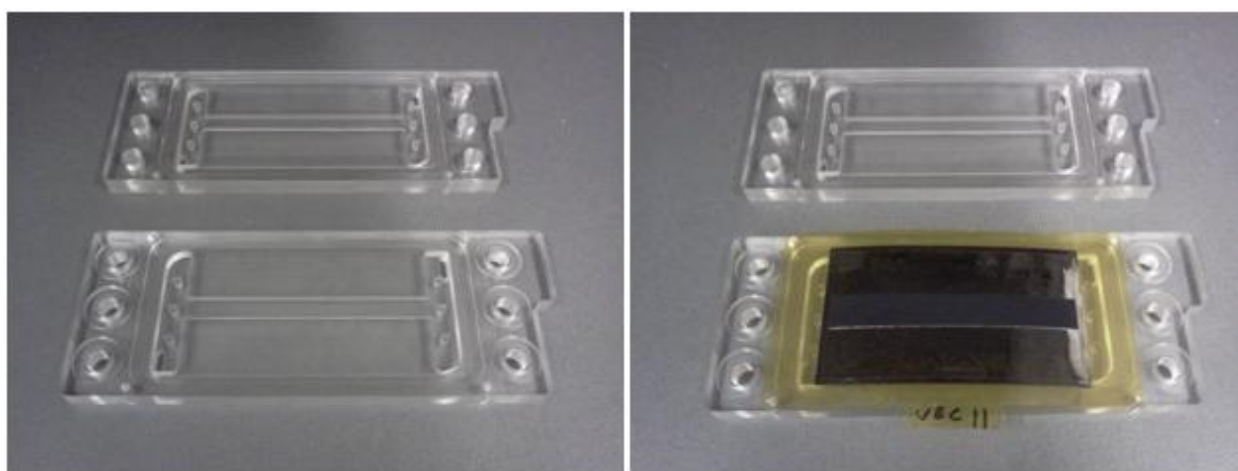


Figure 3-8: Flow plate and GDL assembly

Figure 3-8 shows the flow plates and GDL assembly. O-rings, placed in the six circular grooves on the two sides of the flow plate, were used to achieve proper sealing. A rubber gasket is used around the flow path region. To enhance the adhesion of the O-rings and the gasket to the flow plate, water is sprayed on all the grooves before putting the O-rings and gaskets. This is crucial since one of the plates is turned upside down during assembly.

3.4 Peripheral Devices

The measurement of diffusivity is susceptible to a number of different operating parameters including humidity, temperature, flow rate, pressure, compression, purity of gases supplied etc. Thus, it is important to measure diffusivity in a controlled environment. For this purpose, peripheral devices, elaborated in the following sections, were implemented.

3.4.1 Gas Supply

The gas supply provides different gases to the flow plate to create an artificial concentration gradient. As discussed earlier, air and nitrogen are fed through the top and bottom channels, respectively. An exploded view of the gas supply module is shown in Figure 3-9. The gas supply is connected to a mass flow meter. The flow meter is used to measure the mass flow rate of the fluid passing through the tubing. It is important to measure the mass flow as excessive mass flow reduces the accuracy of the results of gas chromatograph (or the gas sensor) in detection of small amounts of oxygen crossover. On the other hand, if the mass flow rate is kept at the low end a depletion layer is formed at the interface of porous media and flowing fluid. The mass flow meter is used in combination with a small orifice and a pressure reducing regulator. The use of orifice also assists the control of the flow rate along with the pressure reducing regulator.

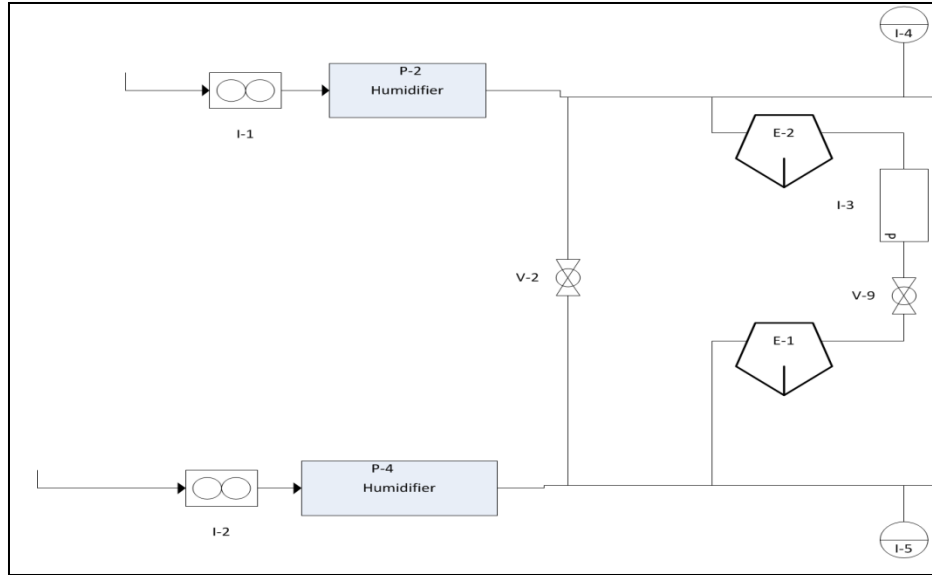


Figure 3-7: Gas supply module

A membrane humidifier is used to humidify the gas stream as it passes over an evaporating liquid stream. The level of humidification can be controlled by altering the operating parameters to meet the humidification demand. The humidity level is kept at 100% throughout the experiments. The gases upon exit from the humidifier are connected to a shunt valve, V-2, which provides a mechanism to control the pressure prior to the experiment. Right at the beginning of the experiment, the shunt is left open and the pressure is regulated until it falls within a reasonable range. After that the shunt is closed and the pressure is controlled using a differential pressure sensor, I-3. There is a possibility of crossover during the time the shunt is left open. However, this is not expected to influence the results as the shunt is closed right after the pressure is regulated. Even after that, a large amount of gas is fed through the channels for a reasonable time to make sure that there is no crossover through any other parts than the GDL.

3.4.2 Differential Pressure Sensor

As it was mentioned before, a small differential pressure across the GDL can induce convection and affect the measurement of diffusivity if pure diffusion is of interest. Furthermore, the wet diffusivity measurement is influenced by the presence of any pressure difference. A moderate pressure difference can act as the driving force for water removal which will change the saturation level of the sample during the measurement. Therefore, it is essential to use a very accurate pressure measurement device to measure the differential pressure with maximum precision. The sensor chosen for this purpose is the Sensirion ASP 1400 Differential Pressure Sensor providing accuracy and resolution particularly for very low differential pressure cases. The working principle of this sensor is based on the thermal gradient that is caused due to even small variations in mass flow rates. As specified by the manufacturer, the sensor has a sensitivity of 0.002Pa which corresponds to an altitude difference of 0.16mm [101].

For this experiment, the goal is to minimize the pressure difference across the GDL to a value close to zero. It is very challenging and almost impossible (from an experimental perspective) to attain an absolute zero pressure difference between the channels. Thus, the measurements are taken when the differential pressure between the channels falls within the range of ± 1 Pa. This difference is obtained with the aid of an optimum flow-plate design, accurate mass flow meters, needle valves and the back pressure assembly. The mass flow meters are used to control the flow rate to optimize the entry pressure. The needle valves at the outlet are used to regulate the exit pressure. The back pressure assembly provides a control of the back pressure.

The only drawback of the pressure sensor used is its susceptibility to the presence of water. The sensor still remains functional under the influence of humid air; however, it loses its functionality when it is exposed to water. For the wet diffusivity measurements, water is injected into the nitrogen channel during which water may come in contact with the pressure sensor placed at one end of the tubing used for water injection. Thus, water knock-outs (E-1 and E-2) are used and connected in series with the sensor, preventing water accessing the sensor. The two flow streams needs to be isolated when a steady pressure difference is obtained between the channels. This isolation is achieved by a valve, V-9, placed in series with the sensor. If the flows are not separated it may result in mixing and crossover, causing significant errors in the measurements.

3.4.3 Back Pressure Assembly

The back pressure assembly plays a significant role in the control of the differential pressure across the GDL. Typically, spring-type back pressure regulators are used for maintaining the required differential pressure. However, most spring-type regulators cannot provide the amount of precision required for this experiment. A precise membrane-type back pressure regulator, Equilibar EB1HF2, is chosen for this setup. Equilibar EB1HF2 can regulate wide ranges of pressure for wide ranges of flow media. It can also retain its performance for ultralow to zero flow situations with very little fluctuation. It has three ports: reference, inlet, and outlet ports. Both inlet and outlet streams are controlled by the single reference port. A diaphragm is connected to the reference port which controls the back pressure. The use of a friction-less membrane enables the opening at a relatively lower overpressure than that compressing the springs in the conventional back pressure regulators. The membrane also facilitates the use of the regulator for a wide range of flow rates at a low level of noise.

Figure 3- 10 shows the schematic of the back pressure regulator (BPR) assembly. Two water knock-outs are used before the gas enters the BPR assembly to block water existing in the flow stream entering the site of the BPR assembly and inducing unwanted noise. The water knock-outs also ensure that only dry air comes in contact with the gas chromatograph (GC) or the gas analyzer which are connected right after the water knock-outs. The reference port is equipped with two metering valves, V-5 and V-7, providing control of pressure.

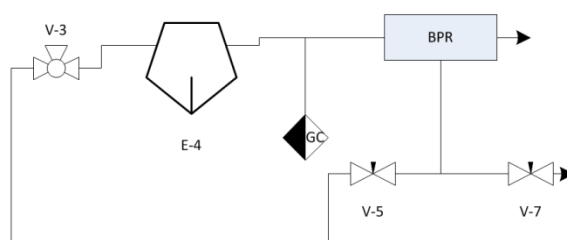


Figure 3-8: Exploded view of the back pressure regulator (BPR) assembly

3.4.4 Gas Chromatograph

Gas chromatography is a common technique used in analytical chemistry to separate and analyze different compounds due to its accuracy and quick response time. It is widely used for testing the purity of a substance or determining the relative amount of a component in a mixture [102]. It has also been used to trace a particular element in a mixture. A detailed overview of the chromatography technique is provided by Eiceman [102]. A gas chromatograph usually consists of a column typically made of glass or metal. The column is covered by a microscopic layer of liquid or polymer resting on an inert solid support. An inert gas like helium (or a gas with less activity like nitrogen) is kept inside the column and called the carrier gas. The compound that needs to be analyzed is carried along the column by the carrier gas. Along the path, the compound interacts with the wall of the column. Different components in the compound descend at different speeds and as a result elute at different time intervals (also referred to as the retention

time). The sample is then forwarded to a thermal conductivity detector which senses changes in the thermal conductivity. When a component elutes from the column the thermal conductivity of the effluent column reduces and a detectable signal is generated.

Before performing the experiments, the GC (HP M200) was calibrated for 0.5%, 1%, 2%, 5% and 10% oxygen, covering the range expected for oxygen crossover. The GC displays the output as a chromatograph plot shown in Figure 3-11. The two bumps indicate the presence of two different gases detected based on their different retention times. The large bump is associated with oxygen, and the area under this curve presents the amount of oxygen in the gas stream. The GC is equipped with an interface calculating the area under the curve and displays the output in terms of the oxygen percentage. In this study, the oxygen concentration in the channel was measured for every 70 seconds.

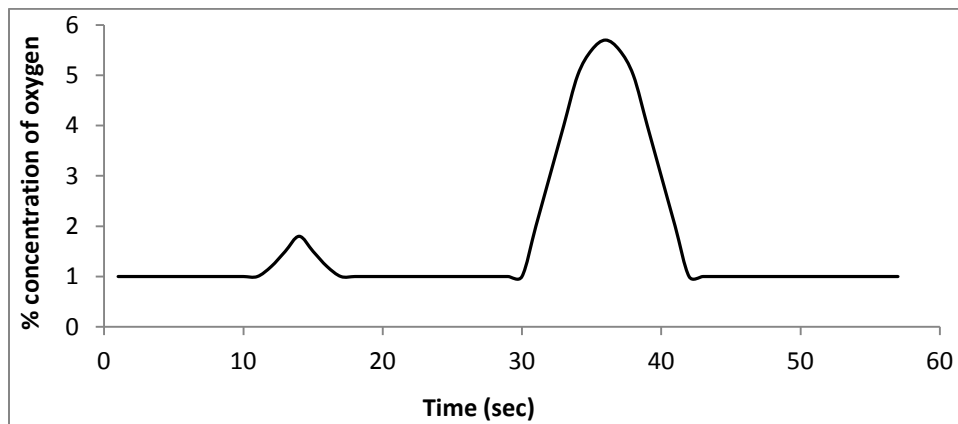


Figure 3-9: A typical plot of GC showing the change of concentration of oxygen with time

Gas chromatography technique (GC) is adopted to find the amount of oxygen crossover across the porous media due to diffusion. The output stream from the nitrogen channel is connected to the GC before it enters the back pressure assembly. The output stream of the air channel is also analyzed to measure the remaining oxygen content after the crossover. A gas

analyzer is used for this purpose. The air supplied contains 21% oxygen. For all the samples tested, the total oxygen amount measured using the GC and the gas analyzer is found to be 21%.

3.5 Water Injection

One of the novelties of the proposed diffusion measurement setup is the ability to measure the change in diffusivity due to the change in the saturation level of the GDL. For this purpose, a water injection module is designed to wet the GDL. Water is injected in the nitrogen channel, mimicking the catalyst layer of the fuel cell. The air channel resembles the cathode flow field where oxygen is supplied to the catalyst layer. First, the dry diffusivity is measured. Then, water is flushed into the nitrogen side of the GDL in two steps: water is injected only up to the point that it fills the tubing and the channel, and just touches the bottom surface of the GDL; and then, additional water is injected at a flow rate corresponding to the current density of 2 A/cm^2 .

The water injection system consists of three components: A syringe pump used to supply water at a desired flow rate, a 60-ml syringe connected to the diffusion assembly by Teflon tubing, and needle valves directing the water towards the GDL rather than any other components in the assembly. A schematic of the injection system is shown in Figure 3-12.

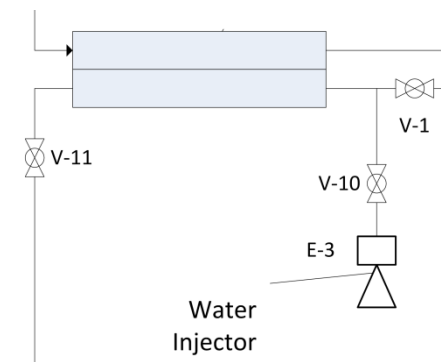


Figure 3-10: Water injection System

After measuring the dry diffusivity, the gas supply is turned off. The valve V-1 placed near the exit of the diffusion assembly is closed. The valve V-10 is fully opened. Then water is injected at a high flow rate (10mL/min) until it is visually observed at the end of the tube near the valve V-11 which is left open to ensure a smooth pathway for water throughout the nitrogen side of the diffusion assembly. This continuous flow of water is arranged to make sure that the GDL does not become wet when water is flowing at the high flow rate. For the GDL samples having micro-porous layers (MPLs), water must overcome a very large capillary pressure to penetrate and wet the sample. During continuous water injection process at the high flow rate, however, the pressure does not build up. The valve V-11 is closed when water reaches the valve and no bubble is observed in the piping. At that moment, the flow channel and the tubing are completely filled with water which just touches the bottom surface of the MPL side of the GDL. Any further injection of water will result in an increase in the pressure. At this stage, a fixed amount of 10 mL of water is injected at a rate of 100 μ L/min. As soon as the injection process starts, a rise in the pressure is noticed. The pressure increases linearly until the breakthrough event after which the pressure suddenly drops. However, the injection process is continued until the entire 10 mL of water is injected. Then, the valve V-10 is closed to isolate the diffusion assembly from the water injection module. After all the water is injected, the valve V-1 is opened very slowly and the gas is allowed to flow at a small flow rate which is gradually increased. The water from the channel is then drained through the water knock-out E-5. At this stage, extra care is taken to make sure that the water inside the GDL is not drained. The valve V-4 is added to obtain extra control over the drainage process. After draining all the water, the valves from V-11 to V-4 are left open.

It is desirable to quantify the saturation level in the GDL and find the change in the diffusivity as a function of saturation. Different approaches were studied. For instance, efforts were made to estimate the level of the GDL saturation from the change in conductivity. However, the conductivity measurements showed a very small change with high fluctuation. Also, the estimation of saturation based on the amount of water injected was not accurate due to two reasons: i) the effect of expansion of system components (e.g. tubing) as a result of the high pressure (close to 1MPa) was ignored; and ii) multiple breakthroughs were observed and it was impossible to account for the volume of the droplets removed from the surface of the GDL. Therefore, in this thesis, diffusivity is measured and compared only for two conditions: dry and wet.

3.6 Experimental Procedure

The experiments were conducted in two stages: first, diffusivity is measured for the dry sample, and then water is injected and the test is conducted for the wet GDL. Dry and wet diffusivity measurements are both conducted at the same operating conditions. The setup is well equipped to conduct experiments at different temperature, pressure, RH, gas compositions and flow rates, and flow rates of water injected. The diffusion assembly is equipped with manifolds that have provisions for thermocouples for the measurement of temperature. Pressure can be measured with the differential pressure sensor and also with the pressure sensor loaded in the Ballard test station. The flow rate can be measured and changed using the flow meter. The RH is controlled and regulated by the humidifier. Gases flowing along the channels can be changed to pure oxygen, helium, hydrogen, or carbon dioxide. The amount of water injected and its flow rate can be controlled via the syringe pump. Although, all of the above parameters can be

changed, they were kept constant for the sake of reducing the number of variables influencing diffusivity. Therefore, the only variable that is attributing to the changes in diffusivity is the composition of GDL samples. The operating parameters that are kept constant for both dry and wet measurements are listed below:

Table 3-1: Experimental operating conditions

Flow rate	1 SLMP
Relative Humidity	100%
Pressure	5 psig
Catalyst Gas Composition	100% N ₂
Flow Channel Gas Composition	Air (21% O ₂ , 79% N ₂)
Temperature	300K

The uncertainties in the diffusivity results can only be caused by the errors associated with the measuring instruments since the changes in the operating conditions were negligible and the tests were performed by the same operator. For instance, the back pressure regulator operates within a maximum error bound of 0.6% of its entire range (0.02-1000 psig) for the flow rate at which the experiments were conducted. The differential pressure sensor operates within an error range of 0.1% for the range of operation of 0.02-100 Pa. The error percentage of the GC is reported to be 3% of the actual measured value [100] which also includes the error in the time delay and the data interpretation interface.

3.6.1 Selection of Samples

GDL samples manufactured by AvCarb, Sigracet and Toray Industries are used for the measurement of diffusivity. Different samples are used to investigate the effects of hydrophobicity (presented in terms of the internal contact angle), thickness, pore diameter, and porosity on diffusivity. Since the study is focused on pure diffusion, only MPL samples are used for measurements. In essence, the fluctuation of differential pressure sensor across the two sides is considerably high for bare GDL samples (without MPLs). As a result, both modes of convection and diffusion mass transfer occur across the GDL. Thus, bare GDL samples are excluded from the diffusivity study.

Three different AvCarb-EP40 samples with different MPL coatings are tested. The properties of these samples in terms of the internal contact angle [19], mean pore diameter and permeability have been measured by Phillips et al. [103] (see Table 3-2). The goal is to study the relationship between diffusivity and these properties (see Chapter 4). Two different Sigracet samples (SGL 34BC and SGL 35BC) and a Toray (TGP-060-T19 with the MPL coating) are also tested to compare the results of dry diffusivity measurements with those reported in the literature [69,78]. The results of the wet and dry tests are also compared to study the changes in diffusivity for two different saturation levels. The porosity values for the SGL samples are taken from the manufacturer specification sheet. For all the other samples the porosity values are provided by Ballard. Other than the above mentioned commercially available samples, tests are also conducted for two proprietary GDL samples for which material properties are unknown.

Table 3-2: Properties of the GDL samples tested. The results shown in this table are obtained from [103].

Sample	Internal contact angle θ (degree)	Mean pore diameter D_{mean} (μm)	Permeability $k \times 10^{-14}$ (m^2)
AvCarb-EP40T12 CBT18 (low)	117.75 \pm 0.29	0.364 \pm 0.008	2.19 \pm 0.343
AvCarb-EP40T12 CBT30 (low)	118.14 \pm 0.29	0.306 \pm 0.010	4.01 \pm 0.014
AvCarb-EP40T12 CBT40 (high)	121.27 \pm 0.25	0.225 \pm 0.026	2.38 \pm 0.268
TGP060T19 CBT18 (low)	117.44 \pm 0.29	0.465 \pm 0.014	2.49 \pm 0.659

3.6.2 Testing Procedure

The diffusion assembly is first assembled together. In most diffusivity setups proposed in the past [91-92], several samples of the same GDL were stacked. However, this may cause an error in the measurements since the level of compression experienced by each GDL sample might be different. For the setup proposed in this research, a single GDL is used. The GDL is laminated between Kapton sheets and then sandwiched between the two flow plates. The grooves on the flow plates are sprayed with water before putting the O-rings in place. The flow plates are then put together. The compression hardware is installed next. An appropriate level of compression (60psi) is applied on the flow plates. Leak test is then conducted by blocking one side of the cell and pressurizing the system with a pressure higher than the operating pressure. For the initial leak test, a soap solution is used and the diffusion assembly is immersed in a water bath to identify the leak spots. If any major leakage is detected, then the assembly is reassembled. The degree of the leakage is then identified using the leak test facility at Ballard. The assembly is

used for the diffusivity measurement only after making sure that it is leak free. For every round of testing, the leak test is performed and the above steps are repeated.

The diffusion assembly is then connected to the test station and the associated components. The system is pressurized again and the soap solution is applied to all the fittings, valve connections and the system components to detect any leakage in the lines and other components. The soap solution forms bubbles in the places where there are leakages. These spots are then tightened even further or blocked using Teflon tapes.

For the dry tests, gases are supplied at the desired flow rate (see Table 3-1). The valve V-2 is left open at this stage until the differential pressure falls within a reasonable range. The valve V-2 is then closed and the gas is supplied for a period of time to make sure that the crossover gases have left the output stream. The pressure is then regulated using the back pressure regulator until a very low differential pressure (close to zero) is obtained. Then, the valve V-9, connecting the two sides of the differential pressure sensor, is closed in the next step to prevent any further crossover. The output stream is then connected to the GC input port. Gases flowing for the first 5 minutes after connecting to the GC are ignored as they might contain the ambient air or leftovers from the last run. The oxygen concentration in the nitrogen side is recorded for the next 30 minutes for an interval of 70 seconds. The differential pressure sensor valve is opened and differential pressure is checked every 5 minutes to make sure that it is till near zero. The runs in which the differential pressure exceeds 3Pa is excluded from the results. Each sample is tested at least twice with a minimum of 15 repeated measurements each time.

Once the dry diffusivity is measured, the valve V-1 is closed and V-10 is opened. The diffusion assembly is filled with water following the procedure described in the water injection

section. Any visible bubble is removed. After filling with water, the valve V-10, connecting the diffusion assembly to the syringe pump, is closed and the gas inlet and outlet valves (V-1 and V-11) are opened. Gases are then supplied across the two sides at the desired flow rate (1 SLPM). The gas flow purges the water from the channels and the tubing while some water still remains inside the GDL. This state represents the wet phase of the measurement mimicking the fuel cell condition running at high current densities. The differential pressure sensor valve (V-9) is kept closed and the shunt valve V-2 is opened until a reasonable differential pressure is obtained. The differential pressure valve is then opened. The shunt valve (V-2) is then closed in several steps during which the back pressure regulator is adjusted. The valve V-9 connected to the differential pressure sensor is closed and crossover amount is recorded 5 minutes after reaching the steady state. Similar to dry measurements, the differential pressure sensor is checked after every 5 minutes. The above procedure is shown in the following flowchart.

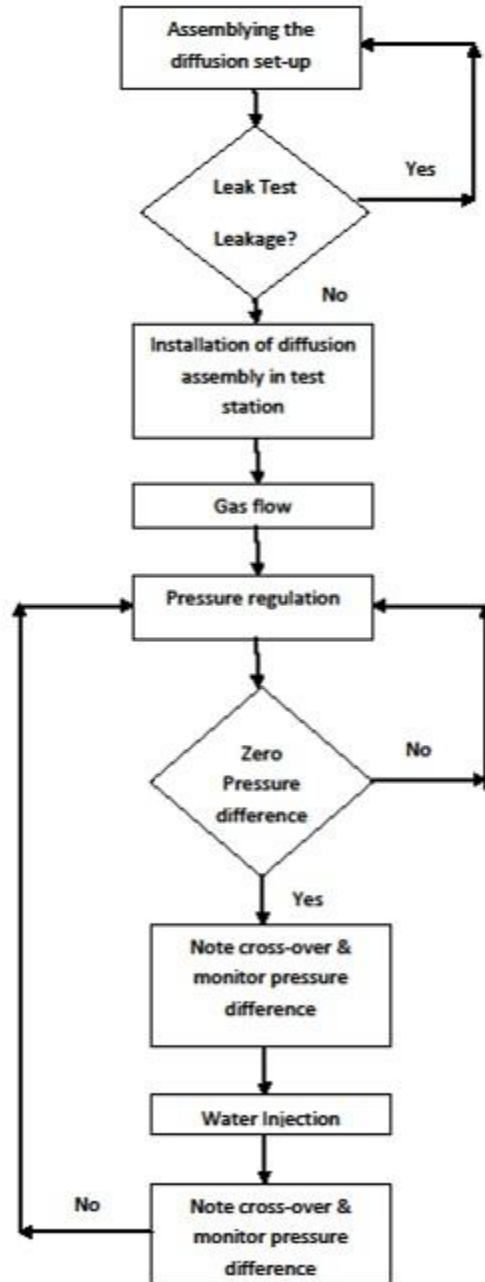


Figure 3-11: Flow chart of the experimental procedure for the diffusivity measurement

3.7 Numerical Analysis

The diffusion coefficient cannot be obtained directly from the experimental setup which only provides the amount of oxygen crossover. Thus, it is required to find a correlation between the crossover and diffusivity. For this purpose, an analytical model is developed to determine the effective diffusion coefficient of GDLs based on the crossover amount. It is assumed that the mass is transported only in the through-plane direction. Therefore, one-dimensional Fick's law (which considers only the molecule-molecule interactions) is adopted to extract the effective diffusivity of the GDL from

$$J = -D \frac{\partial \phi}{\partial l} \quad (3.1)$$

where, J is the diffusive flux, D is the diffusion coefficient of the medium, $\partial \phi$ is the difference in the concentration and ∂l is the diffusion length.

The Reynolds number calculated earlier ($Re = 145$) strongly suggests that the flow is laminar in the flow plate. Therefore, the assumption that the concentration remains constant across the channel will oversimplify the scenario and induce considerable errors. Also, the no-slip boundary condition assumed for the flow near the GDL boundary is not accurate due to the formation of a depletion layer near the boundary. This necessitates the development of a 3-D model finding the concentration in the flow channel based on the Fick's law of diffusion. Fick's law is accurate enough to describe mass transport as the pressure difference is very low and the mixture is not a multi-component mixture. However, Fick's law is not an appropriate choice if the mean pore size of the sample is very small (i.e., close to 10nm) [100]. For such a small pore size, the molecule-wall interaction becomes as significant as the molecule-molecule interactions. The diffusion

caused due to the molecule-wall interaction is called Knudsen diffusion which is not accounted for in the Fick's law. Knudsen diffusion is more likely to occur in the catalyst layer where the mean pore size is significantly smaller than that in the GDL [104]. For GDL samples, the mean pore sizes are in the range of 20 μm [104]. The mean pore sizes for samples with MPLs are reported to be in the range of 0.1 μm -1 μm [105-106]; while a considerably smaller pore size of 20nm has also been reported [104].

The Knudsen number, Kn, which is generally used as an index to characterize the flow regime (see Eq. (3.2)), is a dimensionless number calculated as the ratio of the mean free path, λ , of the gas in transport to the characteristic length of the medium, which depends on the geometry of the medium. The mean free path of air in the ambient condition is approximately 68nm [107]. For GDLs (with or without MPLs), the mean pore size, D_p , represents the characteristic length.

$$\text{Kn} = \frac{\lambda}{D_p} \quad (3.2)$$

For the AvCarb-EP40 samples used in this study, the Knudsen numbers are calculated based on the mean pore sizes reported in [103] (see Table 3-3).

Table 3-3: The Knudsen number for different GDLs

Sample	AvCarb EP40T12 CBT18 (low)	AvCarb EP40T12 CBT30 (low)	AvCarb EP40T12 CBT40 (high)	TGP060T19 CBT18 (low)
Mean Pore Size (μm)	0.19	0.306	0.225	0.465
Knudsen number(Kn)	0.364	0.22	0.30	0.15

The classification of the flow regime which depends on the Knudsen number is provided below [108]:

Table 3-4: Flow regimes based on the Knudsen number

$Kn < 0.001$	Continuum regime
$0.001 < Kn < 0.1$	Continuum-transition regime; slip condition is considered for Navier-Stokes
$0.1 < Kn < 10$	Transition regime; both Knudsen and molecular diffusion occurs
$Kn > 10$	Knudsen diffusion dominates

For bare GDLs, the mean pore size is in a micrometer range; while the mean free path is in a nanometer range. Therefore, the Knudsen number is very small and the flow is in the continuum regime. However, for the samples with MPLs, the Knudsen number lies within the entry zone of the transition region. Thus, there will be both molecular and Knudsen diffusion modes (particularly in smaller pores). There are a few established correlations describing the Knudsen effect within a porous medium like MPLs. These correlations either present the porous medium with an array of cylinders with different diameters, which does not truly reflect the structure of the GDL [109], or require information about the porosity and the thickness of the sample [22], which are not readily available. Pant et al. [93] recently developed a numerical model taking into account all the interactions including Knudsen diffusion, molecular diffusion, and viscous friction. Their measurement of the Knudsen diffusion was based on the permeability measurement, which is similar to the model used by Kast and Hohenthanner [110]. For the case of MPL samples studied here, however, the mean free path is not significantly larger than the

pore diameter (see the Knudsen numbers in Table 3-3). Thus, Knudsen diffusion is ignored. This will not overestimate the diffusion coefficient even by a small amount.

The model developed to correlate the crossover amount to the diffusion coefficient requires a 3-D concentration profile, and hence the velocity profile, in the flow channel. The model for the velocity profile and the pressure profile is developed in COMSOL. The Navier-Stokes equations are solved for the flow plate geometry mentioned in Section 3.4. The assumptions made are listed below:

- Steady state condition: All the measurements are recorded when the operational parameters and the GC readings reach the steady state condition.
- Isothermal condition: The measurements are taken at the room temperature. Thus, any variations in the temperature should not exceed $\pm 2^\circ\text{C}$. This small variation is neglected.
- No chemical reaction and ideal gas behavior
- No convection: The differential pressure across the GDL is kept at a value close to zero. The permeability of the MPL samples is also very small (see Table 3-2). Therefore, the crossover due to convection will be very small based on the Darcy's law

$$Q = \frac{kA\nabla P}{\mu * x} \quad (3.3)$$

where k is permeability, A is the cross-sectional area, μ is viscosity, and ∇P is the pressure difference. For instance, the value of Q (crossover due to convection) for AvCarb EP40T12 CBT18 (low) is $3.066 \times 10^{-14} \text{ m}^3/\text{s}$ when the pressure difference is 1Pa.

- Laminar flow
- No slip boundary condition
- Through-plane diffusion: diffusion is considered only in the through-plane direction, along the thickness of the GDL. In-plane diffusion is ignored.

For the diffusion process, a finite element analysis (FEA) is conducted. A mesh is generated where the length (9cm), the width (8.4mm), and the depth (2.5mm) are divided into 9000, 84, and 25 unit cells, respectively. The initial oxygen concentration in the air side is assumed as 21% of the total concentration (i.e., 5.477×10^{-5} mol/cm³) and in the nitrogen side is considered 0%. The mesh grid consists of two flow plates and the GDL. Bulk diffusion is considered along the width and the height of the flow plate; while the transport along the length is considered to be flow driven. Therefore, the concentration within a unit cell depends on the diffusion flux across the height and width and viscous flux along the length. Figure 3-14 shows the schematic of the flux across the unit element where x axis is parallel to the flow direction, y axis presents the through-plane direction, and z axis is perpendicular to the flow. The Fick's law is used to obtain the concentration profile across the entire mesh grid. The velocity profile is imported from COMSOL.

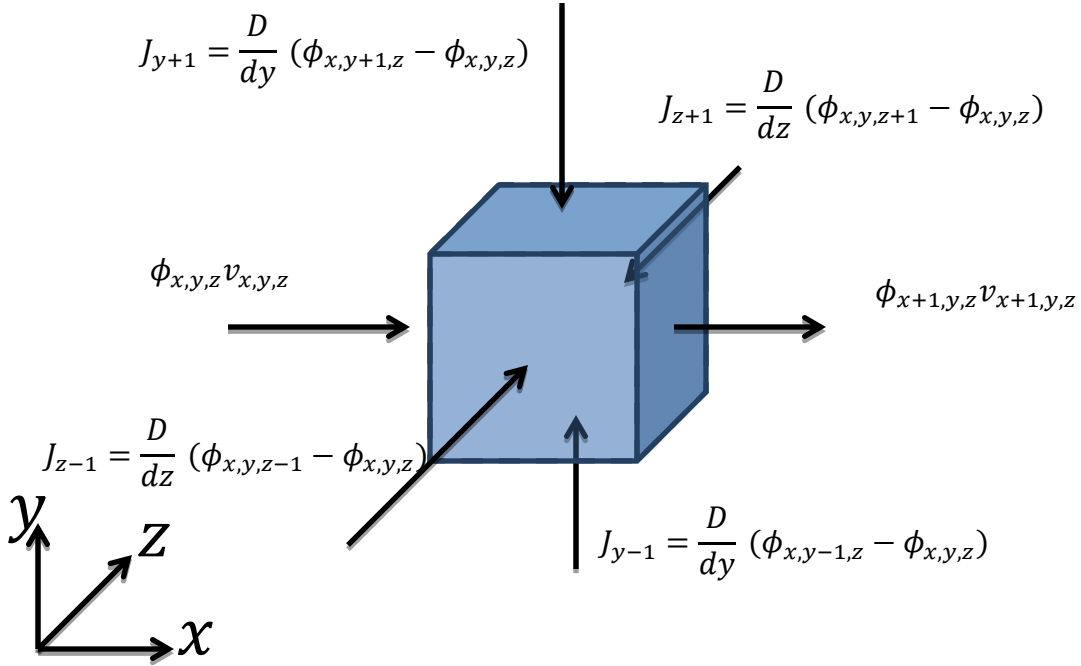


Figure 3-12: Unit element of the mesh grid

Based on the conservation of mass, the output concentration, ϕ ($\frac{mol}{cm^3}$), leaving the unit can be found as

$$\phi_{x+1,y,z} = \frac{v_{x,y,z} \phi_{x,y,z} dy dz + (J_{y+1} + J_{y-1}) dx dz + (J_{z+1} + J_{z-1}) dx dy}{v_{x+1,y,z} dy dz} \quad (3.4)$$

where, v ($\frac{cm}{s}$) and J ($\frac{mol}{cm^2 s}$) present the flow velocity and the flux, respectively. The analysis shown above can be used to obtain the concentration profile in the entire geometry. At the GDL-flow plate interface, the flux along the y-direction (i.e., the through-plane direction) is influenced by the GDL diffusivity and the thickness of the GDL. At this interface, the diffusivity component consists of both the diffusivity in the air, D_{air} , and diffusivity across the GDL, D_{GDL} . Thus, the flux along the y-direction can be written in the form of

$$J_{y-1} = \left(\left(\frac{D_{air}}{dy} \right)^{-1} + \left(\frac{D_{GDL}}{t} \right)^{-1} \right)^{-1} (\phi_{x,y-1,z} - \phi_{x,y,z}) \quad (3.5)$$

where, t presents the thickness of the GDL. The analysis shown above has two unknowns: the GDL diffusivity (D_{GDL}) and the output oxygen concentration ($\phi_{x,y,z}$). Therefore, the result will yield a curve relating the oxygen concentration to the diffusion coefficient per unit thickness of the GDL (see Figure 3-15). For a particular oxygen concentration obtained from GC, the corresponding GDL diffusivity value can be calculated by multiplying the diffusion constant obtained from this curve by the GDL thickness.

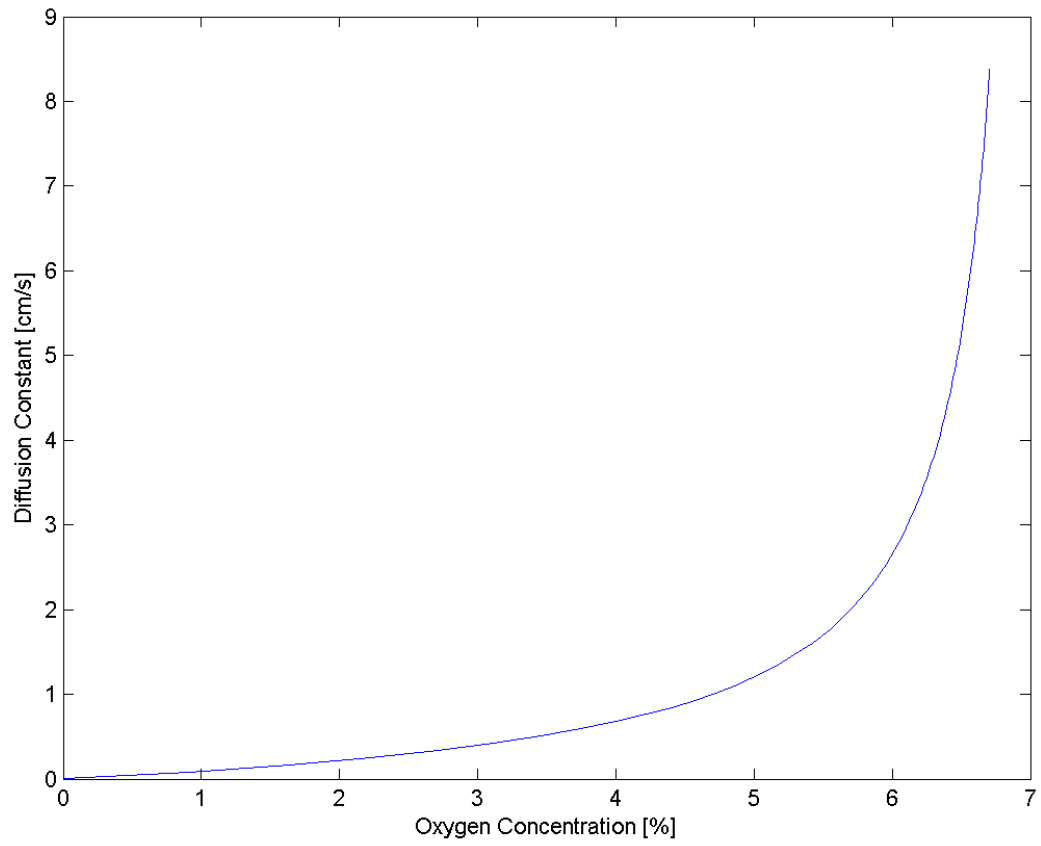


Figure 3-13: Diffusion coefficient versus oxygen concentration obtained as a result of the FEA based data analysis program

CHAPTER 4: RESULTS AND DISCUSSION

The results for water transport and gas diffusion in different GDLs are presented in this chapter. The water transport results are presented in Section 4.1. The measurements are conducted using the first and second generation setups. Using the first generation (Sections 4.1.1), the time of breakthrough, the breakthrough pressure and the impact of expansion are presented. A more detailed analysis is conducted using the second generation setup (Sections 4.1.2). Results obtained from the second generation setup are analyzed to study the effect of hydrophobicity (measured in terms of the internal contact angle), the mean pore diameter, and the thickness on the breakthrough time and pressure. SEM images shown also provide a better understanding of the results.

The results for the diffusivity measurements obtained using the setup described in Chapter 3 are presented in Section 4.2. The dry diffusivity results are analyzed in terms of porosity and thickness. These results are compared with those obtained from the theoretical correlations and experimental measurements reported in the literature. The wet diffusivity measurements are presented and compared with the dry diffusivity results. Finally, the influence of the internal contact angle on the wet diffusivity measurement is shown.

4.1 Results for water transport

In this section, the results obtained from both setups are presented. As pointed out in Chapter 2, the first generation setup has limitations, and the sources of errors are shown in this section. These limitations are rectified in the second generation setup which is used to study the structural and transport properties of the GDLs.

4.1.1 First generation setup

In this subsection, the time of breakthrough and the breakthrough pressure measurements obtained from the first generation setup are presented and discussed. Four different GDL samples (purchased from Toray Industries) with different thicknesses (190 μm (Toray TGP060) and 280 μm (Toray TGP090)) and hydrophobicity levels (0% and 40% wt. PTFE loadings) are used.

4.1.1.1 Breakthrough Time and Pressure

Results for the breakthrough pressure are presented in Figure 4-1. The results indicate that between two samples with the same thickness a higher breakthrough pressure is obtained for a more hydrophobic sample. This is because the pattern for water invasion in a porous GDL differs based on the hydrophobicity level of the medium. Therefore, water is expected to invade the hydrophobic and the hydrophilic pores differently [97]. In essence, the pressure required for water to penetrate the GDL increases as hydrophobicity increases.

The breakthrough pressure is also larger for thicker samples. However, the effect of the thickness on the breakthrough pressure is not as significant as the effect of hydrophobicity. Thickness adds additional pathways that water needs to travel before it breaks through. These pathways of water are not along straight lines due to the porous and tortuous nature of the GDL. As the thickness increases, the water must overcome an additional resistance (due to the addition of the thickness) before the event of breakthrough. Figure 4-1 also shows that for the 32% increase in the thickness (from 190 μm to 280 μm) the change in the breakthrough pressure is 14.8% and 14.0% for untreated (0% wt. PTFE loaded) and treated (40% wt. PTFE loaded) samples, respectively. By adding the PTFE loading, the breakthrough pressure increases by 23.2% and 22.5% for the thin (190 μm) and thick (280 μm) samples, respectively.

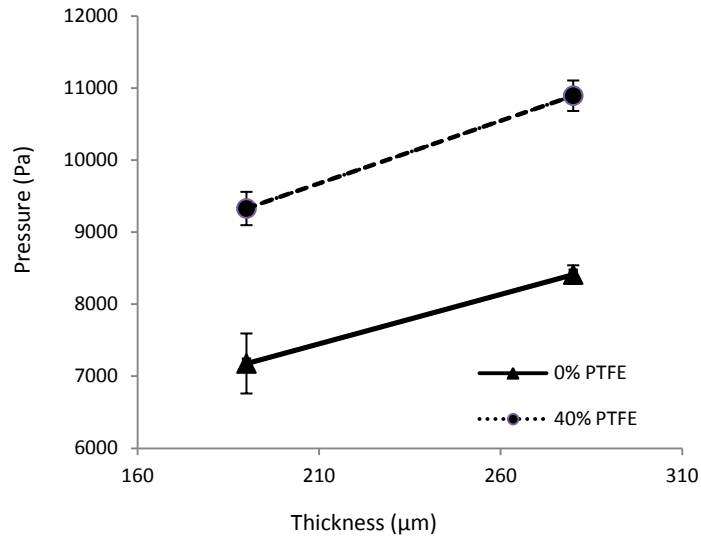


Figure 4-1: Breakthrough pressure of the hydrophobic and hydrophilic samples with different thicknesses

The larger breakthrough pressure for the hydrophobic samples can also be explained by the Young-Laplace equation [111] which relates the capillary pressure of a medium to its morphological and geometric properties. The capillary pressure of the porous medium is the pressure difference between the two phases (air and liquid). During water penetration, water is the displacing phase and air is the displaced phase. Therefore, for water removal, the displacing phase (water) needs to have a larger pressure than the displaced phase (air) to overcome the capillary pressure related to the liquid-gas surface tension (γ), the contact angle (θ), and the pore diameter (d). When a GDL is treated with PTFE, it is shown [103] that the average internal contact angle increases. The change in the average internal contact angle reflects the change in the local contact angle of the pores.

$$P_{liquid} - P_{gas} > \frac{4\gamma\cos\theta}{d} \quad (4.1)$$

The results showed in Figure 4-1 are analyzed using t-test values at the 95% confidence interval to check whether the difference is statistically meaningful. It was found that the t-test values for samples with different thicknesses and the same hydrophobicity level are 4.36 (190 μm) and 4.88 (280 μm); while the t-critical value was found to be 2.77 at the 95% confidence interval. Since these values are larger than the t-critical value, one can conclude that the null hypothesis stating that both samples are the same can be rejected. Therefore, the difference between the measurements of the samples of two thicknesses and the same hydrophobicity is statistically meaningful. The same test was conducted for the samples with the same thickness and different levels of hydrophobicity. The t-values were again larger than the t-critical value, suggesting that the difference between the measurements of these samples is also statistically meaningful.

When water approaches a pore of the GDL, the invasion of the pore depends on two factors: the hydrophobicity of the pore and the capillary pressure required to penetrate the pore. When a pore contains hydrophobic agents (like PTFE), it is expected to repel water. For a given capillary pressure, a hydrophobic medium offers less number of pores that are available for liquid water invasion compared to a hydrophilic medium with the same porosity. Therefore, water may have to travel around a tortuous path in order to break through in a hydrophobic GDL. As a result, the time of breakthrough is expected to be greater for a hydrophobic sample compared to that of a hydrophilic sample. Moreover, the breakthrough pressure for the hydrophobic sample is larger than the hydrophilic sample as explained above. This essentially means that water will penetrate the GDL only when enough pressure is generated to overcome the large resistance of the hydrophobic pores. For generating a large pressure, more water needs to be injected within the control volume. The syringe pump needs to run for a longer period of time to inject the extra

amount of water. As a result, higher time of breakthrough was observed for the hydrophobic samples compared to the hydrophilic samples. The experimental results of the time of breakthrough obtained for different GDLs verify the above discussion (see Figure 4-2). The changes in time of breakthrough for different hydrophobicity and thickness levels are similar to that obtained for the breakthrough pressure shown in Figure 4-1.

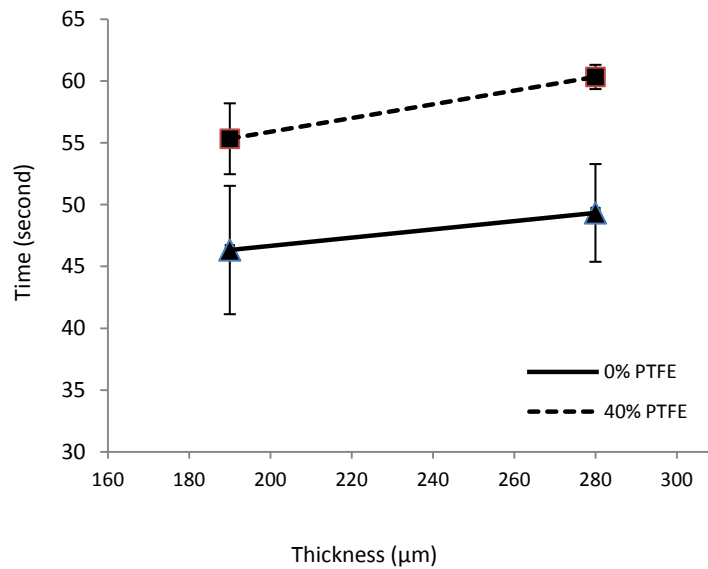


Figure 4-2: Time of breakthrough of the hydrophobic and hydrophilic samples with different thicknesses

Figure 4-2 shows that for the 32% increase in the thickness (from 190 μm to 280 μm) the change in the breakthrough time is 6.1% and 6.7% for untreated (0% wt. PTFE loaded) and treated (40% wt. PTFE loaded) samples, respectively. By adding the PTFE loading, the breakthrough time increases by 17.8% and 18.3% for the thin (190 μm) and thick (280 μm) samples, respectively.

The results showed in Figure 4-2 are also analyzed using t-test values at the 95% confidence interval to check whether the difference is statistically meaningful. It was found that the t-test

values for samples with different thicknesses and the same hydrophobicity level are 0.66 (190 μm) and 1.79 (280 μm); while the t-critical value was found to be 2.77 at the 95% confidence interval. Since these values are larger than the t-critical value one can conclude that the null hypothesis stating that both samples are the same can be rejected. Therefore, the difference between the measurements of the samples of two thicknesses and the same hydrophobicity is statistically meaningful. The same test was conducted for the samples with the same thickness and different levels of hydrophobicity. The t-values were again larger than the t-critical value, suggesting that the difference between the measurements of these samples is also statistically meaningful.

SEM images of the samples tested are presented in Figures 4-3 and 4-4 to show qualitatively the difference in the microstructure and morphology of the GDLs with different PTFE loadings. The figure in the left (an image of a hydrophilic sample) clearly provides additional passages for water transport. When the PTFE is loaded, GDLs (the figure in the right) are covered with a film preventing water movement. Thus, the number of pores available for water transport is undoubtedly larger for the hydrophilic sample; whereas a significant drop in the number of pores ready to accept water is observed for the hydrophobic GDLs.

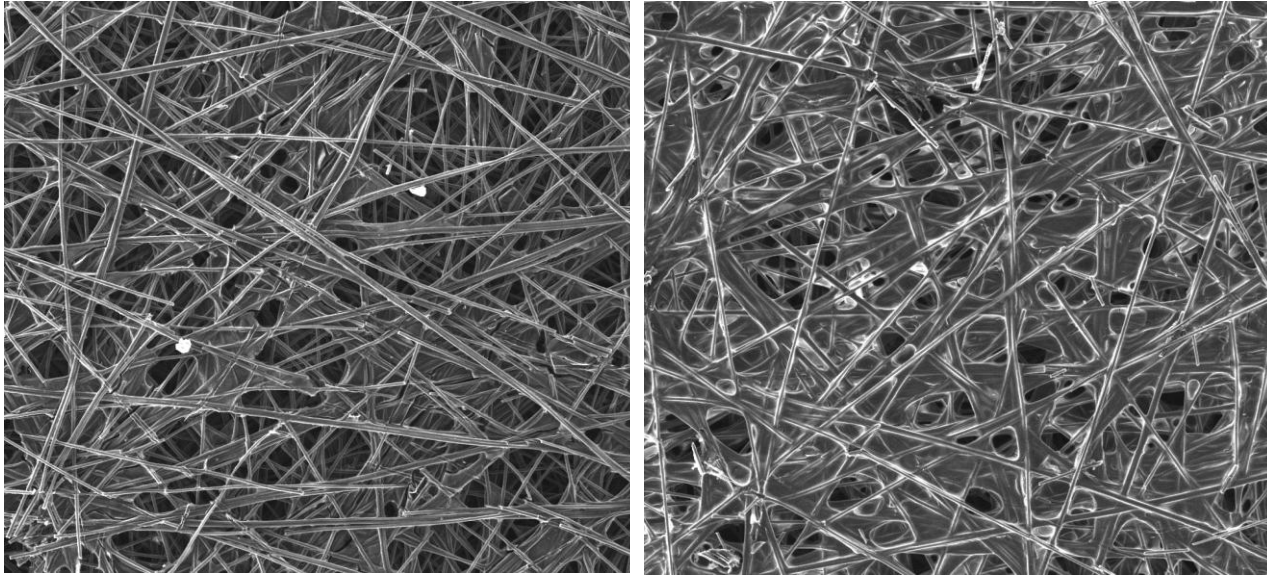


Figure 4-3: SEM images (200X magnification) of Toray TGP060-0% wt. PTFE (left) and Toray TGP060-40% wt. PTFE (right)

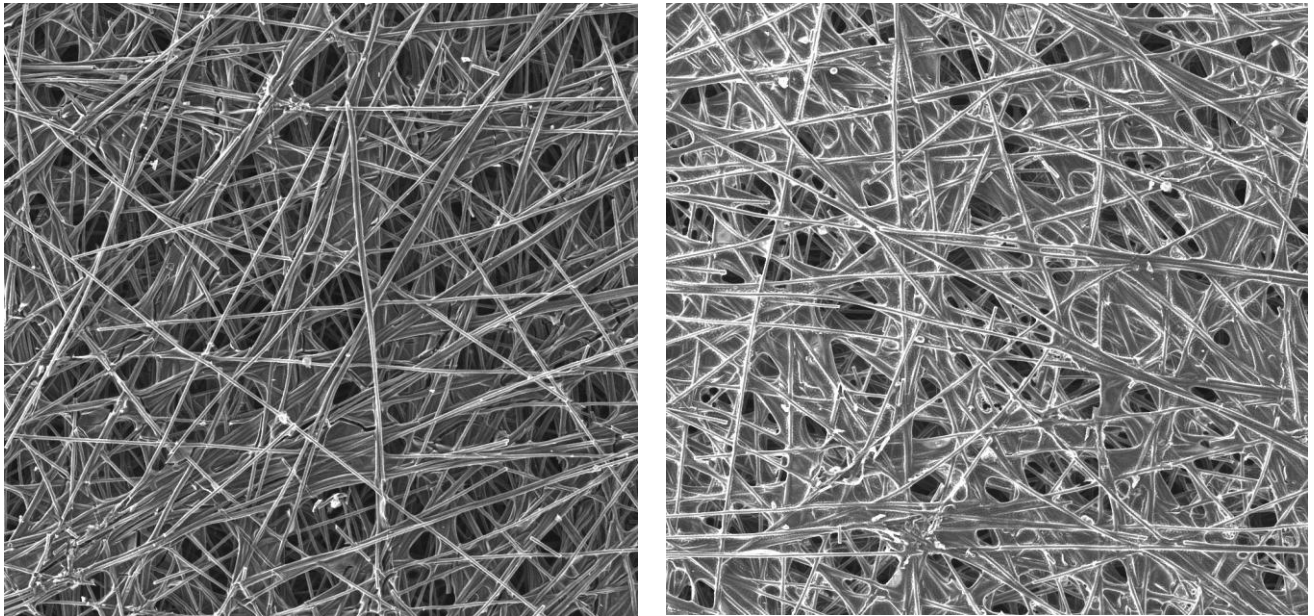


Figure 4-4: SEM images (200X magnification) of Toray TGP090-0% wt. PTFE (left) and Toray TGP090-40% wt. PTFE (right)

The preferential growth of the droplet along the wall of the pressure cylinder used to apply sufficient pressure on the GDL can also be explained by the SEM images. It was already discussed in Chapter 2 that the GDL undergoes morphological changes at the point of contact between the pressure cylinder and the GDL. The loss of hydrophobicity in the samples under compression has been observed in the past [58]. This apparent loss of hydrophobicity results in creating segments with high saturation. This phenomenon can be explained by Figure 4-5 showing the SEM images of a piece of the GDL cut from the area being under compression by the pressure cylinder in the setup (Chapter 2). Disjointed fibers caused by the compression can be observed. It is apparent that the GDL undergoes breakage due to the application of the compression force. The fibers break in a way that a clear opening is formed for water transport. This breakage is more severe for thin and hydrophilic samples like Toray 60-0% wt. PTFE shown in Figure 4-5. However, PTFE adds rigidity to the structure. So, the problem is less noticeable for thick and hydrophobic (larger PTFE loadings) samples.

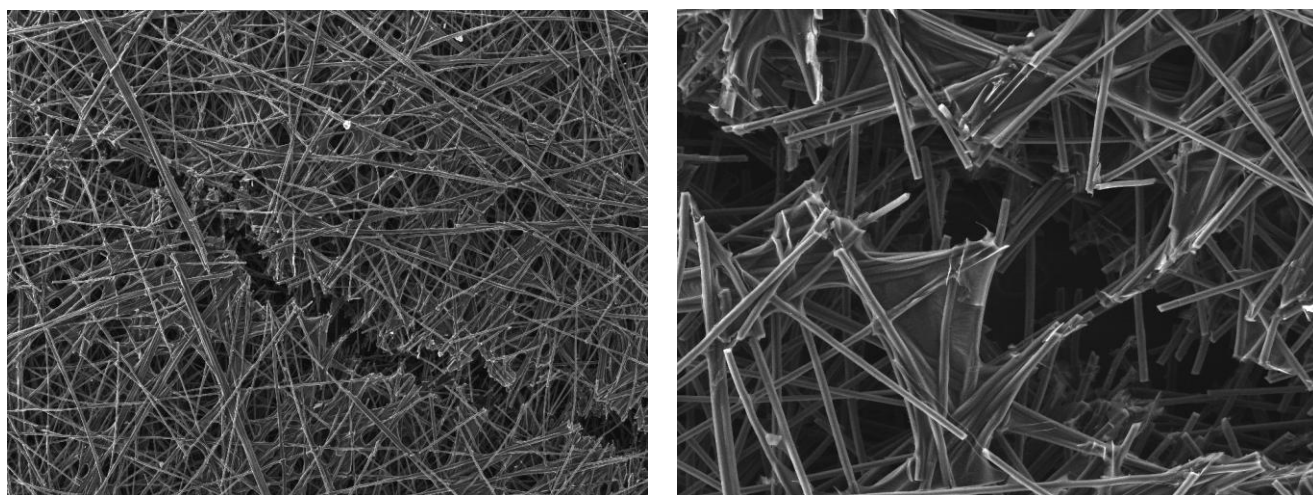


Figure 4-5: SEM images of the TGP060-0% wt. PTFE sample that has been under compression: 200X zoom (left) and 500X zoom (right)

After the event of breakthrough, the flow pattern inside the sample depends on the porous medium. For a hydrophobic sample, water movement is mostly restricted within the paths that have already been established since there is a high probability that the neighboring pores might also contain hydrophobic agents repelling water. To intrude the neighboring pores, a large pressure is required. Therefore, the injected water will fill the pores that have already been intruded and follow the established pathway on the way out. Water transport after breakthrough is, however, different in the hydrophilic GDLs. As the pores around those initially invaded do not repel water, water flows in both the through-plane and the in-plane directions. Thus, after initial invasion, water travels to the other void spaces instead of filling the pores already invaded and instead of continuing along the established pathway, like the hydrophobic samples. This explains the branching mechanism observed for water transport in the hydrophilic GDLs.

The difference in the time of breakthrough of the hydrophobic and the hydrophilic GDL samples shed light on the relative water flow rate within these samples. In essence, the hydrophilic sample is expected to retain more water due to its morphological structure [26]. However, the hydrophobic sample has a larger time of breakthrough. This indicates that the volume of water (or saturation) at the point of breakthrough, obtained by simply multiplying the time of breakthrough by the syringe-pump flow rate, will be larger for the hydrophobic samples which is opposite to the results reported in the past. One may conclude that the calculation of saturation (the water content) based on the assumption of a constant flow rate might produce erroneous results. Since the pathway of water is not straight and smooth due to the porous and tortuous nature of the GDL, water experiences many obstacles on its way. A hydrophobic sample is expected to offer a significantly larger number of obstacles for water flow due to the presence of PTFE. As a result, the water flow rate in a hydrophobic sample can be expected to be lower

than that in a hydrophilic sample. Recent experimental measurements of the flow in and around the GDL with different PTFE loadings conducted by Gauthier et al. [112] verify the above discussion. Gauthier et al. [112] showed that the water flow rate in a typical GDL varies based on the PTFE loading. They showed that the water flow rate drops around 30% when PTFE loading is increased from 5% to 20%. More interestingly, they showed that the water flow rate drops to 70% when PTFE loading is increased from 5% to 40%. Therefore, the estimation of saturation (the water content) based on the assumption of a constant flow rate (flow rate of the syringe pump) is wrong.

4.1.1.2 Impact of Expansion

The water content inside the GDL can be obtained by multiplying the breakthrough time by the flow rate. The widely used assumption of the constant flow rate (obtained from the syringe pump) [26] overestimates the water content (saturation) due to the reason described in the previous section. Another potential source of error in the estimation of the water content is the time of breakthrough. As the pressure within the system rises to the breakthrough pressure (~10,000Pa), the flexible components (like FEP tubing) expand affecting the results of the time of breakthrough. Following the procedure described in Chapter 2, this expansion can be calibrated to correct the time of breakthrough and hence the water content inside the GDL. The results of this correction are presented in Figure 4-6. For all the samples, the values of the water content decrease significantly (more than 50%) when the correction is applied. The difference in the water content of GDLs with different thicknesses diminishes when expansion is considered showing the fact that thickness does not have a significant influence on the time of breakthrough. The difference in the water content of the hydrophobic and the hydrophilic sample is also

significantly smaller when expansion is considered. Moreover, as a result of expansion, the droplet formed at the point of breakthrough might have even a larger volume than the water content inside the GDL. This phenomenon which may result in the reduction of saturation at that instant happens due to the rapid purge of water at the event of breakthrough as a result of the pressure build-up due to expansion.

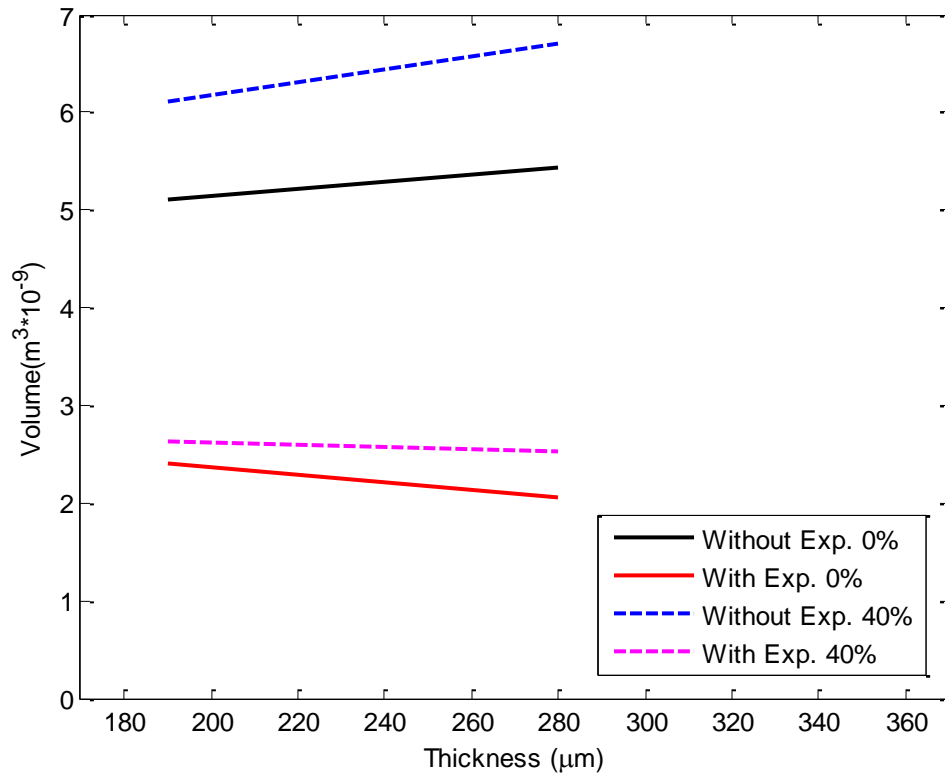


Figure 4-6: Water content inside the GDL with and without considering the expansion of flexible components for different PTFE loading and thickness level

The above results show that the impact of expansion is not negligible. The calibration for the effect of expansion can also cause errors in the results corrected (see the decrease in the water content as the thickness increases). The results presented here were obtained for the flow rate of 400μL/hr which is 10 times larger than the flow rate corresponding to the limiting current at the

flooding condition. For a smaller flow rate, the impact of expansion is expected to be even more significant. Therefore, to measure accurately the time of breakthrough it is essential to conduct the measurements in a non-expandable setup. This serves as the motivation for the development of the second generation setup.

4.1.2 Second Generation Setup

The second generation setup enables the accurate measurement of the breakthrough time and pressure. A number of GDLs made by different manufacturers are tested. The results are then correlated to the morphological and transport properties of the GDLs. Figure 4-7 shows the results of the breakthrough pressure obtained from the first and second generation setups. The results are also compared to those reported in the past [25]. All the measurements were conducted at the flow rate associated with the flooding condition (i.e., the flow rate of 40 μ L/hr for the first and second generation setups). It is noted that the breakthrough pressure obtained using the second generation setup is in general larger than those obtained using the first generation or the other method [25]. The major difference between the first and second generation setups is the use of flexible FEP tubing. In the first generation setup, when water touches the bottom surface of the GDL, the pressure starts to rise as the GDL offers resistance to the free flow of water. As more water is injected, the pressure increases more at the GDL-water interface. This pressure build-up is experienced by all the components including the flexible tubing which expands and hence reduces the effect of the pressure build-up sensed by the membrane of the pressure sensor. As a result, the breakthrough pressure output of the sensor is smaller in the first generation setup. On the other hand, the components of the second generation setup are not expandable so all the pressure generated at the GDL-water interface is sensed by the membrane of the pressure sensor. As a result, the pressure sensor displays the true value of

the breakthrough pressure. It is also interesting to see that the breakthrough pressures reported in the literature [25] is smaller than those obtained using the second generation setup. This is due to the fact that the experimental setup in [25] also uses flexible components.

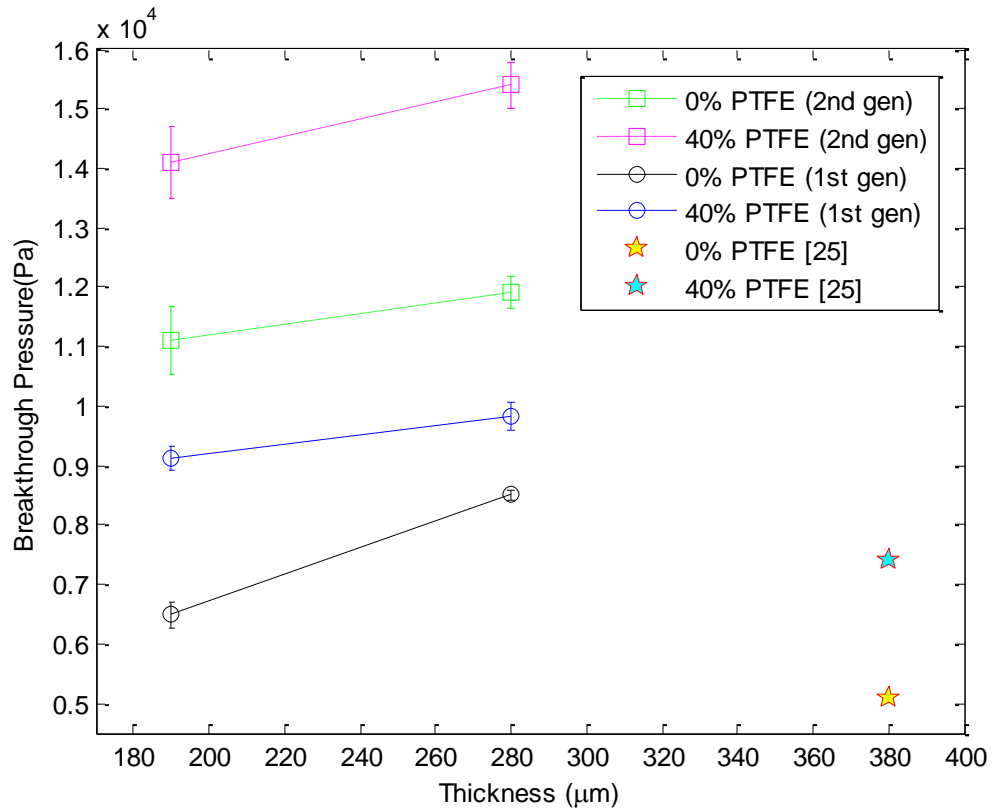


Figure 4-7: Comparison between the breakthrough pressure values obtained using the first and second generation setups and those reported in [25]

Figure 4-8 below compares the time of breakthrough obtained using the first and second generation setups. In general, the time of breakthrough measured using the second generation setup is smaller. For the hydrophobic samples, the effect of the sample thickness on the time of breakthrough is less compared to that observed for the hydrophilic samples. In general, the difference between the time of breakthrough obtained for the hydrophobic and hydrophilic samples is more pronounced for the thin samples.

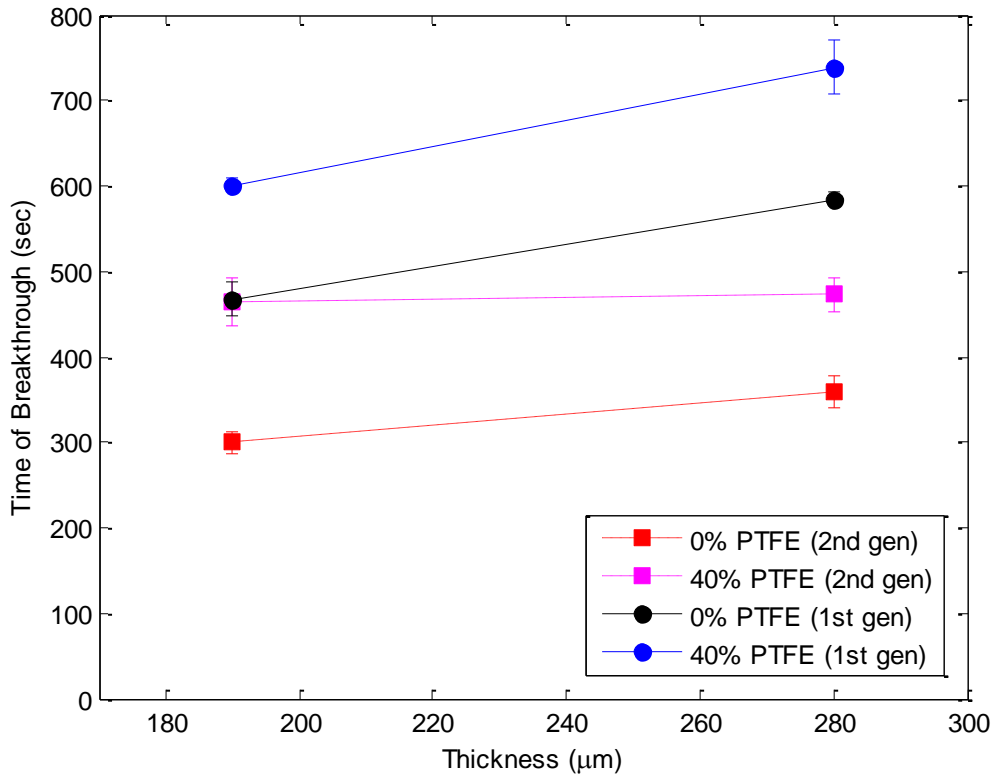


Figure 4-8: Comparison between the time of breakthrough for GDLs with different thickness and hydrophobicity level obtained using the first and second generation setups

A wide variety of other GDL samples are also tested using the second generation setup. The relationship between the breakthrough time and pressure and the internal contact angle [103] (measured using the capillary penetration technique) is shown in Figures 4-9 and 4-10. As more PTFE is added to the sample (see the SEM images in Figure 4-11), the internal contact angle increases. In essence, the samples which contain larger amount of PTFE loadings have a higher tendency to repel water. This tendency attributes to the increased breakthrough pressure and time as shown in the figures below.

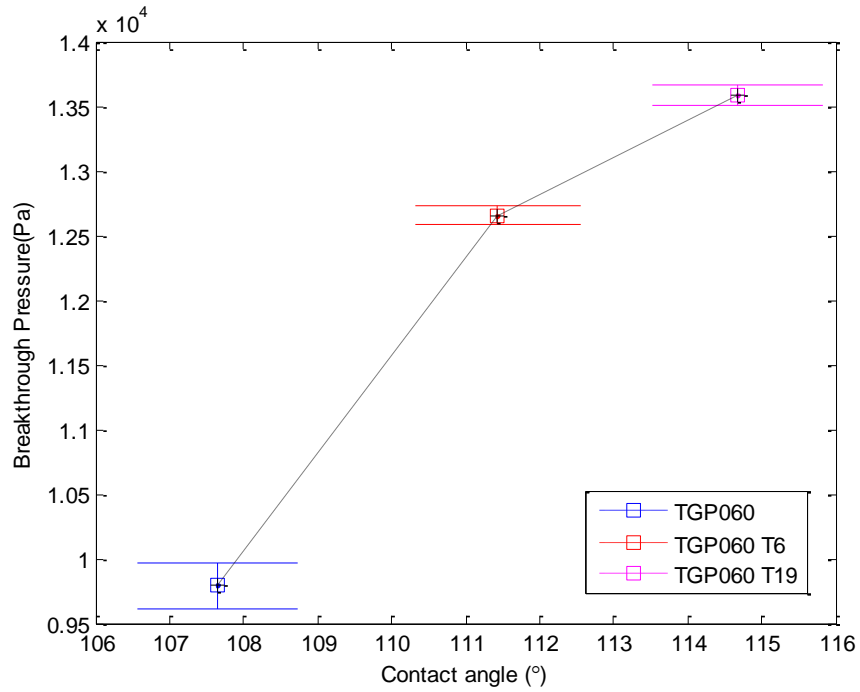


Figure 4-9: Change in the breakthrough pressure with the change in the internal contact angle. The contact angles were taken from [103]

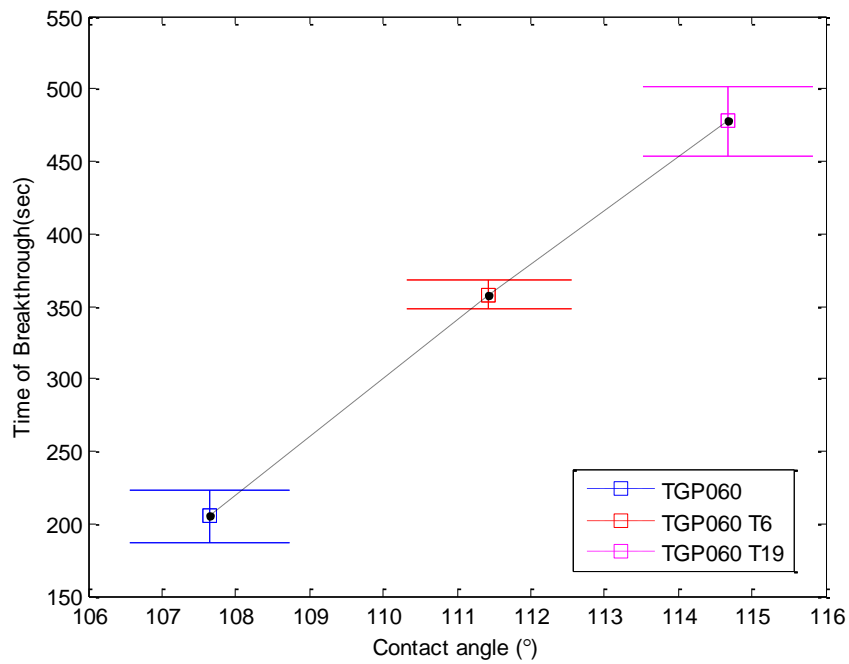


Figure 4-10: Change in the time of breakthrough with the change in the internal contact angle. The contact angles were taken from [103]

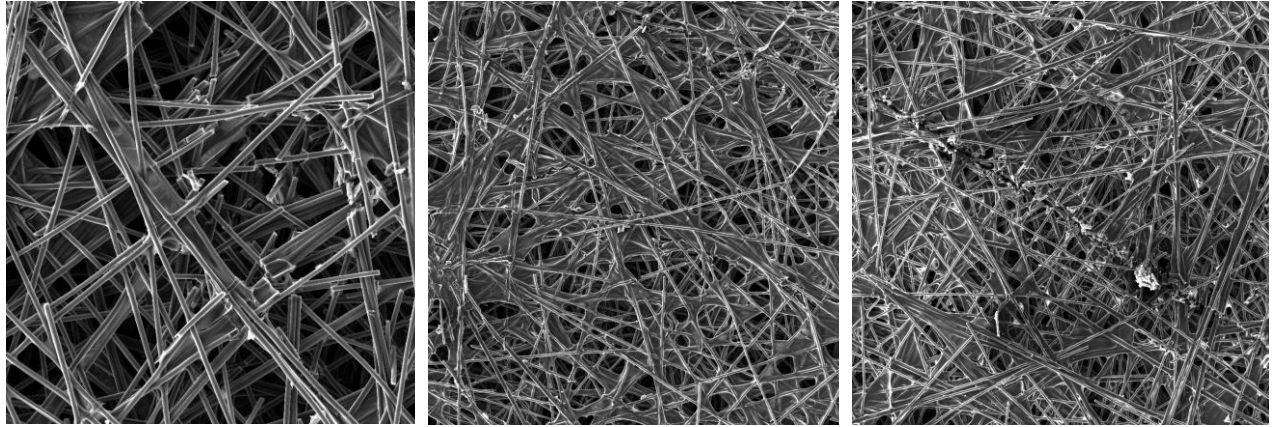


Figure 4-11: SEM images of TGP060 (500X magnification left), TGP060 T6 (200X magnification middle) and TGP060 T19 (200X magnification right)

The relationship between the breakthrough pressure and the mean pore diameter is presented in Figure 4-12. It has been shown [103] that the mean pore diameter decreases as the PTFE loadings increase. Thus, the breakthrough pressure for samples with a smaller mean pore diameter (having higher PTFE loadings) is larger. This can also be explained by the Young-Laplace equation (Eq. 4.1). A similar trend has been observed for the time of breakthrough which is smaller for samples with larger mean pore diameters. The relationship between the breakthrough pressure and time and permeability is expected to be similar to that observed with the mean pore diameter, as a larger mean pore diameter relates to larger permeability.

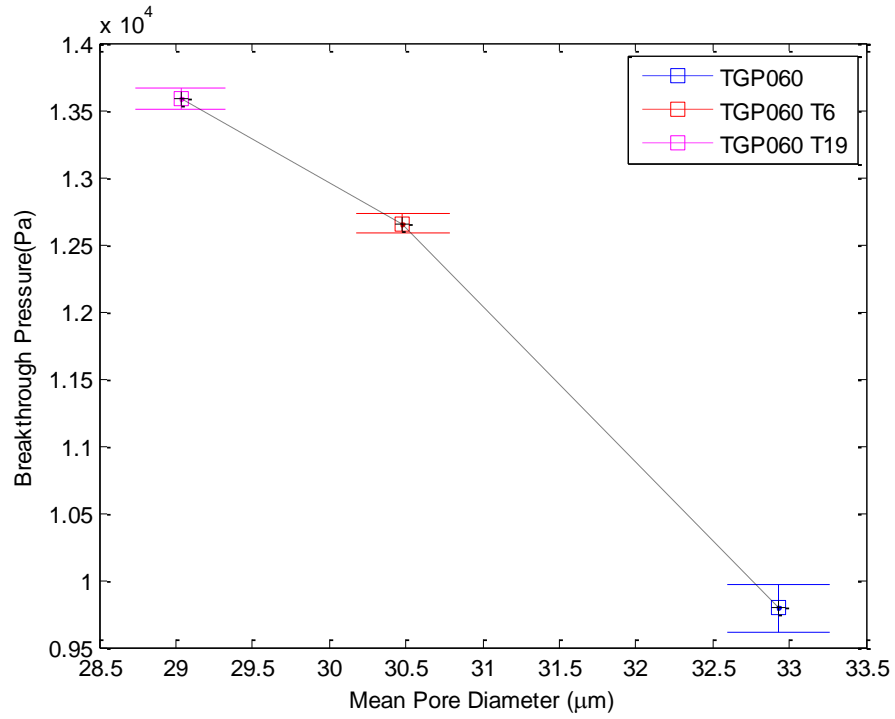


Figure 4-12: Change in the breakthrough pressure with the change in the mean pore diameter. The mean pore diameters were taken from [103]

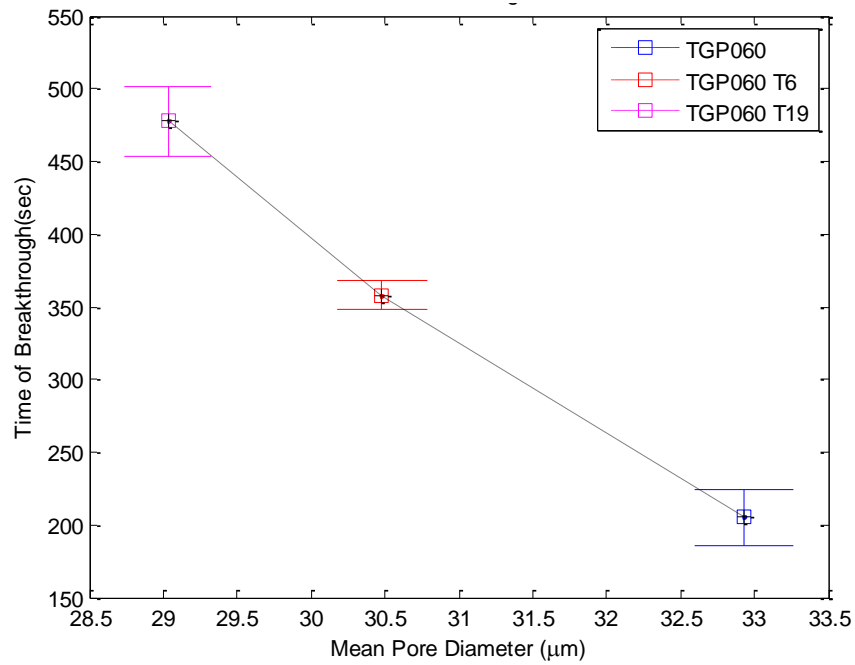


Figure 4-13: Change in the time of breakthrough with the change in the mean pore diameter. The mean pore diameters were taken from [103]

Experiments are also conducted for GDL samples made of carbon clothes. Two E-lat carbon cloth samples purchased from BASF Fuel Cell are used. One of the samples is thin and hydrophilic; while the other sample is thick and hydrophobic. In addition to the E-lat carbon clothes, P50 samples made by AvCarb are also tested. The results are shown in Figure 4-14. It is evident that as the hydrophobicity of the sample increases, the breakthrough time and pressure increase. The SEM images presented in Figures 4-15 and 4-16 provide an insight into the structural properties of these samples. In essence, the number of pores covered by PTFE is substantially large for the hydrophobic P50 sample (i.e., P50 T33). The SEM images of the carbon cloth samples also shows that the thick sample has a coating of hydrophobic powders on one side which does not exist on the hydrophilic sample. This might be the reason for obtaining the largest breakthrough pressure for this sample.

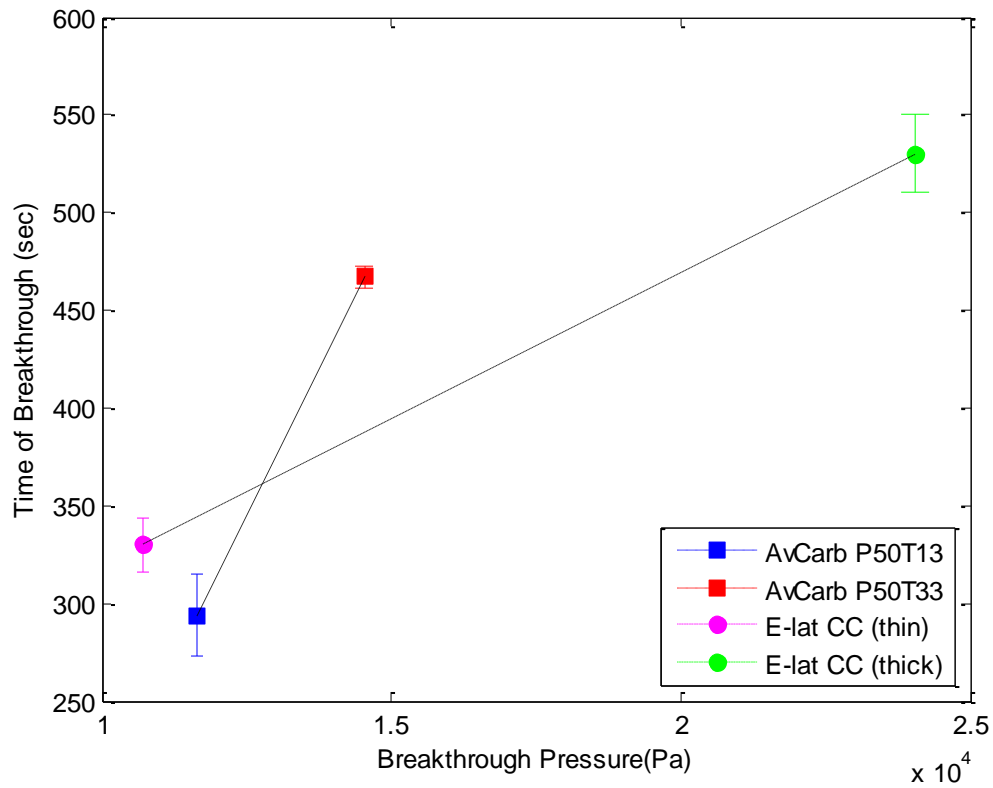


Figure 4-14: Breakthrough time and pressure for E-lat carbon cloths and AvCarb P50 samples with different hydrophobicity

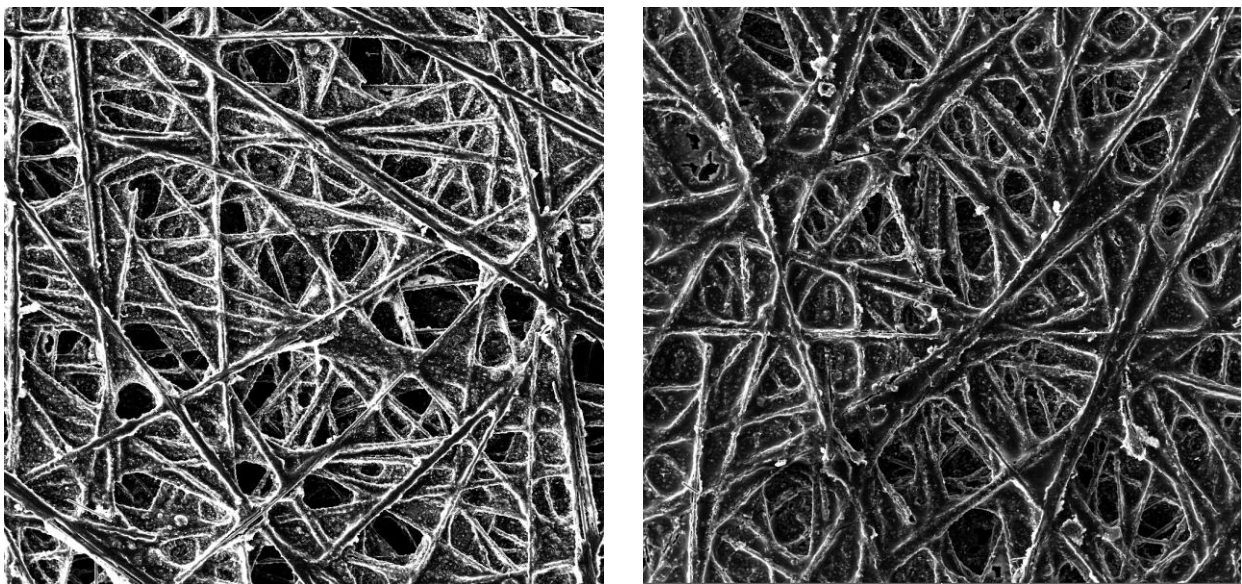


Figure 4-15: SEM images (200X magnification) of P50 T13 (left) and P50 T33 (right)

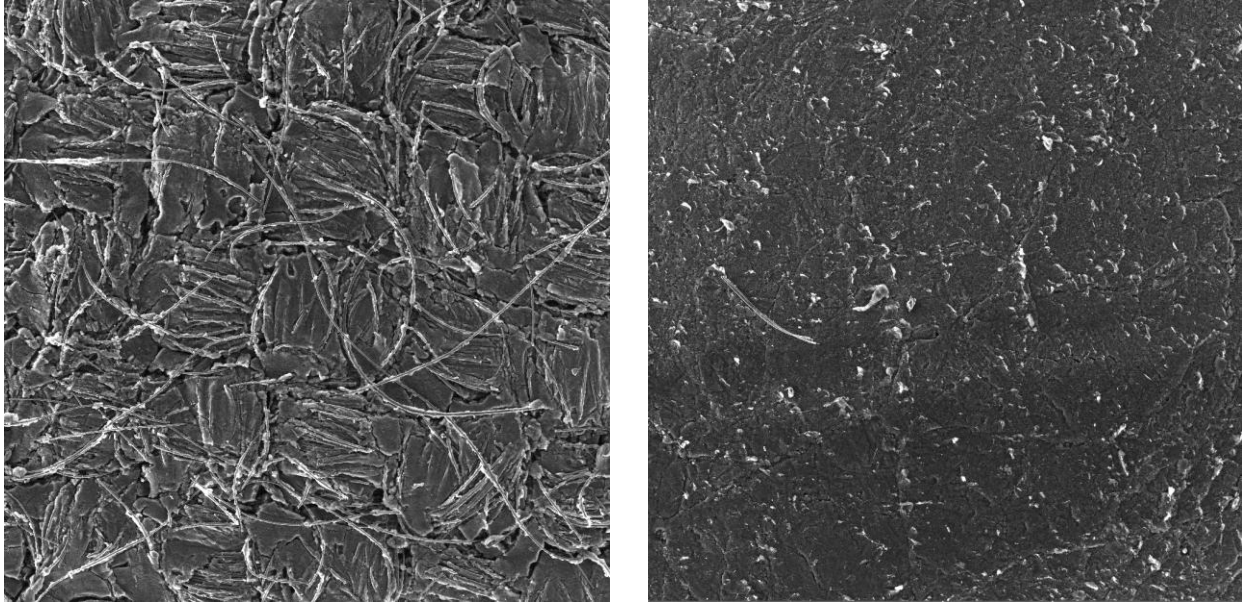


Figure 4-16: SEM images (100X magnification) of E-Lat thin, hydrophilic (left) and E-Lat thick, hydrophobic (right)

The capillary pressure curves obtained for the carbon cloths and papers showed different patterns. Figure 4-17 presents the pressure sensor output for a Toray and carbon cloth sample. For the carbon paper (Toray sample), the pressure drops abruptly to its initial value at the point of breakthrough where the droplet emerges from the surface of the sample. However, for the carbon cloth sample, the pressure does not drop to its initial capillary pressure at the breakthrough instant. Instead, the pressure drops only when the droplet grows to a certain size. The same trend has been observed in all the tests conducted with the carbon cloth samples.

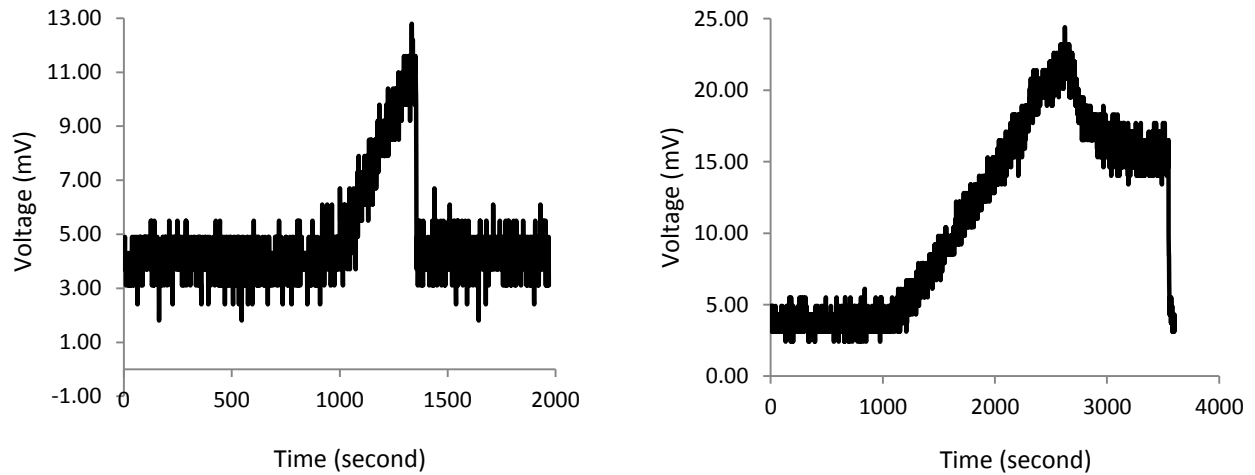


Figure 4-17: The output of the pressure sensor for TGP 60 40% wt. PTFE carbon paper (left) and E-lat carbon cloth (thick-hydrophobic) (right)

Finally, the hysteresis in the breakthrough time and pressure is studied by reusing the samples. It has been reported in literature that the water transport characteristic in the GDL that is already wet is different than that observed in a complete dry sample [113]. As water travels through the pores, it creates a film reducing the hydrophobicity (or wettability characteristics) of the sample. To investigate this phenomenon, the samples are reused again for the measurement of the breakthrough time and pressure. The results of this study are presented in Figure 4-18 for two Toray samples with different hydrophobicity (T6 versus T19). It is observed that breakthrough time and pressure reduce from their original values for the reused samples. Also, the change in the breakthrough time and pressure is more significant after the first reuse and reduces for the runs after.

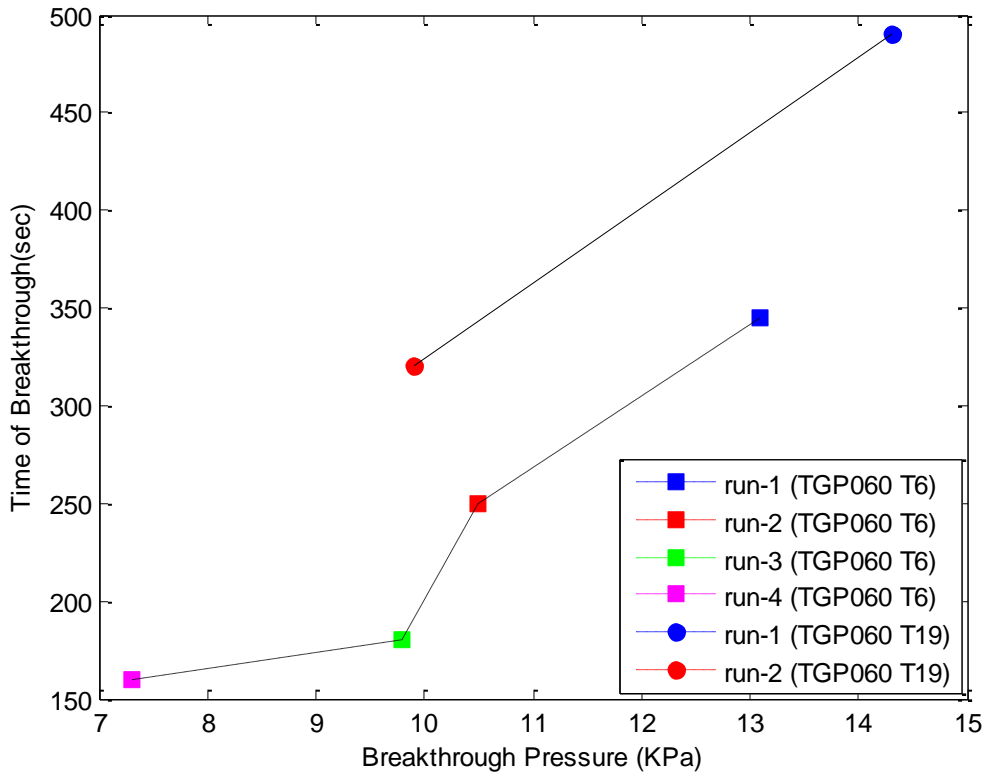


Figure 4-18: Breakthrough time and pressure for reused samples showing a shift towards hydrophilic characteristics

4.2 Results for gas diffusivity

The results for the diffusivity measurements conducted using the setup described in Chapter 3 are presented in this section. The relationship between diffusivity of dry samples and their porosity and thickness is studied. The effect of the pressure difference across the two sides of the GDL on the diffusivity results is shown. The dry diffusivity results are also compared to the theoretical and experimental results presented in the literature. Then, the wet diffusivity measurements are compared with those obtained during dry diffusivity experiments. Finally, the relationship between wet diffusivity and the internal contact angle of the GDLs are investigated.

4.2.1 Effect of Porosity on Diffusivity

Porosity is the ratio of the pore volume to the total volume of the sample. It is well-known that a sample with higher porosity provides more pathways for reactant transport. Thus, a higher porosity sample is desired when the cell is operated at high current densities [114]. Figure 4-19 shows the relationship between diffusivity and porosity for the AvCarb and Toray samples. The porosity values were measured at the Ballard facility. It is evident that as the porosity increases the dry diffusivity value increases. Even a small increase in porosity contributes to a large increase in the diffusion coefficient. Samples made by Sigracet were also tested to investigate whether the trend continues for samples from different manufacturers. The results of the SGL samples are presented in Figure 4-29. The porosity values for these samples were provided by the manufacturer. The results show the same trend as that observed for the previous samples. In essence, diffusivity increases with the increase in porosity.

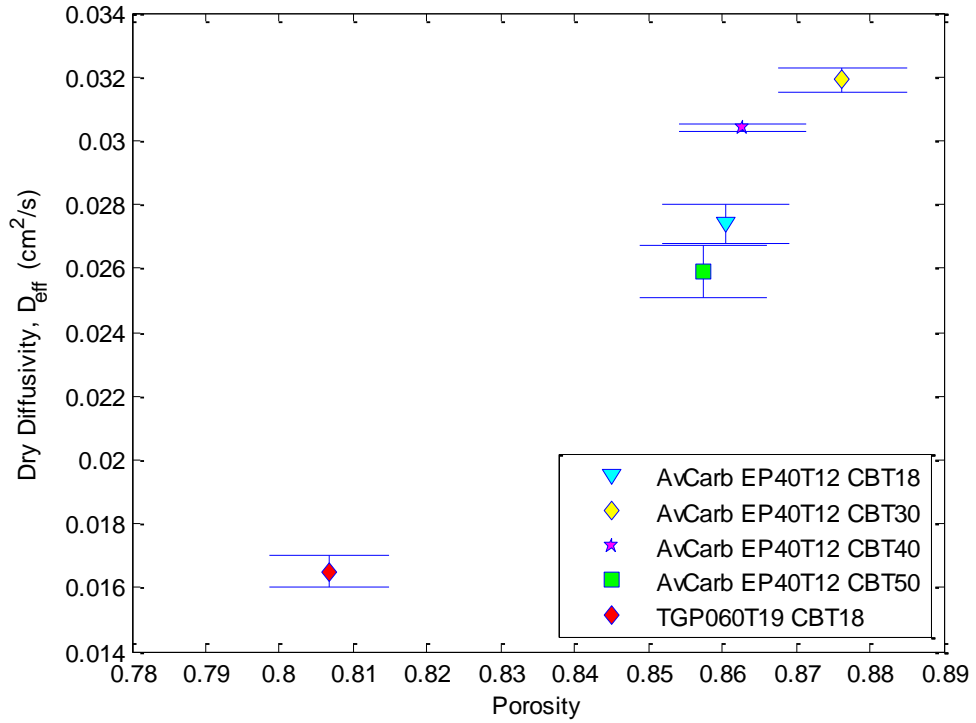


Figure 4-19: Dry diffusivity as a function of porosity (AvCarb EP40 and Toray samples). Porosity values were provided by Ballard

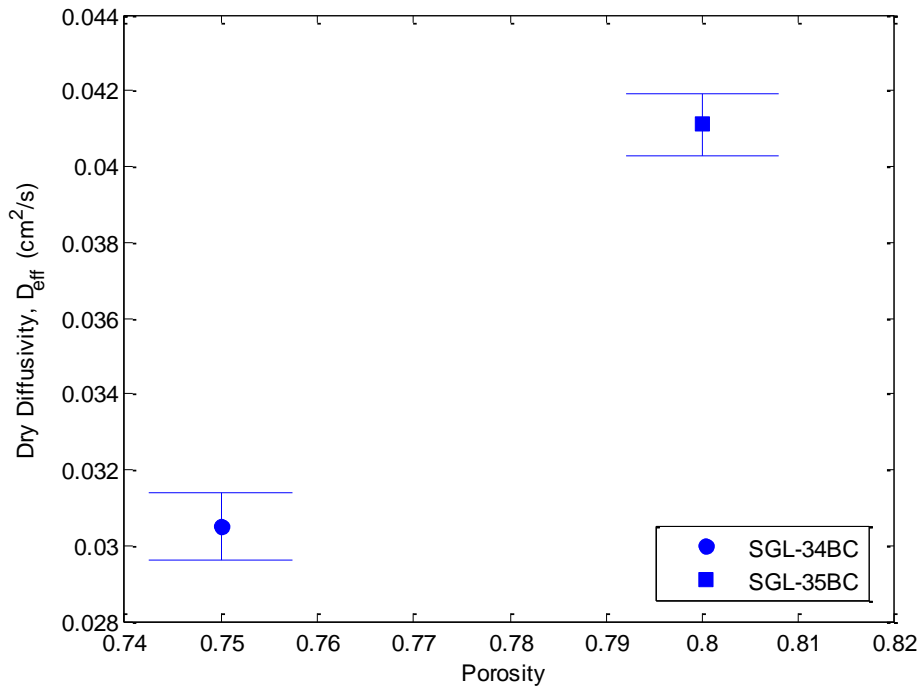


Figure 4-20: Dry diffusivity as a function of porosity (SGL samples). Porosity values are obtained from manufacturer's specification sheet

Diffusivity of a particular GDL sample does not solely depend on porosity. It also depends on the manufacturing process adopted for making the sample. The process for fabricating a GDL, the loading process for PTFE, and the MPL coating procedure are mostly manufacturer specific. Thus, different samples (made by different manufacturers) having similar porosity could have different diffusivity. The variation in the diffusion properties for different samples is shown in Figure 4-21. Diffusivity is presented in terms of diffusibility which is defined as the ratio of the effective diffusion coefficient to the bulk diffusion coefficient [68]. The results show that the Toray sample has low diffusivity despite the fact that it has an intermediate porosity. Also, the diffusibility of the SGL-34BC sample is higher than that of the AvCarb EP-40 samples although the porosity value of the SGL34-BC (0.75) is 12% less than the porosity of the AvCarb EP-40 samples (0.87). Similarly, the diffusibility of SGL-35BC is found to be the highest although it has lower porosity than the Toray and the AvCarb EP-40 samples. These results suggest that the path of diffusion for the SGL samples is less tortuous compared to the AvCarb EP-40 and Toray samples. The PTFE distribution inside the SGL samples might also attribute to the high diffusivity values measured. Thus, it can be concluded that diffusion does not solely depend on the percentage of the pore available for transport. It also depends on the internal structures which vary based on the manufacturing process adopted.

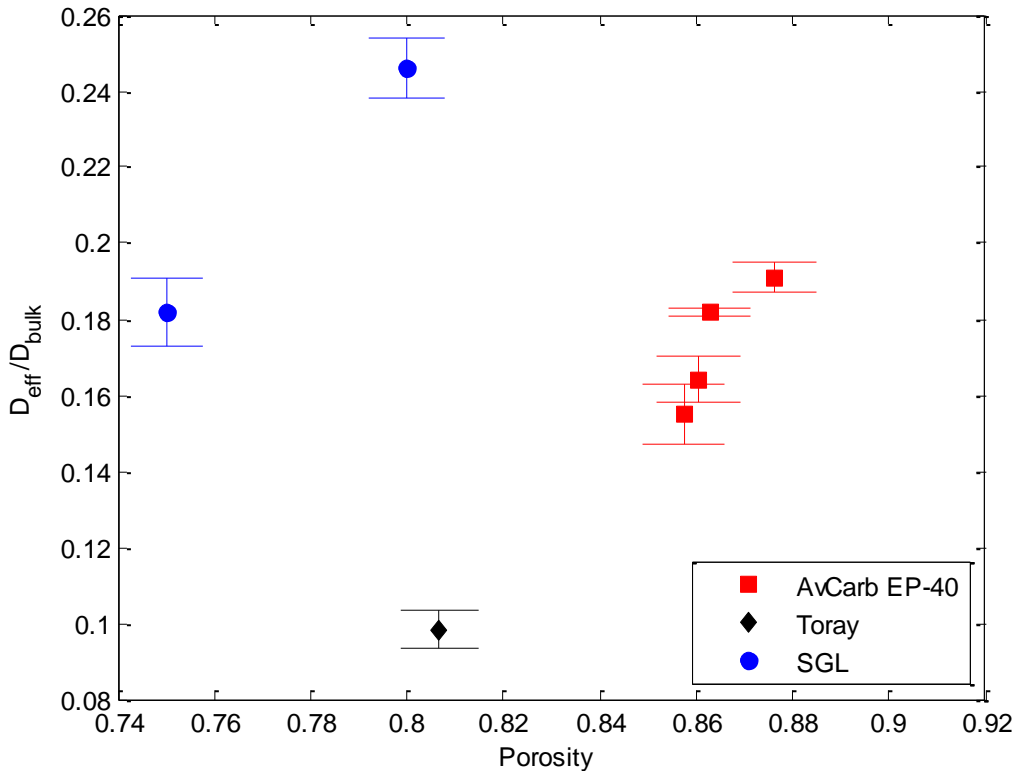


Figure 4-21: Change of diffusibility with the change of porosity for samples made by different manufacturers

4.2.2 Effect of Thickness on Diffusivity

The effect of the thickness on the dry diffusivity is shown in Figure 4-23. It can be seen that for AvCarb EP-40 samples, there is no relationship between the diffusivity and the thickness. This is because the porosity values of all these samples are very close to each other (within 2%). Also, the only difference between the AvCarb EP-40 samples is the thickness of the MPL layer since all the samples have the same GDL containing the same level of PTFE loadings. Therefore, it can be concluded that the effect of the MPL thickness is insignificant when there is little difference in porosity. Similar results were reported by Chan et al. [78] who studied the effect of the MPL thickness on diffusivity. For the SGL samples, on the other hand, larger diffusivity was

obtained for the thicker sample. The same trend was reported by Lamanna et al. [69] who also measured the diffusivity of the SGL-BC samples. The difference between diffusivity of the two SGL samples could be due to the fact that the porosity of these two samples is different by 5%. However, a larger number of samples are required to be tested to identify the effect of the thickness on diffusivity.

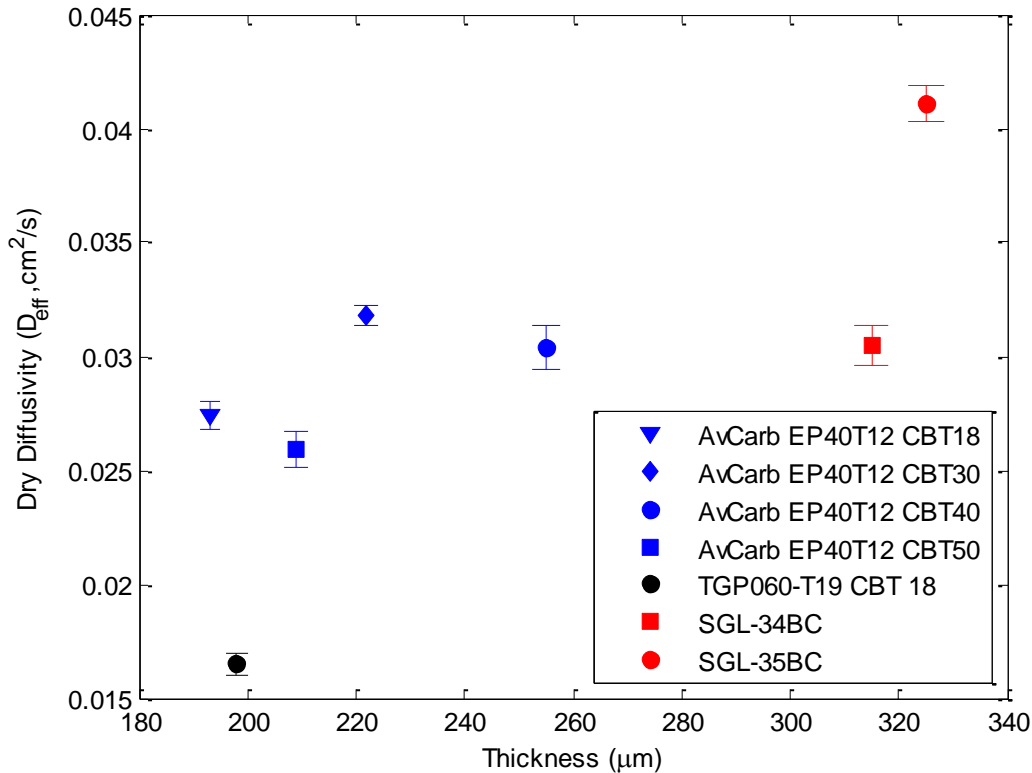


Figure 4-22: Change of diffusivity with the change of thickness for samples made by different manufacturers. The thickness for the SGL samples are taken from manufacturer's specification sheet; while for the other samples the values were taken from [103]

4.2.3 Effect of Pressure Difference on Diffusivity Measurements

It was mentioned in Chapter 3 that the pressure difference across the two sides of the GDL could induce a significant error in the measurements when pure diffusion is of interest.

This effect has been studied here. Figure 4-23 shows the diffusivity results obtained when the pressure difference is intentionally increased between the two sides of the GDL. It can be seen that even for a pressure difference of 5Pa, the diffusivity value is almost doubled. The diffusivity increases linearly with the increase in the pressure difference. This increase in diffusivity is caused due to convection rather than diffusion. Therefore, it is crucial to maintain the pressure difference near zero for studying pure diffusion.

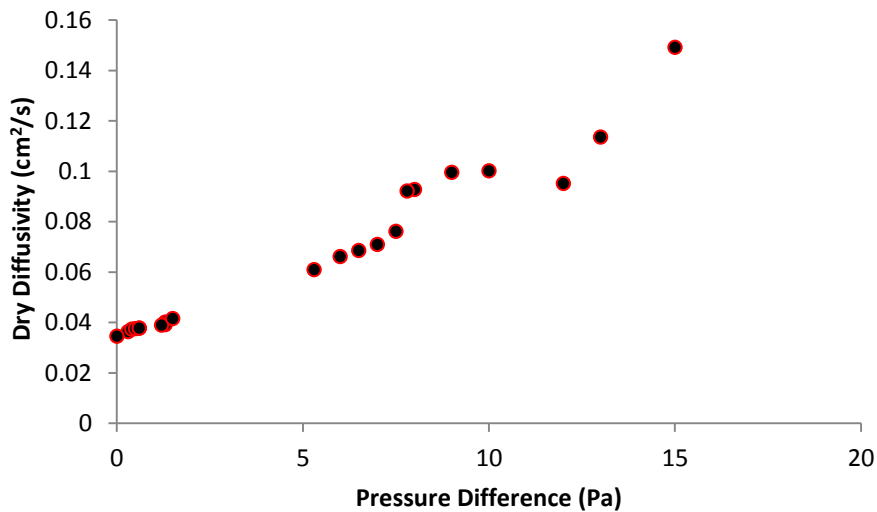


Figure 4-23: Change of diffusivity with the change in the pressure difference across the GDL sample. The pressure difference is intentionally induced to see the effect of pressure gradient on diffusivity

4.2.4 Comparison with Literature

The experimental results obtained here are validated against the results reported in the literature. This comparison is conducted in two steps: First, the results are compared with the theoretical models, predicting the diffusion coefficient as a function of porosity. Then, the results are compared with the available experimental data.

Figure 4-24 shows the dry diffusivity measurements obtained here and those obtained from the theoretical models. These models have been discussed in Chapter 1. The results show that all the models overpredict the diffusivity value, which has also been reported by Lamanna et al. [69], Flückiger et al. [91] and Chan et al. [78]. The porous layers in the fuel cell are under compression which results in the reduction of porosity. In general, the porosity of the sample reduces to 0.4-0.7 when it is under compression [3]. In this range of porosity, there is a deviation even between different models. Therefore, the transport models developed using these correlations overestimate the diffusion rate and underestimate the actual mass transport resistance particularly at higher current densities. One of the main reasons is that the diffusivity correlations presented in these models do not capture the structural complexity of the GDL. Also, the effect of PTFE (or the binder) on the diffusion coefficient is ignored in all these models. As a result the tortuosity assumed in these correlations is far less than the actual tortuosity of the GDLs. The effect of the fiber orientation has also not been included in these models. Finally, the experimental results presented here were obtained for samples with MPLs which have a significantly different microstructure compared to macro-porous GDL layers modeled. These reasons explain the large difference between the experimental results reported in this thesis and those obtained from the theoretical models.

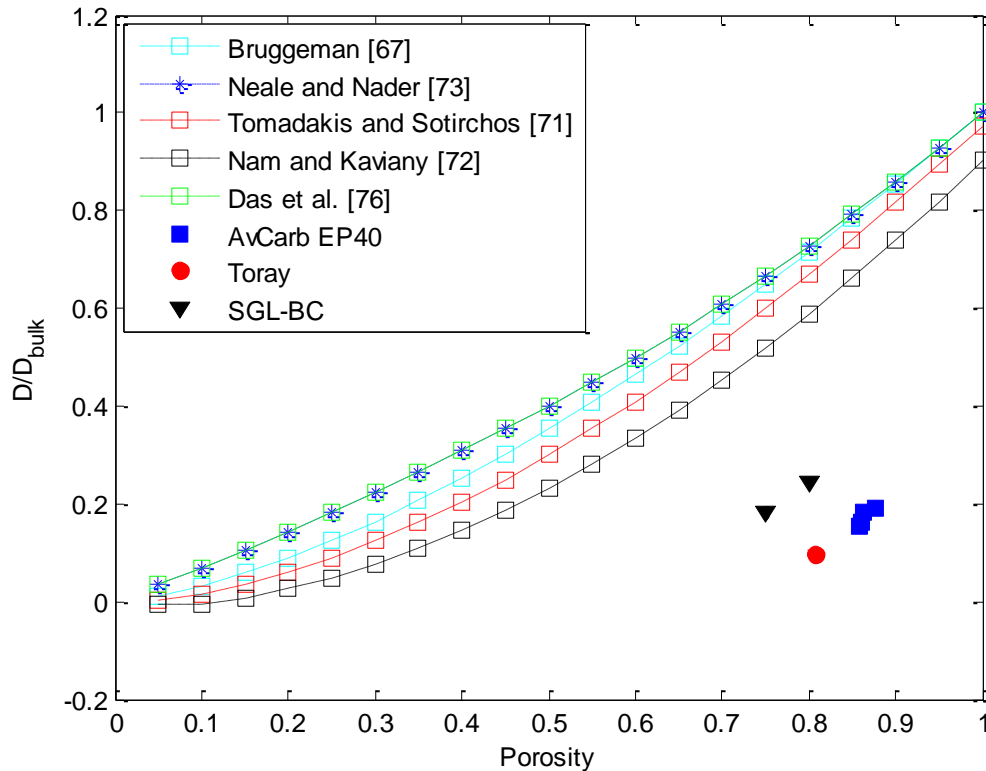


Figure 4-24: Comparison between the diffusivity measured here and those obtained from the theoretical correlations described in Chapter 1

The experimental measurements of diffusivity have been conducted in limited capacity despite their importance in modeling mass transport in the porous sample. Also, the reported measurements were mostly conducted for GDLs without MPLs. Only two groups [69, 78] have conducted the diffusivity measurement with GDL samples including MPLs. Here, the experimental results of this thesis are first compared with those measured with GDL samples without MPLs. Then, the results are compared with those obtained for samples with MPLs.

Figure 4-25 shows that except for the SGL samples the dry diffusivity measurements reported here are outside the trend reported by other researchers for GDLs samples without MPLs. This difference between the diffusivity results is expected as there is a significant

difference between the structures of the GDL and the MPL samples. Similar reduction in diffusivity was also reported by Chan et al. [78]. They showed that diffusivity of a GDL sample drops by 58% upon the addition of a micro-porous layer.

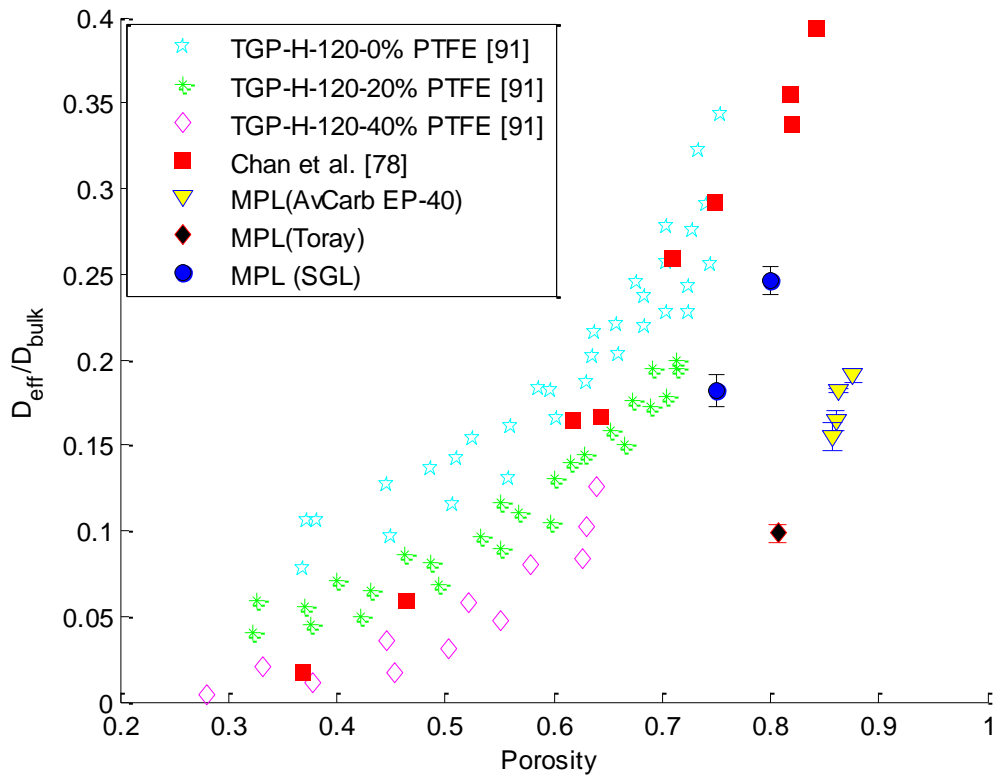


Figure 4-25: Comparison between the dry diffusivity results obtained here and the experimental results reported for GDL samples without MPLs in the literature

It has been shown that the addition of micro-porous layers enhance water management in fuel cells [17]. Therefore, there is an ever growing demand for the measurement of diffusivity in MPL samples to enhance the accuracy of the mass transport models developed. Therefore, in the current research, samples including MPLs were selected for the diffusivity measurement. Figure 4-26 compares the results obtained here with those reported in the literature for samples including MPLs. The results are in agreement even though the samples were made through

different manufacturing processes. The diffusivity values reported by Lamanna et al. [69] are in general higher than the values reported here and in [78]. This difference is due to the fact that Lamanna et al. [69] measured water vapor diffusion in the sample which has a lower molecular weight than air.

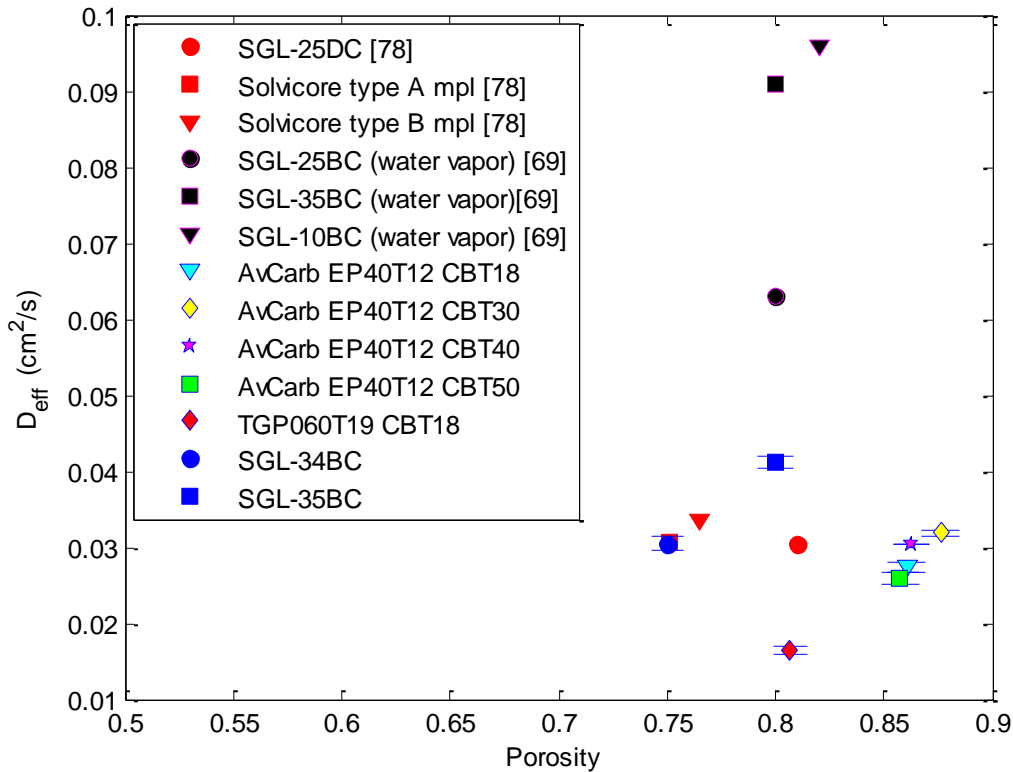


Figure 4-26: Comparison between the dry diffusivity results obtained here and the experimental results reported for GDL samples including MPLs

4.2.5 Wet Diffusivity

The novelty of the proposed diffusivity measurement setup is its capability in measuring gas diffusion in wet samples (see Chapter 3). Figure 4-27 shows the comparison between the dry and wet diffusivity measurements. In general, the diffusivity value decreases as the sample becomes

wet. This decrease in diffusivity is due to the fact that pores previously available for gas transport are blocked by the water injected. A significant drop in the diffusivity value was observed as water was injected into the SGL samples. This indicates that a large amount of water is accumulated in the pores of the SGL samples, which blocks the pathways for gas. Even with lower porosity, the dry diffusivity of the SGL samples is larger than that obtained for AvCarb EP-40 samples. However, the pores of SGL do not repel water as much as the AvCarb EP-40 samples do. Instead, they have a tendency to retain the water that is injected. This results in the reduction in diffusion mass transport in the wet SGL samples. The MPL morphology of the GDL (see SEM images presented in Figures 4-28 to 4-30) has an effect on the reduction of gas diffusivity in the wet sample. Especially, the presence of cracks plays a role in reducing the diffusion coefficient. As observed in the SEM images in Figure 4-30, the SGL samples have cracks which can be visually detected (even at a relatively low magnification); whereas for the AvCarb EP 40 samples, the carbon powders are spread in a way that no cracks can be observed. Therefore, it is easier for water to penetrate and agglomerate inside the SGL samples compared the AvCarb EP-40 samples.

The diffusivity of the AvCarb EP-40 samples decreases as the water is injected, although it is not as large as the reduction observed for the SGL samples. The only irregularity is the diffusivity obtained for the AvCarb EP-40T12 CBT 40 which slightly increased after water injection. The possible explanation for this irregularity could be the fact that this sample is extremely hydrophobic and thick. Also, it is possible that in the course of water injection loosely bound particles remained from the manufacturing process are removed, and hence the diffusion gas transport is enhanced.

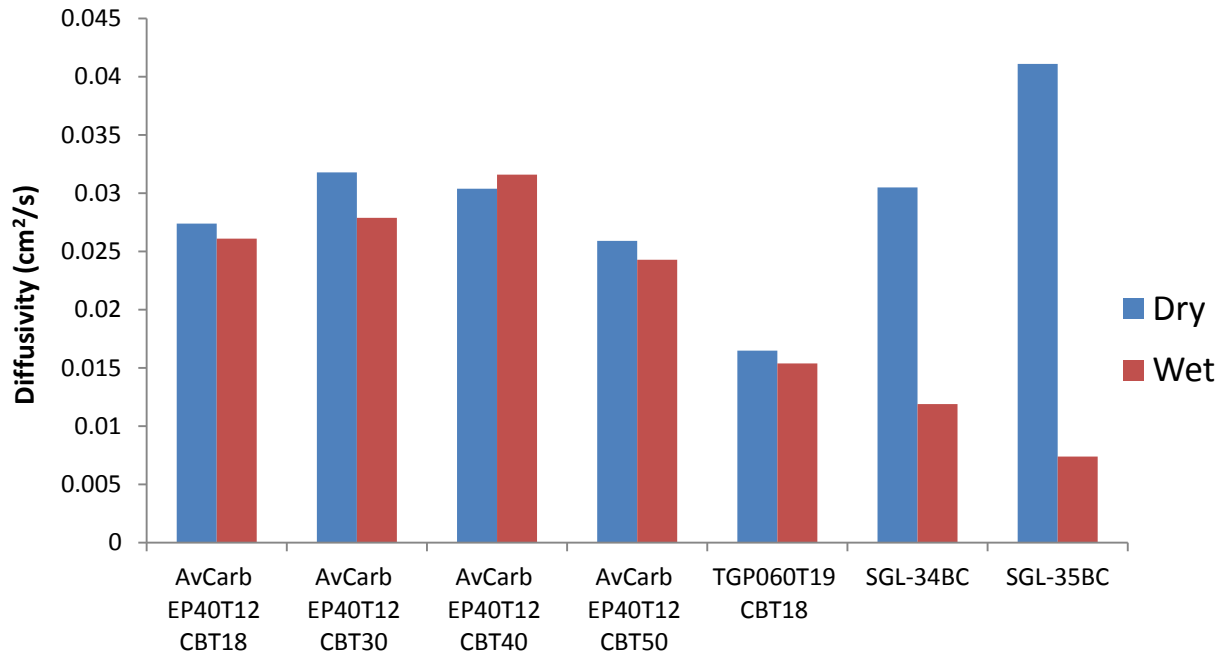


Figure 4-27: Difference between dry and wet diffusivity

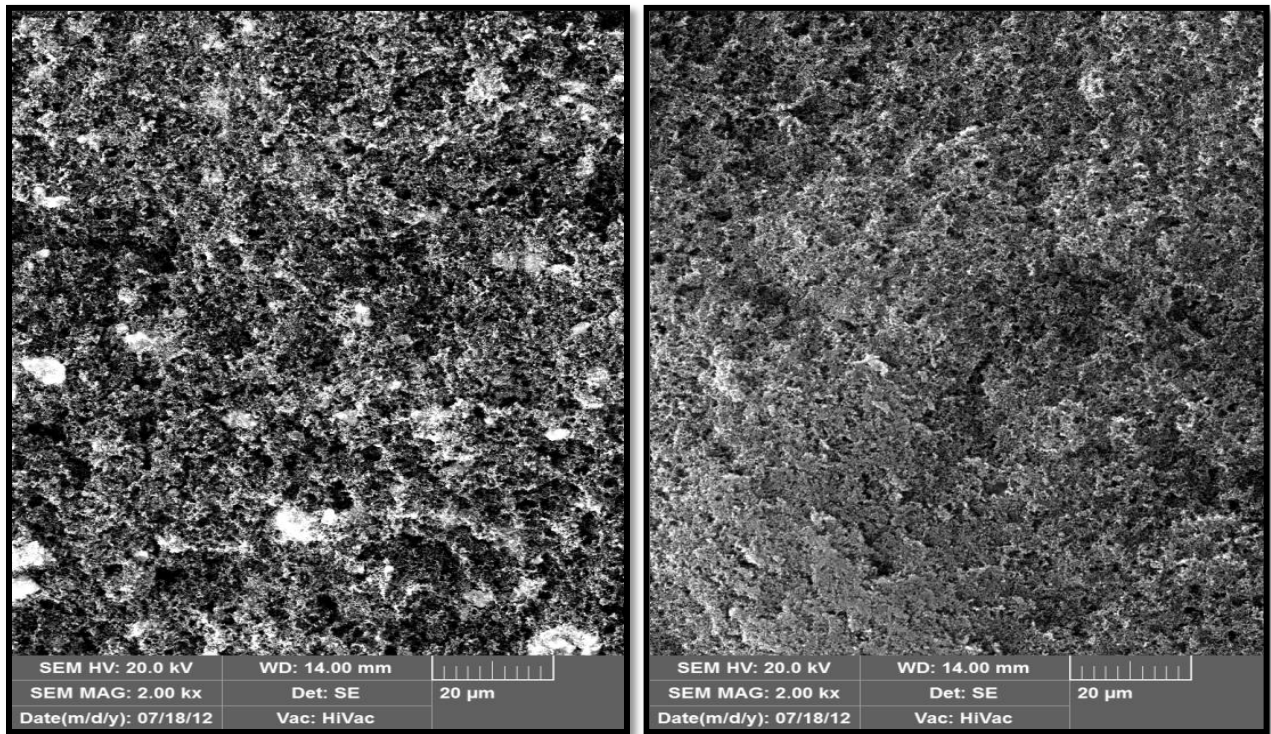


Figure 4-28: SEM images (2000X magnification) of AvCarb EP40T12-CBT18 (left) and AvCarb EP40T12-CBT30 (right)

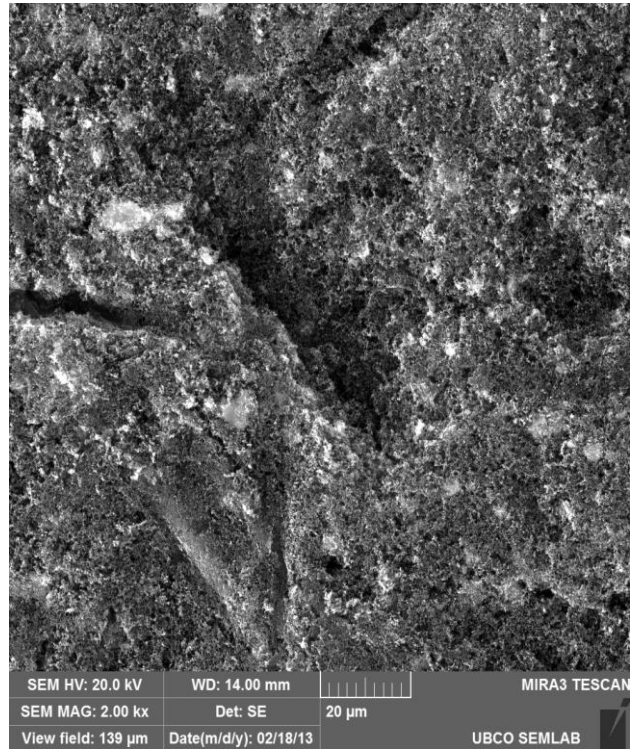
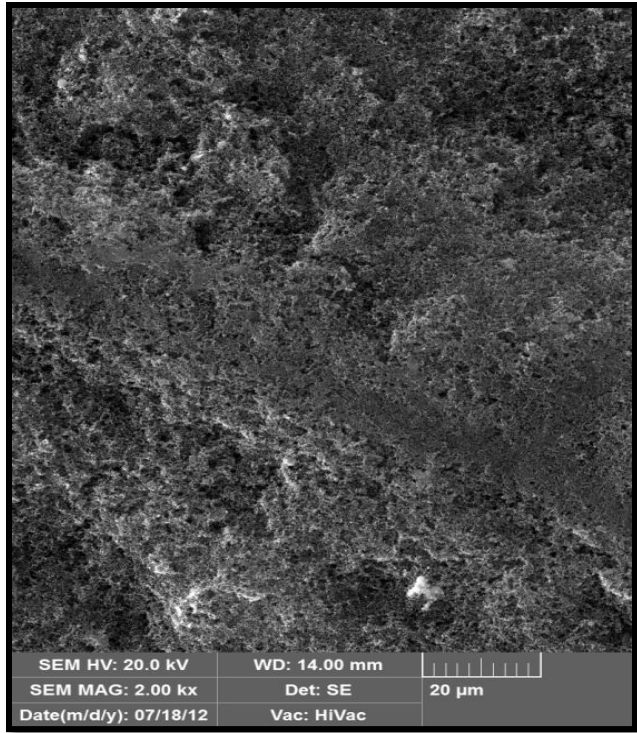


Figure 4-29: SEM images (2000X magnification) of AvCarb EP40T12-CBT40 (left) and TGP060T19-CBT18 (right)

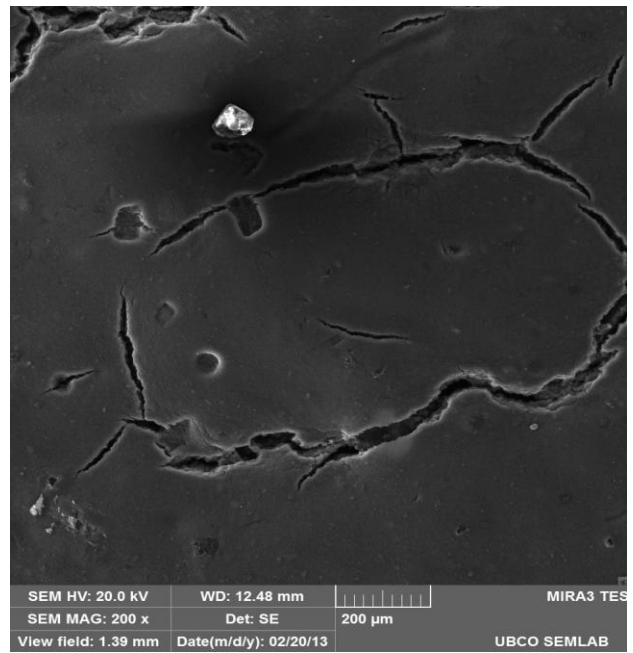
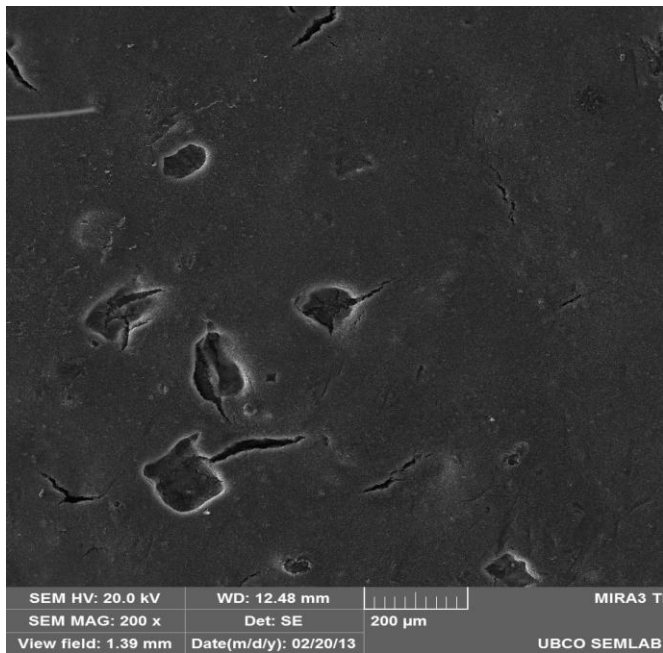


Figure 4-30: SEM images (200X magnification) of SGL-34BC (200X) and SGL-35 BC (200X magnification)

4.2.6 Impact of wettability

The wettability of the AvCarb EP-40 and Toray samples has been quantified by means of measuring the average internal contact angles using the capillary penetration technique [103]. Figure 4-31 shows the wet diffusivity results plotted against the internal contact angles. It is evident that samples with higher contact angles have larger diffusivity when they become wet. In essence, samples with higher contact angles have larger amounts of hydrophobic agents and hence greater tendency to resist water accumulation. Therefore, even after flooding the GDL with water, there are still a number of dry pores present to provide pathways for the gas flow. The higher the hydrophobicity (or the contact angle), the larger the number of passages (dry pores) that are available for gas transport. The only anomaly is again the AvCarb EP40-T12 CBT50 sample which has a relatively high contact angle, low dry diffusivity, and low porosity.

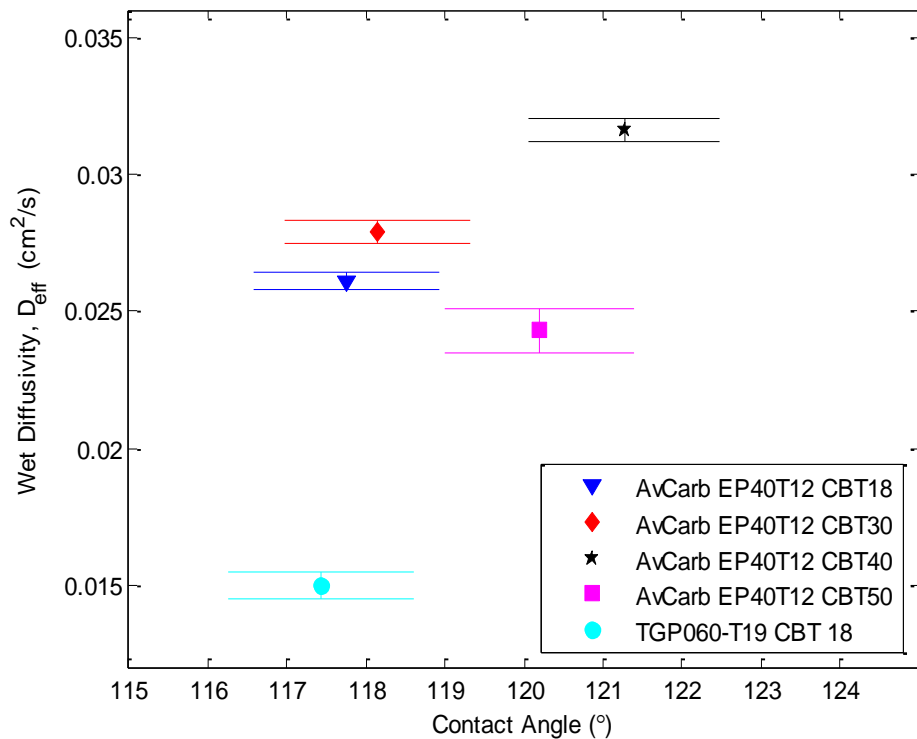


Figure 4-31: Wet diffusivity as a function of the internal contact angles. The contact angle values were taken from [103]

CHAPTER 5: CONCLUSIONS AND FUTURE WORK

In this thesis, experimental approaches were developed to investigate the transport of liquid water and oxygen gas through the gas diffusion layer (GDL) of the proton exchange membrane (PEM) fuel cells. Two different experimental setups were developed to study the transport phenomena of water and oxygen separately. The setup for the study of water transport was developed using the principle described earlier by Shahraeeni and Hoorfar [62]. Fluorescence microscopy was used as a direct visualization technique to understand the behavior of liquid water flow inside the GDL. The time of breakthrough and breakthrough pressure, which are important parameters for water management, were measured. The sources of errors associated with this type of experiment were identified, and their impact on the overall result was highlighted. The influence of various structural properties of the GDL on the water transport characteristics was investigated from quantitative and qualitative perspectives.

A setup was designed and developed to study transport in the GDL due to pure diffusion. A counter diffusion technique was adopted, in which the amount of crossover originated from the difference in the concentration between the two sides of the GDL was measured. The amount of crossover depends on the diffusivity of the GDL which in turn depends on structural and morphological properties of the sample. The relation between the crossover amount and the diffusivity of a particular GDL was established based on the Fick's law. The influence of different GDL properties on diffusivity was also investigated. Precise control of different operational parameters makes this setup unique and more accurate than those developed in the past. Another novelty of the diffusivity setup proposed in this thesis is the ability to measure diffusivity when the GDL becomes wet. A procedure was developed for the first time to inject

water inside the GDL and measure the corresponding crossover. As a result, the diffusion coefficients in saturated GDL samples were measured for the first time.

5.1 Conclusions

The setups explained above were used to measure the transport properties of a variety of GDL samples. The results of the measurements are highlighted in the following points:

Water Transport

- The pressure required to penetrate a GDL (which is referred to as the breakthrough pressure) is higher for the hydrophobic (PTFE treated) samples than the hydrophilic samples. In essence, PTFE loadings decrease the pore size and increase the contact angle which results in obtaining a higher breakthrough pressure. The breakthrough pressure is slightly larger for thicker samples because of the additional pathways that water needs to travel.
- The time of breakthrough follows the same trend as the breakthrough pressure. For a hydrophobic sample, water needs to travel an additional tortuous path and overcome the high pressure barrier to penetrate the GDL. Thus, it takes longer for water to penetrate the hydrophobic sample than the hydrophilic sample. The thickness of the sample does not have a significant effect on the time of breakthrough.
- The use of flexible FEP tubing that readily expands seems to cause significant error in the measurement. It has been shown that the use of flexible tubing overestimates the time of breakthrough by 50%.
- The capillary pressure curve obtained for the carbon cloth samples showed different characteristics than that obtained for the carbon paper GDLs. The capillary pressure of a

carbon paper GDL dropped instantly to its initial pressure at the point of breakthrough; whereas, the capillary pressure for the carbon cloth reduced from its breakthrough pressure but did not drop to its initial pressure at the point of breakthrough.

- Hysteresis in the breakthrough properties was investigated by repeating the measurements with reused samples. It has been shown that when the same sample was reused the breakthrough pressure and time reduced from its initial value. This lowering attributes to the contact with water during the previous sets of experiments. The results suggested that when the GDL comes into contact with water, it loses its hydrophobic characteristics.

Gas Transport

- GDL samples with higher porosity showed to have larger diffusion coefficients. However, porosity is not the only parameter affecting diffusivity as it also depends on the manufacturing process involving the fabrication of the GDL, PTFE loading and MPL coating.
- Even a small pressure gradient between the two sides of a GDL leads to overestimation of diffusivity which is caused by induced convection rather than diffusion. Therefore, it is very important to maintain a zero pressure difference across the two sides of GDL when the measurement of mass transport due to pure diffusion is of interest.
- The diffusion coefficients of the samples with similar porosity do not depend on the sample thickness. However, diffusivity increases with an increase in the thickness if the porosity of the thicker sample is higher than the thinner sample.

- The theoretical correlations used for modeling transport in the porous media considerably overpredict the diffusivity of MPLs. The comparison with the experimental data available in literature showed that the diffusivity of samples with MPLs is much lower than the diffusivity of GDLs without MPLs. The results obtained from the current setup are in close agreement with those reported for MPLs.
- The decrease in diffusivity when the GDL becomes wet is reported for the first time. In general, diffusivity decreases as water injected into the sample. The decrease in the diffusivity when the GDL becomes wet is a good indicator of the water management capability of a particular GDL. A GDL with good water management characteristics does not allow water to accumulate inside the pores and block oxygen transport. Therefore, the diffusivity of GDLs with enhanced water management should not significantly decrease even after flooding the sample with water.
- The wet diffusivity is heavily influenced by the internal contact angle of the GDL. Larger diffusion coefficients were obtained for samples with larger contact angles.

5.2 Potential applications of the research

The parameters measured in this thesis can be utilized in modeling the transport phenomena in GDLs. The breakthrough pressure and the time of breakthrough can be used as the boundary conditions in the models developed. They can also be used as the validating parameters for an already developed model. Also, diffusivity values obtained for MPLs can be used to develop more accurate correlations. The changes in diffusivity when the GDL becomes wet can also be used as a very useful parameter in modeling oxygen transport in the flooding condition.

In addition to modeling, the results also provide a basic insight into the water and gas transport characteristics of GDLs. In essence, the two methodologies proposed in this thesis can be used as effective tools for testing the water management and the transport characteristics of GDLs. The setup developed to estimate the breakthrough characteristics can be used by GDL manufacturers to test the water transport behavior of GDLs. The diffusivity is another important criterion which needs to be tested for every GDL. The methodology described in this thesis can be adopted to test the diffusion properties of GDLs especially at the flooding condition.

5.3 Future Work

Water Transport

- The measurement of saturation is sensitive to the actual flow rate inside the sample at the time of breakthrough. The results of the current measurements and those reported by other researchers [112] suggest that the flow rate at the time of breakthrough will be different for GDLs with different PTFE loadings. Therefore, it is very important to develop a mechanism that could measure directly the flow rate with high accuracy.
- It is desirable to mimic the real operating conditions when ex-situ techniques are used. The typical operating temperature of a fuel cell is around 70-80 °C, but the tests were conducted at room temperature. This difference in the temperature can significantly alter the water vapor production rate through the GDL. Therefore, it is important to conduct the tests at the real temperature. This would also shed lights on the effect of temperature on water transport characteristics.
- The current setup can only measure the characteristics of GDLs without MPL coatings. This limitation is caused due to the use of a pressure sensor having high resolution and accuracy

but a limited pressure range. This can be rectified by installing different pressure sensors covering a wide pressure range but still maintaining accuracy and resolution.

Gas Transport

- The Fick's law has been used to establish the correlation between the crossover amount and the GDL diffusivity. However, the Fick's law might not be accurate for MPLs with nano pores. Therefore, a better relationship taking into account forces originated from the different interactions must be developed.
- The setup is flexible enough to handle ternary transport mimicking the actual fuel cell. The ternary transport should include nitrogen, oxygen and water vapor. For such a transport, an additional humidity sensor needs to be placed on either side of the flow channels to predict the amount of water vapor crossover.
- The effect of operating parameters (e.g., temperature, pressure, relative humidity, and compression) on diffusivity needs to be studied. This can result in identifying an optimum operating condition providing maximum gas diffusivity.

REFERENCES

- [1] F. Barbir. PEM fuel cells: theory and practice, 1st ed. New York: Academic Press, 2005.
- [2] M. Conte, A. Iacobazzi, M. Ronchetti and R. Vellone. Hydrogen economy for a sustainable development: state-of-the-art and technological perspectives. *Journal of Power Sources*, 100:171–187, 2001.
- [3] M.F. Mathias, J. Roth, J. Fleming, W. Lehnert. Diffusion media materials and characterization, in: Vielstich W, Gasteiger HA, Lamm A. (Eds.). *Handbook of fuel cells: fundamentals, Technology and applications*. John Wiley & Sons, Ltd., 2003.
- [4] M.F. Mathias, R. Makharia, H.A. Gasteiger, J.J. Conley, T.J. Fuller, C.J. Gittleman, S.S. Kocha, D.P. Miller, C.K. Mittelsteadt, T.Xie, S.G. Yan and P.T. Yu. Two fuel cell cars in every garage? *Electrochemical Society Interface*, 14:24–35, 2005.
- [5] M.S. Wilson, J.A. Valerio, S. Gottesfeld. Low platinum loading electrodes for polymer electrolyte fuel cells fabricated using thermoplastic ionomers. *Electrochimica Acta*, 40:355–363, 1995.
- [6] H. Li, Y. Tang, Z. Wang, Z Shi, S. Wu, D. Song, J. Zhang, K. Fatih, J. Zhang, H. Wang, Z. Liu, R. Abouatallah and A. Mazza. A review of water flooding issues in the proton exchange membrane fuel cell. *Journal of Power Sources*, 178:103–17, 2008.
- [7] X. Li and I. Sabir. Review of bipolar plates in PEM fuel cells: Flow-field design. *International Journal of Hydrogen Energy*, 30(4):359–371, 2005.
- [8] J. Larminie, A. Dicks and K. (Firm). *Fuel cell systems explained*, 2003.

- [9] V. Mehta and J.S. Cooper. Review and analysis of PEM fuel cell design and manufacturing. *Journal of Power Sources*, 114(1):32–53, 2003.
- [10] G.T. Burstein. A hundred years of Tafel's Equation: 1905–2005. *Corrosion Science*, 47(12):2858–2870, 2005.
- [11] W. He, J.S. Yi and T.V. Nguyen. Two-phase flow model of the cathode of PEM fuel cells using interdigitated flow fields. *AIChE Journal*, 46(177):2053–2064. 2000.
- [12] D. Natarajan, T.V. Nguyen. A two-dimensional, two-phase, multicomponent, transient model for the cathode of a proton exchange membrane fuel cell using conventional gas distributors. *Journal of the Electrochemical Society*, 148:A1324–A1335, 2001.
- [13] J.P. Owejan, T.A. Trabold, D.L. Jacobson, M. Arif and S. Kandlikar. Effects of flow field and diffusion layer properties on water accumulation in a PEM fuel cell. *International Journal of Hydrogen Energy*, 32:4489–4502, 2007.
- [14] J.H. Nam, K-J Lee, G-S Hwang, C-J Kim and M. Kaviany. Microporous layer for water morphology control in PEMFC. *International Journal of Heat and Mass Transfer*, 52:2779–2791, 2009.
- [15] D. Spornjak, S.G. Advani and A.K.Prasad. Simultaneous Neutron and Optical Imaging in PEM Fuel Cells. *Journal of Electrochemical Society*, 156:B109–B117, 2009.
- [16] D. Spornjak, A.K. Prasad, S.G. Advani. Experimental investigation of liquid water formation and transport in a transparent single-serpentine PEM fuel cell. *Journal of Power Sources*, 170:334–344, 2007.

[17] R.P. Ramasamy, E.C. Kumbur, M.M. Mench, W. Liu, D. Moore and M. Murthy. Investigation of macro- and micro-porous layer interaction in polymer electrolyte fuel cells. *International Journal of Hydrogen Energy*, 33:3351–3367, 2008.

[18] U. Pasaogullari and C.Y.Wang. Liquid water transport in gas diffusion layer of polymer electrolyte fuel cells. *Journal of the Electrochemical Society*, 151(3):A399–A406, 2004.

[19] B.R. Friess and M. Hoorfar. Measurement of internal wettability of gas diffusion porous media of proton exchange membrane fuel cells. *Journal of Power Sources*, 195:4736–4742, 2010.

[20] B.R. Friess, M. Hoorfar. Measurement of Average Contact Angles of Gas Diffusion Layers Using a Novel Fluorescence Microscopy Method. *Journal of Fuel Cell Science and Technology*, 8:021006–021010, 2011.

[21] V. Gurau, M.J. Bluemle, E.S. De Castro, Y.-M.Tsou, J.A. Mann, T.A. Zawodzinski. Characterization of transport properties in gas diffusion layers for proton exchange membrane fuel cells 1. Wettability (internal contact angle to water and surface energy of GDL fibers). *Journal of Power Sources*, 160:1156–1162, 2006.

[22] J. Gostick, M. Fowler, M. Ioannidis, M. Pritzker, Y.M. Volfkovich and A. Sakars. Capillary pressure and hydrophilic porosity in gas diffusion layers for polymer electrolyte fuel cells. *Journal of Power Sources*, 156:375–387, 2006.

[23] K.G. Gallagher, R.M. Darling, T.W. Patterson and M.L. Perry. Capillary pressure saturation relations for PEM fuel cell gas diffusion layers. *Journal of Electrochemical Society*. 155(11):1225–1231, 2008.

[24] J. T. Gostick, M.A. Ioannidis, M.W. Fowler and M.D. Pritzker. Direct measurement of the capillary pressure characteristics of water–air–gas diffusion layer systems for PEM fuel cells. *Electrochemistry Communications*, 10:1520–1523, 2008.

[25] J. Benziger, J. Nehlsen, D. Blackwell, T. Brennan and J. Itescu. Water flow in the gas diffusion layer of PEM fuel cells. *Journal of Membrane Science*, 261:98–106, 2005.

[26] J.T. Gostick, M.A. Ioannidis, M.D. Pritzker and M.W. Fowler. Impact of liquid water on reactant mass transfer in PEM fuel cell electrodes. *Journal of the Electrochemical Society*, 157(4):563–571, 2010.

[27] M.A. Hickner, N.P. Siegel, K.S. Chen, D.S. Hussey, D.L. Jacobson and M. Arif. In situ high-resolution neutron radiography of cross-sectional liquid water profiles in proton exchange membrane fuel cells. *Journal of the Electrochemical Society*, 155:B427–B434, 2008.

[28] T. Rosén, J. Eller, J. Kang, N.I. Prasianakis, J. Mantzaras and F.N. Büchi. Saturation dependent effective transport properties of PEMFC gas diffusion layers. *Journal of the Electrochemical Society*, 159:F536–F544, 2012.

[29] C. Lim and C.Y. Wang. Effects of hydrophobic polymer content in GDL on power performance of a PEM fuel cell. *Electrochimia Acta*, 49:4149–4156, 2004.

[30] I.R. Harkness, N. Hussain, L. Smith and J.D.B. Sharman. The use of novel water porosimeter to predict the water handling behavior of gas diffusion media used in polymer electrolyte fuel cells. *Journal of Power Sources*, 193:122–129, 2009.

[31] R.B. Mathur, P.H. Maheshwari, T.L. Dhama and R.P. Tandon. Characteristics of the carbon paper heat-treated to different temperatures and its influence on the performance of PEM fuel cell. *Electrochimia Acta*, 52:4809–4817, 2007.

[32] A. Jena and K. Gupta. Advances in pore structure evaluation by porometry. *Chemical Engineering and Technology*, 33:1241–1250, 2010.

[33] N. Zamel, X. Li, J. Becker and A. Wiegmann. Effect of liquid water on transport properties of the gas diffusion layer of polymer electrolyte membrane fuel cells. *International Journal of Hydrogen Energy*, 36:5466–5478, 2011.

[34] M. Ji and Z. Wei. A Review of water management in polymer electrolyte membrane fuel cells. *Energies*, 2:1057–1106, 2009.

[35] A. Bazylak. Liquid water visualization in PEM fuel cells: A review. *International Journal of Hydrogen Energy*, 34:3845–3857, 2009.

[36] J. Zawodzinski, A. Thomas, C. Derouin, S. Radzinski, R.J. Sherman, V.T. Smith, T.E. Springer, S. Gottesfeld. Water uptake by and transport through nafion (r) 117 membranes. *Journal of the Electrochemical Society*, 140:1041–1047, 1993.

[37] S. Tsushima, K. Teranishi and S. Hirai. Magnetic resonance imaging of the water distribution within a polymer electrolyte membrane in fuel cells. *Electrochemical and Solid-State Letters*, 7:A269–A272, 2004.

[38] K. Teranishi, S. Tsushima, and S. Hirai. Study of the effect of membrane thickness on the performance of polymer electrolyte fuel cells by water distribution in a membrane. *Electrochemical and Solid-State Letters*, 8:A281–A284, 2005.

[39] K. Feindel, S. Bergens and R. Wasylshen. Insights into the distribution of water in a self-humidifying h₂/o₂ proton-exchange membrane fuel cell using 1h nmr microscopy. *Journal of the American Chemical Society*, 128(43):14192–14199, 2006.

[40] R. Satija, D. Jacobson, M. Arif and S. Werner. In situ neutron imaging technique for evaluation of water management systems in operating PEM fuel cells. *Journal of Power Sources*, 129(2):238–245, 2004.

[41] R. Mosdale, G. Gebel and M. Pineri. Water profile determination in a running proton exchange membrane fuel cell using small-angle neutron scattering. *Journal of Membrane Science*, 118(2):269–277, 1996.

[42] T. Trabold, J. Owejan, D. Jacobson, M. Arif and P. Huffman. In situ investigation of water transport in an operating PEM fuel cell using neutron radiography: Part 1—experimental method and serpentine flow field results. *International Journal of Heat and Mass Transfer*, 49(25):4712–4720, 2006.

[43] A. Turhan, K. Heller, J. Brenizer and M. Mench. Quantification of liquid water accumulation and distribution in a polymer electrolyte fuel cell using neutron imaging. *Journal of Power Sources*, 160(2):1195–1203, 2006.

[44] J. Owejan, T. Trabold, D. Jacobson, D. Baker, D. Hussey and M. Arif. In situ investigation of water transport in an operating PEM fuel cell using neutron radiography: part 2—transient water accumulation in an interdigitated cathode flow field. *International Journal of Heat and Mass Transfer*, 49(25):4721–4731, 2006.

[45] J. Zhang, D. Kramer, R. Shimoji, Y. Ono, E. Lehmann, A. Wokaun, K. Shinohara and G. Scherer. In situ diagnostic of two-phase flow phenomena in polymer electrolyte fuel cells by neutron imaging:: Part b. material variations. *Electrochimica Acta*, 51(13):2715–2727, 2006.

[46] S. Kim and M.M. Mench. Investigation of temperature-driven water transport in polymer electrolyte fuel cell: phase-change-induced flow. *Journal of The Electrochemical Society*, 156:B353–B362, 2009.

[47] Y.-S. Chen, H. Peng, D.S. Hussey, D.L. Jacobson, D.T. Tran, T. Abdel-Baset and M. Biernacki. Water distribution measurement for a PEMFC through neutron radiography. *Journal of Power Sources*, 170:376–386, 2007.

[48] P. Sinha, P. Halleck and C. Wang. Quantification of liquid water saturation in a PEM fuel cell diffusion medium using x-ray microtomography. *Electrochemical and Solid-State Letters*, 9:A344–A348, 2006.

[49] I. Manke, C. Hartnig, M. Grunerbel, W. Lehnert, N. Kardjilov, A. Haibel, A. Hilger, J. Banhart and H. Riesemeier. Investigation of water evolution and transport in fuel cells with high resolution synchrotron x-ray radiography. *Applied Physics Letters*, 90(17):174105–174105, 2007.

[50] C. Hartnig, I. Manke, R. Kuhn, S. Kleinau, J. Goebbels and J. Banhart. High-resolution in-plane investigation of the water evolution and transport in PEM fuel cells. *Journal of Power Sources*, 188:468–474, 2009.

[51] F.N. Büchi, R. Flückiger, D. Tehlar, F. Marnoe and M. Stampanoni. Determination of liquid water distribution in porous transport layers. *ECS Transaction*, 16(2):587–592, 2008.

[52] K. Tüber, D. Pöcza and C. Hebling. Visualization of water buildup in the cathode of a transparent PEM fuel cell. *Journal of Power Sources*, 124(2):403–414, 2003.

[53] X. Yang, F. Zhang, A. Lubawy and C. Wang. Visualization of liquid water transport in PEMFC. *Electrochemical and Solid-State Letters*, 7(11):A408-A411, 2004.

[54] S. Ge and C.Y. Wang. Liquid water formation and transport in the PEMFC Anode. *Journal of The Electrochemical Society*, 154(10):B998–B1005, 2007.

[55] A. Theodorakakos, T. Ous, M. Gavaises, J. Nouri, N. Nikolopoulos, and H. Yanagihara. Dynamics of water droplets detached from porous surfaces of relevance to PEM fuel cells. *Journal of Colloid and Interface Science*, 300(2):673–687, 2006.

[56] E. Kimball, T. Whitaker, Y. Kevrekidis and J. Benziger. Drops, slugs, and flooding in polymer electrolyte membrane fuel cells. *AIChE Journal*, 54(5):1313–1332, 2008.

[57] S. Litster, D. Sinton and N. Djilali. Ex situ visualization of liquid water transport in PEM fuel cell gas diffusion layers. *Journal of Power Sources*, 154(1):95–105, 2006.

[58] A. Bazylak, D. Sinton, Z. Liu and N. Djilali. Effect of compression on liquid water transport and microstructure of PEMFC gas diffusion layers. *Journal of Power Sources*, 163(2):784–792, 2007.

[59] A. Bazylak, D. Sinton and N. Djilali. Dynamic water transport and droplet emergence in PEMFC gas diffusion layers. *Journal of Power Sources*, 176(1):240–246, 2008.

[60] J. T. Gostick, M.A. Ioannidis, M.W. Fowler and M.D. Pritzker. On the role of the microporous layer in PEMFC operation. *Electrochemical Communications*, 11:576–579, 2009.

[61] J. T. Gostick, M.A. Ioannidis, M.W. Fowler and M.D. Pritzker. Pore network modeling of fibrous gas diffusion layers for polymer electrolyte membrane fuel cells. *Journal of Power Sources*, 173:277–290, 2007.

[62] M. Shahraeeni and M. Hoorfar. Effect of gas diffusion layer properties on the time of breakthrough. *Journal of Power Sources*, 196:5918–5921, 2011.

[63] A. Casalegno, L. Colombo, S. Galbiati and R. Marchesi. Quantitative characterization of water transport and flooding in the diffusion layers of polymer electrolyte fuel cells. *Journal of Power Sources*, 195:4143–4148, 2010.

[64] H. Mehrer and N.A. Stolwijk. Heroes and highlights in the history of diffusion. *The Open-Access Journal for the Basic Principles of Diffusion Theory, Experiment and Application*, *Diffusion-fundamentals.org*, 11:1–32, 2009.

[65] D. Kramer, S.A. Freunberger, R. Flückiger, I.A. Schneider, A. Wokaun, F.N. Büchi and G.G. Scherer. Electrochemical diffusimetry of fuel cell gas diffusion layers. *Journal of The Electroanalytical Chemistry*, 612:63–77, 2008.

[66] M. Mezedur, M. Kaviani and W. Moore. Effect of pore structure, randomness and size on effective mass diffusivity. *AIChE Journal*, 48:15–24, 2002.

[67] D. Bruggeman. Berechnung verschiedener physikalischer konstanten von heterogenen substanzen. *Ann Phys (Leipzig)*. 24:636–679, 1935.

[68] N. Zamel, N. Astrath, X. Li, J. Shen, J. Zhou, F. Astrath, H. Wang and Z-S. Liu. Experimental measurements of effective diffusion coefficient of oxygen-nitrogen mixture in PEM fuel cell diffusion media. *Chemical Engineering Science*, 65(2): 931–937, 2010.

[69] J.M. LaManna and S.G. Kandlikar. Determination of effective water vapor diffusion coefficient in PEMFC gas diffusion layers. *International Journal of Hydrogen Energy*, 36:5021–5029, 2011.

[70] L.M. Pant, S.K. Mitra and M. Secanell. Mass transport measurements in porous transport layers of a PEM fuel cell. *International Conference on Micro Nano and Mini Channel, Edmonton-2011. ICNMM2011-58181*.

[71] M.M. Tomadakis and S. Sotirchos. Ordinary and transition regime diffusion in random fiber structures. *AIChE Journal*, 39:397–412, 1993.

[72] J. Nam and M. Kaviany. Effective diffusivity and water-saturation distribution in single- and two-layer PEMFC diffusion medium. *International Journal of Heat and Mass Transfer*, 46(24):4595–4611, 2003.

[73] G. Neale and W. Nader. Prediction of transport processes within porous media – diffusive flow processes within an homogeneous swarm of spherical-particles. *AIChE Journal*, 19:112–119, 1973.

[74] D. Mu, Z.S. Liu, C. Huang and N. Djilali. Prediction of the effective diffusion coefficient in random porous media using the finite element method. *Journal of Porous Materials*, 14:49–54, 2007.

[75] Hashin Z. The elastic moduli of heterogeneous materials. *Journal of Applied Mechanics*, 29:143–50, 1962.

[76] P.K. Das, X. Li and Z.S. Liu. Effective transport coefficients in PEM fuel cell catalyst and gas diffusion layers: Beyond Bruggeman approximation. *Applied Energy*, 87:2785–2796, 2010.

[77] N. Zamel, X. Li and J. Shen. Correlation for the effective gas diffusion coefficient in carbon paper diffusion media. *Energy and Fuels*. 23:6070–6078, 2009.

[78] C. Chan, N. Zamel, X. Li and J. Shen. Experimental measurement of effective diffusion coefficient of gas diffusion layer/microporous layer in PEM fuel cells. *Electrochimica Acta*, 65:13–21, 2012.

[79] T. Marrero and E. Mason. Gaseous diffusion coefficients. *Journal of Physical and Chemical Reference Data*, 1(1):3–118, 1972.

[80] A. Fick. Ueber diffusion. *Annalen der Physik*, 170(1):59–86, ISSN 1521–3889, 1855.

[81] J. Becker, R. Flückiger, M. Reum, F.N. Büchi, F. Marone and M. Stampanonic. Determination of material properties of gas diffusion layers: experiments and simulations using phase contrast tomographic microscopy. *Journal of The Electrochemical Society*, 156(10):B1175–B1181, 2009.

[82] N. Astrath, J. Shen, D. Song, J. Rohling, F. Astrath, J. Zhou, T. Navessin, Z.S. Liu, C.E. Gu and X. Zhao . The effect of relative humidity on binary gas diffusion. *Journal of Physical Chemistry*, 113:8369–8374, 2009.

[83] E.N. Fuller , P.D. Schettler and J. C. Giddings. New method for prediction of binary gas-phase diffusion co-efficients. *Industrial and Engineering Chemistry Research*, 58 (5):18–27, 1966.

[84] C. Quick, D. Ritzinger, W. Lehnert and C. Hartnig. Characterization of water transport in gas diffusion media. *Journal of Power Sources*, 190:110–120, 2009.

[85] Z.Yu and R.N. Carter. Measurement of effective oxygen diffusivity in electrodes for proton exchange membrane fuel cells. *Journal of Power Sources*, 195:1079–1084, 2010.

[86] Y. Utaka, Y. Tasaki, S. Wang, T. Ishiji and S. Uchikoshi. Method of measuring oxygen diffusivity in microporous media. *International Journal of Heat and Mass Transfer*, 52:3685–3692, 2009.

[87] D.R. Baker, C. Wieser, K.C. Neyerlin and M.W. Murphy. The Use of limiting current to determine transport resistance in PEM fuel cells. *ECS Transactions*, 3:989–999, 2006.

[88] D.R. Baker, D.A. Caulk, K.C. Neyerlin and M.W. Murphy. Measurement of oxygen transport resistance in PEM fuel cells by limiting current methods. *Journal of The Electrochemical Society*, 156(9): B991–B1003, 2009.

[89] J. Stumper, M. Löhr and S. Hamada. Diagnostic tools for liquid water in PEM fuel cells. *Journal of Power Sources*, 143:150–157, 2005.

[90] U. Beuscher. Experimental method to determine the mass transport resistance of a polymer electrolyte fuel cell. *Journal of The Electrochemical Society*, 153:A1788–1793, 2006.

[91] R. Flückiger, S.A. Freunberger, D. Kramer, A. Wokaun, G.G. Scherer and F.N. Büchi. Anisotropic, effective diffusivity of porous gas diffusion layer materials for PEMFC. *Electrochimica Acta*, 54: 551–559, 2008.

[92] L.M. Pant, S.K. Mitra and M. Secanell. Absolute permeability and Knudsen diffusivity measurements in PEMFC gas diffusion layers and micro porous layers. *Journal of Power Sources*, 206:153–160, 2012.

[93] L.M. Pant, S.K. Mitra and M. Secanell. A generalized mathematical model to study gas transport in PEMFC porous media. *International Journal of Heat and Mass Transfer*. 58:70–79, 2013.

[94] N.M. Carrigy, L.M. Pant, S.K. Mitra and M. Secanell. Knudsen diffusivity and permeability of PEMFC microporous coated gas diffusion layers for different polytetrafluoroethylene loadings. *Journal of The Electrochemical Society*, 160: F81–F89, 2013.

[95] B. R. Masters. Book review of handbook of biological confocal microscopy, 3rd ed. by J. B. Pawley. *Journal of Biomedical Optics*, 13(2):029902-1–029902-3, 2008.

[96] Y. S. Shin, K. Cho, S. H. Lim, S. Chung, S.-J. Park, C. Chung, D.-C. Han and J.K. Chang. PDMS-based micro PCR chip with Parylene coating. *Journal of Micromechanics and Microengineering*, 13(5):768–774, 2003.

[97] M. Shahraeeni and M. Hoorfar. Experimental and numerical comparison of water transport in untreated and treated diffusion layers of proton exchange membrane (PEM) fuel cells. *Journal of Power Sources*, 238:29–47, 2013.

[98] T. Marrero and E. Mason. Gaseous diffusion coefficients. *Journal of Physical and Chemical Reference Data*, 1(1):3–118, 1972.

[99] J. Winkelmann. Measurement methods: Diffusion of gases in gases, liquids and their mixtures. *Landolt Bornstein Database*, 2007.

[100] L.M. Pant. Experimental and theoretical investigation of mass transport in porous media of a PEM fuel cell. M.Sc. Thesis. University of Alberta, Edmonton, AB. 2011.

[101] Sensirion differential sensor ASP1400 datasheet.

[102] G.A. Eiceman. Instrumentation of gas chromatography. In RA Meyers, Ed. *Encyclopedia of Analytical Chemistry*. Chichester: John Wiley & Sons, 1–9, 2000.

[103] R.K. Phillips, B.R. Friess, A.D. Hicks, J. Bellerive and M. Hoorfar. Ex-situ measurement of properties of gas diffusion layers of PEM fuel cells. *WHEC:763*, 2012.

[104] J.P. Owejan, J.E. Owejan, W. Gu, T.A. Trabold, T.W. Tighe, T.W., M.F. Mathias. Water transport mechanism in PEMFC gas diffusion layers. *Journal of The Electrochemical Society*, 157:1456–1464, 2010.

[105] U. Pasaogullari, C.Y. Wang and K.S. Chen. Two-phase transport in polymer electrolyte fuel cells with bilayer cathode gas diffusion media. *Journal of The Electrochemical Society*, 152:A1574–A1582, 2005.

[106] Z. Lu, M.M. Daino, C. Rath and S. Kandlikar. Water management studies in PEM fuel cells, part III: Dynamic breakthrough and intermittent drainage characteristics from GDLs with and without MPLs. *International Journal of Hydrogen Energy*, 35: 4222–4233, 2010.

- [107] S. Jennings, The mean free path in air. *Journal of Aerosol Science*, 19(2):159–166, 1988.
- [108] R. Agarwal, K.-Y. Yun and R. Balakrishnan. Beyond Navier-Stokes: Burnett equations for flows in the continuum-transition regime. *Physics of Fluids*, 13(10):3061–3085, 2001.
- [109] D. Mu, Z.S. Liu, C. Huang and N. Djilali. Determination of the effective diffusion coefficient in porous media including Knudsen effects. *Microfluid Nanofluid*, 4:257–260, 2008.
- [110] W. Kast and C.R. Hohenthanner. Mass transfer within the gas-phase of porous media. *International Journal of Heat and Mass Transfer*, 43(5):807–823, 2000.
- [111] A.W. Neumann, R. David and Y.Y. Zuo. *Applied Surface Thermodynamics*. Taylor and Francis, 2010.
- [112] E. Gauthier, Q. Duan, T. Hellstern and J. Benziger. Water flowing through, and around the gas diffusion layer. *FUEL CELLS*, 12(5):835–847, 2012.
- [113] Y.M. Volkovich, V.E. Sosenkin, V.S. Bagotsky. Structural and wetting properties of fuel cell components. *Journal of Power Sources*, 195:5429–5441, 2010.